Summer 9-1-2014

Optimal Control and Synchronization of Dynamic Ensemble Systems

Anatoly Zlotnik
Washington University in St. Louis

WASHINGTON UNIVERSITY IN ST. LOUIS

School of Engineering and Applied Science

Department of Electrical and Systems Engineering

Dissertation Examination Committee:
Jr-Shin Li, Chair
ShiNung Ching
István Kiss
Dan Moran
Hiro Mukai
Heinz Schaettler

Optimal Control and Synchronization of Dynamic Ensemble Systems

by

Anatoly Zlotnik

A dissertation presented to the Graduate School of Arts and Sciences
of Washington University in partial fulfillment of the
requirements for the degree of

Doctor of Philosophy

August 2014
Saint Louis, Missouri

Contents

List of Figures

List of Tables

Acknowledgments

I wish to express my gratitude to my advisor, Dr. Jr-Shin Li, for his generous attention, guidance, confidence, and support during my studies at Washington University in St. Louis. I am also grateful to Dr. István Kiss for sharing his insight over many discussions throughout our work together. I would also like to thank the members of my dissertation defence committee, Dr. ShiNung Ching, Dr. Dan Moran, Dr. Hiro Mukai, and Dr. Heinz Schaettler, for their time and helpful suggestions. I also wish to thank the many instructors and mentors from the University of Nebraska – Lincoln, Case Western Reserve University, and Washington University in St. Louis for helping me to establish a foundation on which to build my research. In addition, I would like to thank my colleagues and collaborators Justin Ruths, Isuru Dasanayake, Ji Qi, Hisa-Aki Tanaka, Yifei Chen, and Wei Zhang, who made working on challenging problems a pleasure.

Most of the credit and my gratitude is due to my parents, who always provided me with their love and support. Their encouragement made this work possible.

Anatoly Zlotnik

Washington University in Saint Louis
August 2014

Dedicated to my parents.

ABSTRACT OF THE DISSERTATION

Optimal Control and Synchronization of Dynamic Ensemble Systems

by

Anatoly Zlotnik

Doctor of Philosophy in Systems Science and Mathematics

Washington University in St. Louis, August 2014

Professor Jr-Shin Li, Chair

Ensemble control involves the manipulation of an uncountably infinite collection of structurally identical or similar dynamical systems, which are indexed by a parameter set, by applying a common control without using feedback. This subject is motivated by compelling problems in quantum control, sensorless robotic manipulation, and neural engineering, which involve ensembles of linear, bilinear, or nonlinear oscillating systems, for which analytical control laws are infeasible or absent. The focus of this dissertation is on novel analytical paradigms and constructive control design methods for practical ensemble control problems. The first result is a computational method for the synthesis of minimum-norm ensemble controls for time-varying linear systems. This method is extended to iterative techniques to accommodate bounds on the control amplitude, and to synthesize ensemble controls for bilinear systems. Example ensemble systems include harmonic oscillators, quantum transport, and quantum spin transfers on the Bloch system. To move towards the control of complex ensembles of nonlinear oscillators, which occur in neuroscience, circadian biology, electrochemistry, and many other fields, ideas from synchronization engineering are incorporated.

The focus is placed on the phenomenon of entrainment, which refers to the dynamic synchronization of an oscillating system to a periodic input. Phase coordinate transformation, formal averaging, and the calculus of variations are used to derive minimum energy and minimum mean time controls that entrain ensembles of non-interacting oscillators to a harmonic or subharmonic target frequency. In addition, a novel technique for taking advantage of nonlinearity and heterogeneity to establish desired dynamical structures in collections of inhomogeneous rhythmic systems is derived.

Chapter 1

Introduction

The implementation of all scientific and engineering applications is complicated by uncertainty or variation in system model parameters, for which known control techniques are often unable to successfully compensate. This issue is especially challenging when a control task must be accomplished without feedback, whether the control function must transfer a single control system between states of interest without sensitivity to an uncertain parameter set, steer a possibly uncountable collection of structurally identical systems with variation in common parameters between states that may depend on the parameters, or establish a complex dynamical configuration in a collection of interacting systems. Such highly underactuated ensemble systems appear in a variety of emerging areas in science and technology, including quantum information science, circadian biology, neuroscience, and robotics, and impact applications such as protein spectroscopy, deep brain stimulation for Parkinson's disease, and sensorless robotic manipulation. As a result, developing effective and, moreover, optimal forcing signals or synthesizing coupling functions that drive complex systems towards desired dynamical conditions is of fundamental importance [147, 119]. These and many other emerging applications involve controlling collections of structurally similar systems by using a common external signal. The microscopic scale and inherent uncertainty of the physical systems involved often makes it impractical to obtain state feedback, or the types of feedback laws that can be used are severely restricted due to the complexity of the system dynamics. These limitations present a fundamental challenge in robust and sensorless manipulation of complex ensemble systems. Therefore techniques that take advantage of the differences in dynamics or model parameters in collections of dynamical units will broadly extend the ability to manipulate complex or large-scale systems.

Novel theoretical approaches, mathematical methods, and computational techniques are required for formulating, describing, and synthesizing controls for the complex dynamics of ensemble systems in a manner that is both tractable and flexible in design. This dissertation bridges two emerging notions related to the control of complex dynamical systems. One notion is called ensemble control, and involves steering the state of very large indexed collections of dynamical systems between given states of interest [140, 139]. A complementary concept is referred to as synchronization engineering, which is the science of establishing complex periodic behavior in collections of rhythmic systems [121, 119]. In the following chapters, ideas from ensemble control and synchronization engineering are fused to produce novel analytical and computational devices for robust and optimal control of ensemble systems. Such practical and tractable ensemble control designs that are key to emerging applications including quantum control [140, 144, 206], synchronization and entrainment of neuron and chemical oscillators [95, 119, 128, 151], as well as in uncertain engineering systems [17, 18].

The control of complex ensemble systems presents several challenges. Relatively few control inputs must be used to manipulate a large system composed of many subsystems without using state feedback information, or using very limited or statistical feedback. The designed controls must be optimal with regard to a cost objective and simultaneously robust to uncertainties and disturbances inherent to the system. Finally, and most crucially, mathematical models and control design methodologies must be tractable, computationally verifiable, and readily applicable to diverse experimental systems. In this chapter, the motivating applications and basic ideas of ensemble control and synchronization engineering are reviewed.

1.1 Ensemble Control

The term ensemble control describes an emerging and challenging area in mathematical control theory that encompasses a class of problems involving the guidance of an uncountably infinite collection of structurally identical dynamical systems, which are indexed by a parameter set, by applying a common control input without the use of state feedback information. The subject originates from the study of complex spin dynamics in Nuclear Magnetic Resonance (NMR) spectroscopy and imaging (MRI), and has attracted recent interest for its potential to facilitate the manipulation of nuclear spin systems for compelling applications for quantum control and information processing.

1.1.1 Quantum Control and Information Processing

Rapidly progressing technologies based on quantum theory require the manipulation of very large ensembles of quantum systems on the order of Avogadro's number (6×10^{23}), whose states cannot be measured during the transfer, and whose dynamics are subject to dispersion in parameters such as frequency. The performance of the necessary controls must be insensitive to parameter variation across the ensemble, as well as to inhomogeneity in the applied radiofrequency (RF) control field [142, 140]. A long standing problem of significance to NMR requires the design of RF excitations that steer a given quantum ensemble between initial and target states, and whose performance is insensitive to parameter variation [125, 124, 173].

NMR exploits the property of atomic nuclei to re-emit absorbed electromagnetic energy at specific resonance frequencies when subject to a magnetic field. It is widely used in medical MRI for non-invasively visualizing organs and tissues, and for obtaining information about their biochemical composition and dynamic activity. Applications also include chemical spectroscopy for determining the structure of molecules such as complex proteins and scanning porous media in the petroleum industry. The importance of NMR has compelled significant research, so the physical principles and mathematics behind NMR are very well-understood. An acceptable control function must concurrently drive a collection of systems, with identical dynamics but parameter values unknown up to a given range, between desired initial and target states. Designing and implementing time-varying excitations, i.e., electromagnetic pulses, that steer a large quantum ensemble between states of interest is an indispensable step that enables cutting-edge applications in NMR spectroscopy, MRI, quantum computation and quantum information processing, and laser cooling [144, 140, 182, 115, 75, 38]. The capacity of nuclear magnetic resonance for manipulating quantum phenomena has progressed notably in the past decade due to powerful computational techniques for pulse design. By employing principles from ensemble control, these capabilities can require much lower computational cost, and become more flexible and widely available.

A standing goal is to enhance the sensitivity of measurement, in which the nuclear spins of a sample within a magnetic field B are manipulated using a RF pulse u. The resonant signals produced as the spin vectors realign with B are measured. The intensity depends on B and, crucially, on how well u made the intended spin transfer. A few precise, strong pulses suffice in basic cases, but not for complex transfers and biological samples, where B as

well as the maximum amplitude A and duration of u are restricted. In selective excitation, u must reorient only those nuclei with specific spin frequencies while compensating for RF field inhomogeneity. Mathematically, NMR is a control system where the state $X(t, \omega, \varepsilon)$ at time t is the orientation of nuclear spins in the sample as a function of spin frequency ω and RF attenuation ε. The system input is $u(t)$, which is a parameter-independent function of time that we design to steer the system to a target state. Using optimal control theory, a pulse design problem is formulated to, e.g., minimize error in the final state given $u(t) \leq A$. While no analytical solutions exist for this problem, commercial MRI systems employ the Shinnar-Le Roux (SLR) algorithm [173] for selective excitation. The RF field of modern NMR devices is finely adjustable, so critical gains are possible using novel pulses.

Since SLR, impressive gains have been made, such as fine selective excitation in ω and ε [124]. This involves gradient optimization of thousands of decision variables that represent u, which requires supercomputer resources. An alternative is to employ the principles of ensemble control, which is an area of mathematical control theory that concerns manipulation of a continuum of structurally identical parameter-dependent dynamical systems using a common control without feedback [140]. Inspired by this notion, pulse design was translated by pseudospectral approximation into a discrete optimization problem, which was solved and applied in experiments to enhance the excitation profile of broadband pulses [144, 143, 191]. This success has compelled the investigation of new design methods for optimal control of ensembles for use in a new generation of highly sensitive and versatile MRI systems. This method is effective for solving a variety of ensemble control problems, but may be difficult to implement for large-scale systems with variation in many parameters because of the computational complexity required for approximating control functions with sufficient accuracy [192]. Therefore, a need exists for direct and computationally efficient numerical methods for synthesizing ensemble controls that can accomplish various state transfers for a variety of systems. In particular, constructive, customizable synthesis methods that do not depend on gradient optimization are desirable. Such control synthesis methods for linear and bilinear ensembles, which satisfy minimum-norm objectives and control amplitude constraints, are presented in Chapters 2 and 3.

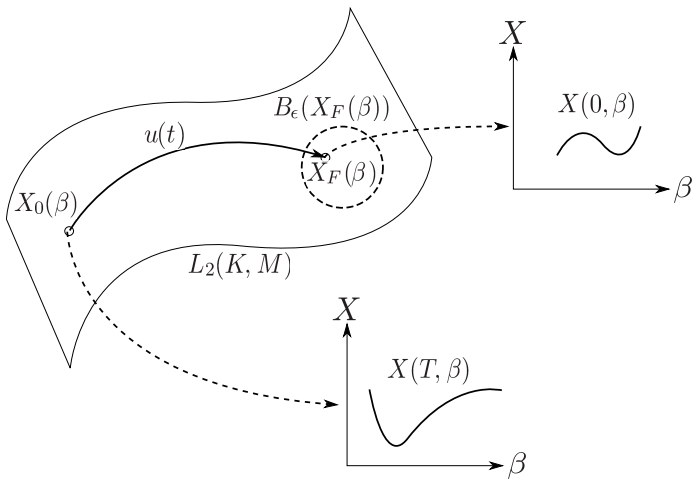

$t \in [0,T]$	$\equiv$	time
β	$\equiv$	parameter
K	$\equiv$	parameter space
X	$\equiv$	state of ensemble
M	$\equiv$	state space manifold
u	$\equiv$	control
U	$\equiv$	admissible controls
X_0	$\equiv$	initial state
X_F	$\equiv$	final state
$L_2(K,M)$	$\equiv$	function space

Figure 1.1: An illustration of the concept of ensemble control, with explanation of notation.

1.1.2 Formulation of the Ensemble Control Problem

As described above, ensemble control refers to the guidance of an uncountable collection of structurally identical dynamical systems, which are indexed by a parameter varying on a continuous set, between desired initial and terminal configurations using a common control without feedback. The most general way to precisely formulate this concept is as a continuum of dynamical systems given by

$$\dot{X}(t,\beta) = F(t, X(t,\beta), \beta, u(t)), \tag{1.1}$$

where $t \in [0,T]$ denotes time, $\beta \in K$ is an indexing parameter, $X : [0,T] \times K \to M \subset \mathbb{R}^n$ is an ensemble of state trajectories, and $u : [0,T] \to U \subset \mathbb{R}^d$ is a control input that is received by each unit of the ensemble. The state of the ensemble may be restricted to a manifold $M \subset \mathbb{R}^n$, thereby inducing a nonholonomic constraint. In Chapter 2, control systems of the form 1.1 with linear dynamics are examined, including examples such as ensembles of harmonic oscillators and the frictionless cooling of atoms in harmonic traps subject to parameter uncertainty in the spin frequency. Then in Chapter 3, systems with bilinear dynamics are studied, with a particular focus on the Bloch system, which represents nuclear spin dynamics of an atom subjected to a strong magnetic field, and which is ubiquitous in quantum control [140].

1.2 Synchronization Engineering

Natural and engineered systems that consist of ensembles of interacting nonlinear dynamical components often require an optimal hierarchical organization and dynamical structure, such as synchrony, for normal operation. Common examples include neural circuitry in the brain [219], metabolic chemical reaction systems [166] in biology, and electrical power distribution, communication, and traffic control systems [218, 54, 23, 4] in engineering. These systems are governed by highly complex, multiscale dynamics that are impacted by external cyclical processes. Their overall behavior, such as information processing by neural networks in the brain [154, 104, 107, 106, 196, 80, 78] or the propagation of power grid failure [53, 52, 65], depends on the subtle network topology of the connected units and the natural laws that control the processes within them. Their dynamics are adjusted by external stimulation, typically with predefined waveforms such as narrow pulses in deep brain stimulation (DBS) [213, 214] and cardiac pacemaking [85], square-wave light protocols for sleep cycles in circadian biology [73], or sinusoidal waveforms in phase locked loops [21].

The collective behavior of forced oscillator ensembles can be described and analyzed using phase models [228, 131], which have been effectively used in theoretical, numerical, and more recently, experimental studies [1, 122, 180, 165]. Phase resetting is a fundamental function for biological rhythms, and when resetting signals are globally applied repeatedly to an oscillator ensemble, dynamic patterns emerge, including oscillator death [228], desynchronization [213], and cluster formation [232]. Such patterns have been observed in a variety of systems including chemical oscillators [233, 232], plant and mammalian [70, 220] circadian clocks, and neuronal spiking patterns [213, 62].

The use of phase coordinate transformation for studying nonlinear oscillations has a long history [149], and was famously used with formal averaging to model collective dynamics in coupled chemical oscillations [131]. Since then, phase models have been successfully applied to investigate many synchronization phenomena [210], focusing on synchronization emerging in networks of interacting oscillators and on the response of large collections of oscillators to periodic external stimuli [186, 103]. The majority of this work has focused on modeling, so that as our understanding of such dynamical systems has solidified, the means to control such systems, and to do so in an optimal manner, have come within reach. Optimal waveforms that entrain a collection of phase oscillators with the greatest range of frequencies by weak periodic forcing have been characterized for certain oscillating chemical systems [95], and this

approach has been extended to a method for optimal entrainment of oscillating systems with arbitrary PRC [236]. In Chapter 4 the phase coordinate transformation is examined, novel theoretical and practical approaches to solving fundamental problems of optimal entrainment for a variety of objectives are derived in Chapter 5, and these concepts are extended to the manipulation of ensembles of oscillating systems in Chapter 6.

1.2.1 Control and Synchronization of Neuronal Dynamics

Technologies for brain stimulation offer an ever increasing ability to perturb the activity in small and large-scale neuronal populations. Clinical modalities such as DBS have demonstrated the efficacy of such technology for treating neurological conditions such as Parkinson's disease [80]. Similarly, optogenetics is being used to characterize the basic neuronal function in the healthy brain. Such methods have depended largely on clinical insight or experimental trial and error to date [130], and merging them with control theory is necessary for advancing beyond bulk stimulation to more precise modulation of neuronal dynamics [213, 214].

Controlling the dynamics of neuronal ensembles is a highly nontrivial engineering problem, because complex nonlinearities and irregularities appear in individual neurons and the couplings between them [213]. The under-actuated nature of most current brain stimulation modalities adds to this complexity, because a single actuator (e.g., an electrode) typically affects tens of thousands of neurons so that individual units in a population receive a common stimulus. Therefore, a tractable yet meaningful mathematical formulation and novel approaches for manipulating individual neurons in an ensemble using the same external input is crucial. The behavior of neurons and neuronal ensembles has motivated the development of numerous mathematical models whose dynamics have been studied extensively [112, 10, 189, 97, 126]. One notion that has gained wide acceptance among researchers in neuroscience and mathematical biology is the modeling of neuronal dynamics in the human brain as oscillating systems [26, 157].

In areas ranging from theoretical neuroscience to clinical neurology, devising minimum-power external stimuli that synchronize a population of coupled or uncoupled neurons, or desynchronize a network of pathologically synchronized neurons, is imperative for wide-ranging applications from the design of neurocomputers [105, 107] to neurological treatment of Parkinson's disease and epilepsy [9, 19, 196]. Nonlinear oscillators have served as models of neuronal

dynamics in neuroscience for many decades [179, 58, 99], and the intrinsic occurrence and extrinsic imposition of entrainment in networked oscillators is of particular interest [20, 201]. Phase model reduction is an especially compelling approach for constructing simplified yet accurate models that capture essential overall properties of such oscillating systems [228, 131].

Several studies have been motivated by the prospect of using dynamical systems theory to improve the effectiveness of DBS as a clinical therapy for epilepsy and Parkinson's disease [214, 177, 80]. Concurrently, others have concentrated on the use of phase models in order to attain desired design objectives for electrochemical [121, 163] and neural [105, 108] systems, including recent work that approaches the use of phase models in neuroscience from a control theoretic perspective [221, 160]. The control of neural spiking using minimum energy inputs with constrained amplitude and charge balancing has also recently been examined with the aid of phase models [46, 47]. These studies have demonstrated that phase-model reduction provides a practical approach to synthesizing near-optimal controls that achieve design goals for oscillating neural systems.

The desired outcome of such investigation is to understand how to manipulate neuronal dynamics in experiments, as well as in a clinical setting in order to treat neurological disorders using therapies such as deep brain stimulation (DBS) [152, 145, 214]. As a result, interest is increasing in developing methods for controlling neuronal ensembles, and outlining the limits on possible actuation [155, 35]. This requires mathematical models that appropriately represent the phenomenology of neural ensembles and brain stimulation, and are also tractable for control design. A modeling and control technique is presented in Chapter 6 that, together with the model identification method in Section 4.4, is a promising step towards this goal.

1.2.2 Electrochemical Oscillators and Neurocomputing

In addition to the compelling scientific questions and clinical applications that motivate this work from the perspective of neuroscience, the control of complex rhythmic systems has important implications for electrochemistry [116, 121, 119, 190]. Complex oscillatory behavior is known to arise in many electrochemical systems, and such phenomena have been proposed as the basis of an electrochemical computing device [105, 107]. Such devices, which are called neurocomputers, are intended to function using the principles that govern computation in

the human brain. Arrays of coupled electrochemical oscillators have been suggested as a platform for construction such devices, with components on a micro- or even nano-scale. The techniques in Chapter 6 provide robust principles for bringing complex collections of dynamical systems to a desired condition using low amplitude controls that leave the local inherent behavior intact. Methods for achieving phase-assigned synchronization in electrochemical oscillator ensembles takes a step towards micro-scale electrochemical computing.

1.3 Organization

The rest of the dissertation is organized as follows. Chapter 2 formulates the most fundamental type of ensemble control problem, in which the dynamics of each system are linear. The results on ensemble controllability for this case are reviewed, and a numerical method for minimum-norm ensemble control synthesis is presented. In Chapter 3, the technique in Chapter 2 is extended to bilinear ensembles, in which the dynamics of the individual systems feature products of the state and control. The remaining chapters are devoted to the optimal synchronization of oscillating systems. Chapter 4 contains a derivation of the phase coordinate transformation, including a computational method for performing the model reduction, examples, and a phase model identification technique for rhythmic systems with unknown dynamics. In Chapter 5, phase reduction, ergodic averaging, and the calculus of variations are used to formulate and solve optimal entrainment problems for nonlinear oscillating systems, with design objectives that including minimum input energy, fast entrainment, and subharmonic forcing. Then in Chapter 6, these solutions are extended to problems involving the optimal entrainment of ensembles of oscillators, and the design of dynamic configurations in such ensembles. Finally, Chapter 7 contains concluding remarks and an outlook for continuing work on open problems in ensemble control and synchronization engineering.

1.4 Contributions

Several novel contributions described in this dissertation merit attention. The first is the computational ensemble control synthesis method for linear systems based on the singular

value decomposition (SVD), which is described in Section 2.2 [239, 185]. This method provides a tractable means of computing high-resolution minimum-norm ensemble controls for very large collections of dynamical systems, and lies at the interface between control theory, integral operator theory, and numerical linear algebra. This method is extended to the iterative fixed-point technique for synthesizing ensemble controls for bilinear systems, which is presented in Section 3.1. This method is tractable for solving large-scale fixed-endpoint optimal control problems, and does not depend on computationally costly gradient optimization steps [237]. Next, the straightforward computational technique for computation of the phase response curve (PRC) of an oscillator in Section 4.2 and the practical model identification method in Section 4.4 constitute a robust framework for analyzing and controlling synchronization in real physical systems [235]. The theoretical framework in Chapter 5 facilitates the modeling and solution of a variety of entrainment problems using weak forcing. In particular, it is shown that minimum-energy frequency control of an oscillator is achieved using a re-scaled PRC waveform in Section 5.2 [236], and that the fastest entrainment is achieved using a re-scaled derivative of the PRC as the input waveform in Section 5.3 [235]. In addition, expressions for optimal subharmonic entrainment, where the frequency of the input and state oscillations are related by a rational number, are derived in Section 5.4 [240]. Finally, optimal waveforms for the entrainment of ensembles of structurally similar nonlinear oscillators are derived in Section 6.2 [238, 240], and a novel theoretical approach and constructive technique for engineering phase-assigned synchronization in such ensembles is presented in Section 6.4.

Chapter 2

Control of Linear Ensemble Systems

The implementation of all control tasks in science and engineering is complicated by uncertainty or variation in system model parameters, for which known control techniques are often unable to successfully compensate. This issue is especially challenging when the control task must be accomplished without feedback, whether the control input must transfer a single control system between states of interest without sensitivity to an uncertain parameter set, or steer a possibly uncountable collection of structurally identical systems with variation in common parameters between states that may depend on the parameters. In this chapter, we consider control design problems for which an acceptable control input must concurrently drive a collection of systems, with identical dynamics but parameter values unknown up to a given range, between desired initial and target states.

The theoretical investigation of ensemble control begins with the notion of ensemble controllability, which determines the existence of controls that achieve various types of state transfers for a system of interest. The necessary and sufficient conditions for ensemble controllability of finite-dimensional time-varying linear systems for transfers between states in Hilbert space have been recently derived [138]. These conditions depend on the singular system [162] of the operator characterizing the system dynamics, which can in turn be used to represent the minimum norm control that accomplishes the transfer as an infinite sum of weighted eigenfunctions [139]. This method was used to synthesize optimal ensemble controls for a harmonic oscillator system, for which the resulting eigenfunctions are the well-known family of prolate spheroidal wave functions [139]. This special structure facilitates synthesis of the controls in this case, as well as the computation of optimal controls with bounded amplitude by solving a constrained convex optimization problem [139]. However, more importantly for the realization of ensemble control applications, there is a need

to develop numerical methods for synthesizing these ensemble controls, because analytical solutions are available only in the simplest cases. In this chapter, an accurate, computationally efficient, optimization-free algorithm based on the singular value decomposition (SVD) is presented that approximates ensemble controls of minimum norm for finite-dimensional time-varying linear systems. This method enables the application of ensemble control to engineering problems involving complex, time-varying, and high-dimensional linear dynamic systems [239, 185].

Although first motivated by the necessity to control large collections of similar systems, the mathematical devices produced by investigating ensemble control can also be used to approach any open-loop control application in which the system response must be immune to uncertainty in model parameters. For instance, harmonic oscillators are widely used to approximate periodic phenomena in a variety of scientific and engineering applications where the frequency of oscillation may not be known exactly, but rather is confined to a given range [14, 27]. Harmonic oscillators often appear in quantum-electrodynamics, and steering such quantum systems using electromagnetic fields is a subject of widespread interest [156].

The following section contains a review of the notation and mathematical foundation for ensemble control theory of finite-dimensional time-varying linear systems. Afterwards we formulate an accurate, stable, and computationally efficient numerical method based on the singular value decomposition for constructing minimum norm ensemble controls for finite-dimensional time-varying linear systems [239]. The crucial innovation concerns the numerical approximation of the singular system of the Fredholm integral operator of the first kind [162] that characterizes the dynamics of a linear ensemble system, as well as the synthesis of the unique minimum norm control that accomplishes a desired transfer in function space. In addition, the technique is extended to a fast, iterative method for solving the same problem when a constraint on the control amplitude is added. These techniques are promising because they produce high resolution ensemble control functions, of fine time discretization, which sidestep the need for computationally costly gradient optimization steps. The method is applied to control the canonical ensemble control system, which consists of a continuum of harmonic oscillators, in order to demonstrate the effectiveness of our new method for accomplishing complex state transfers. Additional examples of linear systems with higher dimension and with variation in several parameters are examined as well.

2.1 Linear Ensemble Control Theory

The aim of ensemble control is to simultaneously manipulate a continuum of dynamical systems, which are governed by internal and external dynamics that depend on a parameter varying over a compact indexing set, by applying the same open-loop control input to each. In this section, we review the basic definitions and the fundamental theoretical results that enable ensemble control synthesis for finite-dimensional time-varying linear systems.

Consider a parameterized family of dynamical systems indexed by a parameter β varying over a compact set K, given by

$$\begin{gathered}\dot{X}(t,\beta) = A(t,\beta)X(t,\beta) + B(t,\beta)u(t), \\ X \in M \subset \mathbb{R}^n, \quad \beta \in K \subset \mathbb{R}, \quad u \in U \subset \mathbb{R}^m,\end{gathered} \tag{2.1}$$

where $A(t,\beta) \in \mathbb{R}^{n\times n}$ and $B(t,\beta) \in \mathbb{R}^{n\times m}$ have elements that are real L_∞ and L_2 functions, respectively, defined on a compact set $D = [0,T] \times K$, and are denoted $A \in L_\infty^{n\times n}(D)$ and $B \in L_2^{n\times m}(D)$. The ensemble controllability conditions for the system (2.1) depend on the existence of an open-loop control $u : [0,T] \to U$ that can steer the instantaneous state of the ensemble $X(t,\cdot) : K \to M$ between any points of interest in the Hilbert space of functions on K. Let $\mathcal{H}_T = L_2^m[0,T]$ denote the set of m-tuples, whose elements are real square-integrable functions defined on $0 \le t \le T$, with an inner product defined by

$$\langle g, h\rangle_T = \int_0^T g'(t)h(t)dt, \tag{2.2}$$

where $'$ denotes the transpose. Similarly, let $\mathcal{H}_K = L_2^n(K)$ be equipped with an inner product

$$\langle p, q\rangle_K = \int_K p'(\beta)q(\beta)d\mu(\beta), \tag{2.3}$$

where μ is the Lebesgue measure. With well-defined addition and scalar multiplication, $\mathcal{H}_T$ and $\mathcal{H}_K$ are separable Hilbert spaces, where $||\cdot||_T$ and $||\cdot||_K$ denote their respective induced norms. Ensemble controllability is formulated within this Hilbert space framework as follows.

Definition 1: (*Ensemble controllability* [138]) We say that the family (2.1) is ensemble controllable on the function space $\mathcal{H}_K$ if for all $\varepsilon > 0$, and all X_0, $X_F \in \mathcal{H}_K$, there exists

$T > 0$ and an open loop piecewise-continuous control $u \in \mathcal{H}_T$, such that starting from $X(0,\beta) = X_0(\beta)$, the final state $X(T,\beta) = X_T(\beta)$ satisfies $||X_T - X_F||_K < \varepsilon$.

In other words, the system (2.1) is ensemble controllable if it is possible to guide it from X_0 to X_F in the space $\mathcal{H}_K$, where the acceptable range of $T \in (0,\infty)$ may depend on ε, K, and U. It is useful to note that ensemble controllability is defined in the sense of approximate controllability [41, 37]. Necessary and sufficient conditions have been determined for the ensemble controllability of finite-dimensional time-varying linear systems, and are based on the Fredholm integral operator that characterizes the system dynamics [139], which is obtained as follows. Given the initial state $X(0,\beta) = X_0(\beta)$ of the system (2.1), the variation of parameters formula gives rise to the solution

$$X(T,\beta) = \Phi(T,0,\beta)X_0(\beta) + \int_0^T \Phi(T,\sigma,\beta)B(\sigma,\beta)u(\sigma)d\sigma, \tag{2.4}$$

where $\Phi(t,0,\beta)$ is the transition matrix for the system $\dot{X}(t,\beta) = A(t,\beta)X(t,\beta)$. Our goal is for the terminal state to equal the target state in the function space $\mathcal{H}_K$, so setting $X(T,\beta) = X_F(\beta)$, pre-multiplying by $\Phi(0,T,\beta)$ and rearranging results in the integral operator equation

$$(Lu)(\beta) = \int_0^T \Phi(0,\sigma,\beta)B(\sigma,\beta)u(\sigma)d\sigma = \xi(\beta), \tag{2.5}$$

where $\xi(\beta) = \Phi(0,T,\beta)X_F(\beta) - X_0(\beta)$. The theory of ensemble controllability for finite-dimensional time-varying linear systems and the derivation of minimum norm controls can be reduced to the solvability and applied solution of the above integral equation, in either the exact or approximate sense. Implicit controllability conditions have been derived based on the associated input-to-state operator L in (2.5) within the Hilbert space setting described above [139]. This operator, as defined in equation (2.5), satisfies $L \in \mathcal{B}(\mathcal{H}_T, \mathcal{H}_K)$, where $\mathcal{B}(\mathcal{H}_T, \mathcal{H}_K)$ is the set of bounded linear operators from $\mathcal{H}_T$ to $\mathcal{H}_K$. Furthermore, because the Hilbert spaces $\mathcal{H}_T$ and $\mathcal{H}_K$ with inner products defined by (2.2) and (2.3), respectively, are both separable, it follows that L has the adjoint L^* satisfying

$$\langle \xi, Lu \rangle_K = \langle L^*\xi, u \rangle_T, \quad \forall\, \xi \in \mathcal{H}_K, \quad u \in \mathcal{H}_T. \tag{2.6}$$

We omit the subscript on the inner product when it is clear from the context. The conditions characterizing ensemble controllability are related to the singular system of the operator L, which requires the following important definition.

A spectral decomposition, called the singular system, of the operator L is used to produce an infinite eigenfunction series expansion for the $u \in \mathcal{H}_T$ of minimum norm that satisfies (2.5) with sufficient accuracy.

Definition 2: *Singular System* [79]: Let Y and Z be Hilbert spaces and $L : Y \to Z$ be a compact operator. If (σ_n^2, ν_n) is an eigensystem of LL^* and (σ_n^2, μ_n) is an eigensystem of L^*L, namely, $LL^*\nu_n = \sigma_n^2\nu_n$, $\nu_n \in Z$, and $L^*L\mu_n = \sigma_n^2\mu_n$, $\mu_n \in Y$, where $\sigma_n > 0$ $(n \geq 1)$, and the two systems are related by the equations $L\mu_n = \sigma_n\nu_n$ and $L^*\nu_n = \sigma_n\mu_n$, we say that (σ_n, μ_n, ν_n) is a singular system of L.

It can be shown that the operator L in (2.5) is compact [139], and hence LL^* and L^*L are both compact, self-adjoint, and nonnegative operators. By the Spectral theorem, L^*L can be represented in terms of its positive eigenvalues, namely, $L^*Ly = \sum_n \sigma_n^2 \langle y, \mu_n \rangle \mu_n$ for all $y \in \mathcal{H}_T$. Moreover, because $L^*L\mu_n = \sigma_n^2\mu_n$, the relations $L\mu_n = \sigma_n\nu_n$ and $L^*\nu_n = \sigma_n\mu_n$ follow by taking $\nu_n = (1/\sigma_n)L\mu_n$. Note that the singular system is the infinite dimensional analogue of the singular value decomposition of a matrix.

Suppose that (σ_n, μ_n, ν_n) is a singular system of the operator L as defined in (2.5), which is compact [138]. The following theorem provides necessary and sufficient conditions for ensemble controllability of finite-dimensional time-varying linear systems with input-to-state operator L.

Theorem 1: [139] The family of systems (2.1) is ensemble controllable on the function space $\mathcal{H}_K$ if and only if for any given initial and final state $X_0\, X_F \in \mathcal{H}_K$, at time $t = 0$ and $t = T < \infty$ respectively, and for $\xi = \Phi(0, T, \beta)X_F - X_0$, the conditions

$$(i) \quad \sum_{n=1}^{\infty} \frac{|\langle \xi, \nu_n \rangle_K|^2}{\sigma_n^2} < \infty, \tag{2.7}$$

$$(ii) \quad \xi \in \overline{\mathcal{R}(L)}, \tag{2.8}$$

hold, where L is the input-to-state operator of the system (2.1) defined in equation (2.5), with $\overline{\mathcal{R}(L)}$ denoting the closure of the range space of L, and the collection of triples (σ_n, μ_n, ν_n) is a singular system of the linear operator L. Moreover, the control

$$u = \sum_{n=1}^{\infty} \frac{1}{\sigma_n} \langle \xi, \nu_n \rangle \mu_n \tag{2.9}$$

satisfies $\langle u, u\rangle \leq \langle u_0, u_0\rangle$ for all $u_0 \in \mathcal{U}$ and $u_0 \neq u$, where $\mathcal{U}$ is the set of solutions to (2.5) given by $\mathcal{U} = \{v \,|\, Lv = \xi \text{ with } (i) \text{ and } (ii)\}$. For further details we refer the reader to the original work on this subject [138, 139].

Because singular systems and hence optimal ensemble controls cannot be derived analytically except for in the simplest cases, such as that of the prolate spheroidal wave function [139], an accurate and efficient numerical method for approximating the former is a prerequisite for applying this new theory. Given an appropriate numerical approximation to the singular system (σ_n, μ_n, ν_n) for the operator L of an ensemble controllable system, the series (3.17) can be truncated to synthesize an approximation to u that results in $||X_T - X_F||_K < \varepsilon$ as desired. In addition, a numerical test of the criteria (2.7) for ensemble controllability is a natural extension of such a framework, which we present in the following section.

2.2 Numerical Synthesis of Minimum-Norm Ensemble Controls for Linear Systems

Theorem 1, together with Definition 2, suggests a natural method for approximating solutions to (2.5) of minimum norm [239]. The integral operator equation $Lu = \xi$ can be approximated by a linear matrix equation, so that the singular system (σ_n, μ_n, ν_n) of L can be approximated by the singular value decomposition of this matrix. The approximation is carried out using the following discretization. Let $\{\beta_j\}$ be a collection of points that are uniformly distributed throughout the space K for $j = 0, 1, 2, \ldots, P$, and let $\{t_k\}$ be a collection of points that linearly interpolate the time domain $[0, T]$ for $k = 0, 1, \ldots, N$, including endpoints, with $t_k - t_{k-1} = \delta$. Thus for each for each $\beta \in \{\beta_j\}$, and using the time discretization $\{t_k\}$, we make the Riemann quadrature approximation

$$\begin{aligned}(Lg)(\beta) &= \int_0^T \Phi(0, t, \beta) B(t, \beta) g(t) \mathrm{d}t \\ &= \sum_{k=1}^{N} \int_{t_{k-1}}^{t_k} \Phi(0, t, \beta) B(t, \beta) g(t) \mathrm{d}t \\ &\approx \sum_{k=1}^{N} \delta \Phi(0, t_k, \beta) B(t_k, \beta) g(t_k) \end{aligned} \tag{2.10}$$

Hence the action of the operator L on a function $g \in \mathcal{H}_T$ can be approximated by the action of a block matrix $W \in \mathbb{R}^{nP \times mN}$, with $n \times m$ blocks $W_{jk} = \delta\Phi(0, t_k, \beta_j)B(t_k, \beta_j)$, on a vector $\hat{g} \in \mathbb{R}^{mN}$, with N blocks $\hat{g}_k = g(t_k)$ of dimension $m \times 1$. This can be seen by observing that $(Lg)(\beta_j)$ is approximated by (2.10) for each β_j by applying $\mathcal{W}_{jN}$ to $\hat{g}$, where $\mathcal{W}_{jk} = [\ W_{j1} \quad W_{j2} \quad \ldots \quad W_{jk}\ ] \in \mathbb{R}^{n \times mk}$.

Recall that the singular value decomposition (SVD) of the matrix W is given by $W = U\Sigma V'$, where $\bar{u}_j$ and $\bar{v}_j$ are the orthogonal columns of U and V, respectively, which correspond to the singular value s_j [50]. The diagonal matrix Σ contains the singular values s_j on the main diagonal. It then follows that $WW'\bar{u}_j = s_j^2\bar{u}_j$ and $W'W\bar{v}_k = s_j^2\bar{v}_k$. Therefore the SVD $(s_j, \bar{v}_j, \bar{u}_j)$ of the matrix W approximates the singular system (σ_j, μ_j, ν_j) of the operator L, where $\bar{v}_j$ and $\bar{u}_j$ are discretizations of μ_j and ν_j, respectively. It is important to note that the use of the SVD to approximate solutions to Fredholm integral equations has been previously investigated [223, 92, 91, 11], although primarily in the context of least-squares problems, rather than minimum norm solutions.

Now suppose that $\hat{\xi} \in \mathbb{R}^{nP}$ is given by $\hat{\xi}_k = \xi(\beta_k)$ for a function $\xi \in \mathcal{H}_K$. As a result of the projection theorem in normed linear spaces, the minimum norm solution $\hat{g}^*$ that satisfies $W\hat{g} = \hat{\xi}$ is given by $\hat{g}^* = W'z$ where $WW'z = \hat{\xi}$ [146], so that applying basic properties of the SVD yields

$$\hat{g}^* = \sum_{j=1}^{q} \frac{\hat{\xi}'\bar{u}_j}{s_j}\bar{v}_j \tag{2.11}$$

for an appropriate $q < nP$ chosen to avoid the accumulation of roundoff errors. The components $\hat{u}_1^*, \ldots, \hat{u}_m^*$ of the synthesized minimum norm control $\hat{u}^*$ are therefore given by $\hat{u}_k^* = \{\hat{g}_{k+m(j-1)}^*\}_{j=1}^N$. Note that the time and parameter discretizations N and P must be chosen such that $nP \leq mN$, so that the pair $(W, \hat{\xi})$ represents an underdetermined system and therefore a minimum norm and not a least squares approximation problem.

The use of a Riemann sum quadrature formula to approximate the action of a Fredholm integral operator of the first kind by a matrix, so that the SVD can be used to approximate the singular system of the operator, has previously been examined as part of a least-squares type method [94]. An analysis of numerical methods for approximating solutions to such integral equations, as well as an examination of accuracy and conditioning issues, has also been performed [92]. The latter work includes a discussion of the Picard criterion, which

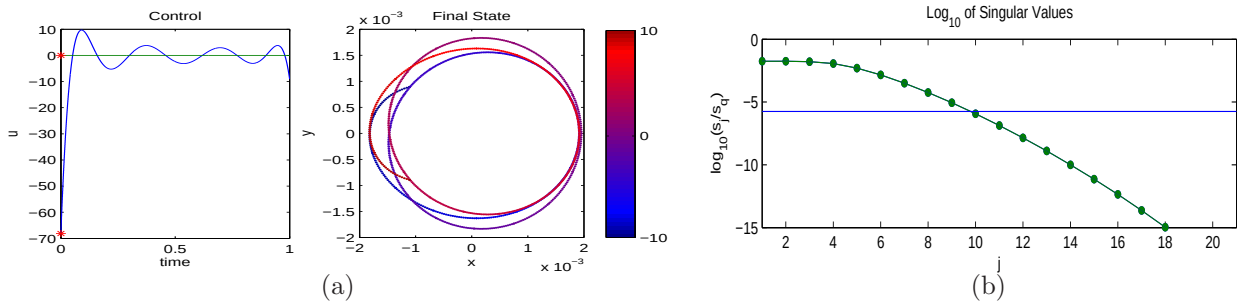

Figure 2.1: Simulation of system ensemble (2.12) for $N = 20000$, $T = 1$, $P = 20$, and $\omega \in [-10, 10]$. The initial and target states are $X_0(\omega) = (1, 0)'$ and $X_F(\omega) = (0, 0)'$. The matrix W is computed in about 5 seconds, and the SVD is computed in under 1 second. (a) The optimal control law $(u_1(t), u_2(t))$ for $t \in [0, 1]$ (left), and the final states for all systems $\omega \in [-10, 10]$. (b) The singular values $\{s_j\}$ of W on a $\log_{10}$ scale, with the $\tau_r = 10^4$ cutoff indicated. Here $q = 18$ (9 each for u_1 and u_2) singular vectors are used to synthesize the control.

asserts that there exists a square integrable solution to the integral equation (2.5) only if (2.7)(i) holds.

The most important computational issue is the prevention of the aggregation of numerical errors. These first arise from computation of the transition matrix Φ, which must be done using numerical integration unless Φ has a tractable analytical form. A practical relative error tolerance for solving ODE systems is $\mathcal{O}(10^{-6})$. Another source of numerical error arises from computation of the SVD. In essence, the solution (2.11) reflects the use of a pseudoinverse, i.e., $\hat{g} = W^{\dagger}\hat{\xi}$. In order to prevent numerical conditioning errors from dominating the synthesized control, it is appropriate to choose q in (2.11) such that the corresponding first and last singular values used satisfy $s_1/s_q < 10^4$. Let us denote this as the relative truncation factor τ_r. This relative tolerance effectively guarantees that the resulting pseudoinverse solution is well-conditioned. Certain convergence issues related to the optimal truncation of SVD-based least squares solutions to first kind Fredholm equations have been investigated for noisy data [223]. Further results of previous work on the consistency, stability, convergence, and regularity of numerical solutions to Fredhom equations of the first kind are discussed in Section 2.5.

2.3 Examples of Linear Ensemble Transfers

In order to illustrate the performance of the above method, several example simulations of control synthesis for ensemble transfers are presented below.

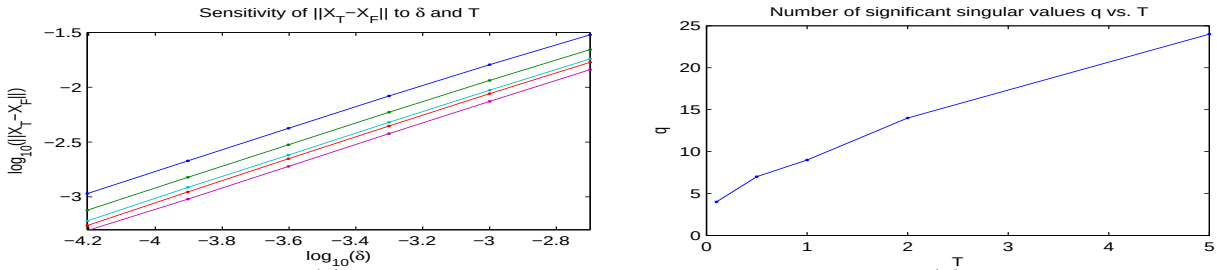

(a) (b)

Figure 2.2: The simulation in Figure 2.1 is repeated for different values of time horizon T and time step δ, where $N = T/\delta$, and $P = 40$ is used in each instance. (a) The norm of the error in the final state is plotted as a function of $1/\delta = N/T$. The slope of the lines is very close to 1, so that the error is proportional to δ. The lines correspond to $T = 0.1$, 0.5, 2, 1, and 5, from top to bottom, hence a longer time horizon does not necessarily result in improvement. (b) The number of significant singular values q is plotted as a function of T.

2.3.1 Ensembles of Harmonic Oscillators

Consider the optimal control of an ensemble of harmonic oscillators, which has been previously examined in detail [139]. This system was proven to be ensemble controllable, and the eigenfunctions of the operator that characterizes the system dynamics are related to the family of prolate spheroidal wave functions. The dynamics are

$$\frac{\mathrm{d}}{\mathrm{d}t}\begin{bmatrix} x(t,\omega) \\ y(t,\omega) \end{bmatrix} = \begin{bmatrix} 0 & -\omega \\ \omega & 0 \end{bmatrix}\begin{bmatrix} x(t,\omega) \\ y(t,\omega) \end{bmatrix} + \begin{bmatrix} u_1(t) \\ u_2(t) \end{bmatrix}, \tag{2.12}$$

where $\omega \in K = [\omega_1, \omega_2] \subset \mathbb{R}$, the instantaneous state is $X(\cdot,\omega) = (x(\cdot,\omega), y(\cdot,\omega))' \in \mathcal{H}_K$, and the control vector is $U = (u_1, u_2)' \in \mathcal{H}_T$. We apply the method described in Section 2.2 to solve an optimal ensemble control problem for the system (2.12), and the results are shown in Figure 2.1. The transition matrix Φ is evaluated analytically for this example. The control is computed more accurately than in previous results [139], and its performance is similar. In addition, the results of further numerical experiments that determine the sensitivity of the error $\|X_T - X_F\|_K$ to the choice of time horizon T and time discretization $\delta = T/N$ are shown in Figure 2.2. The error in the final state of the ensemble is proportional to the time step δ, which provides a means to calibrate the number N of time discretization points.

This method can also be used to solve more challenging problems, for example where the initial and target states X_0 and X_F are non-constant functions of ω in the state space, which is

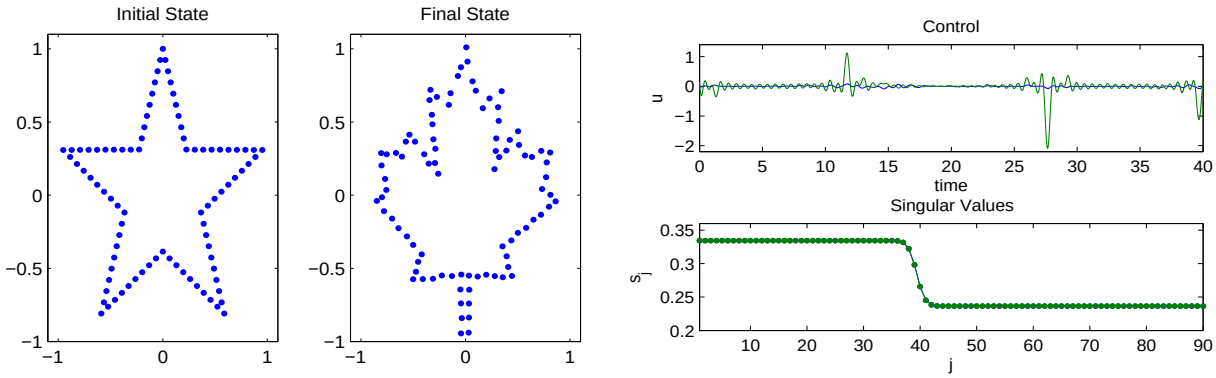

(a) (b)

Figure 2.3: Simulation of system ensemble (2.12) for $N = 20000$, $T = 40$, $P = 89$, and $\omega \in [-10, 10]$, where the initial and target states X_0 and X_F are arrangements of the $P + 1$ oscillators in star and leaf shaped images in the plane, respectively. The average error in the final states of the oscillators is 3.03×10^{-4}, and the maximum error is 0.0167. (a) Initial (left) and actual final (right) states are plotted. (b) The control that accomplishes the transfer (top), and the spectrum of the SVD (bottom) are shown. Observe that the latter differs in form from that which results from the simulation in Figure 2.1, i.e., the singular values do not decay to zero, and all of the singular vectors are used to synthesize the control.

referred to as a non-uniform transfer. The control synthesis technique can be applied to steer an ensemble of harmonic oscillators (2.12) between arbitrary initial and target configurations in the plane. An example result of such a simulation is shown in Figure 2.3, and we encourage the reader to view a video of the transfer [234]. This example is in fact related to a complex problem of importance to the field of NMR in which the initial and target states also depend on system parameters. In certain experiments specific sub-collections of quantum systems must be excited based on parameter values or the physical position in the sample under study by using so-called selective pulses [124, 183]. Controls that can create arbitrary patterns in the terminal state of the ensemble as a function of system parameters are desired.

An important question concerns the proper sampling over the space K, and whether the resulting solution does in fact yield an appropriate allocation of the continuous ensemble in the case of a non-uniform transfer. This issue will be further explored in Section 2.5. First, observe that for the basic uniform ensemble transfer illustrated in Figure 2.1, the singular values decay rapidly to zero, hence relatively few samples in K are required. In order to examine the issue of sampling for non-uniform transfers, consider the example of steering the same ensemble of harmonic oscillators from an arrangement in the form of a circle, i.e., $X_0(\omega) = (\cos(\pi\omega/10), \sin(\pi\omega/10))$, to the form of a square, as shown in Figure 2.4(a). For a time discretization of $N = 20000$ for $T = 15$, using a sampling of $P = 41$ yields a control that steers the sampled systems to the desired locations. When the same control is applied to an

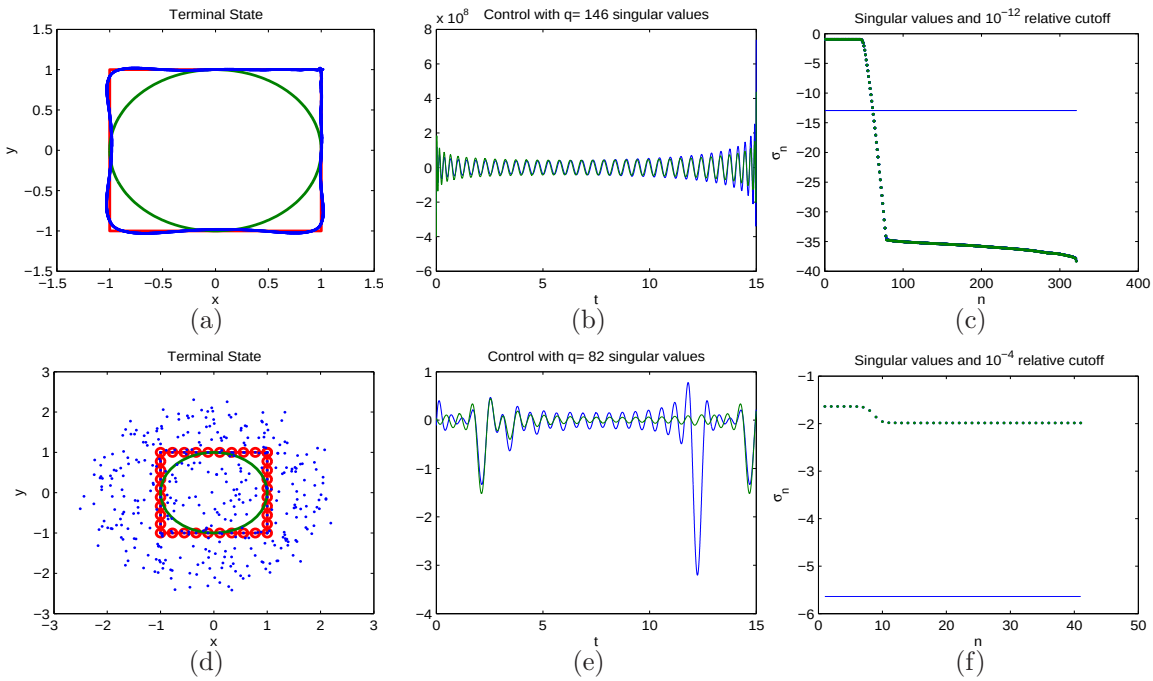

Figure 2.4: Simulation of system ensemble (2.12) using $N = 10000$, $T = 15$, and $\omega \in [-10, 10]$, where the initial state as a function of ω is $X_0(\omega) = (\cos(\pi\omega/10), \sin(\pi\omega/10))$ and the target state X_F is distributed uniformly in a square figure centered at the origin. For the target state, the systems corresponding to $\omega = 10$ and $\omega = -10$ are both located at the Northeast corner, and samples are distributed uniformly along the square shape. The top panels, for a simulation with $P = 321$ sample points on K, show (a) the initial (green), target (red), and terminal (blue) states simulated using $P = 3210$, (b) the optimal control, and (c) the corresponding singular values with relative truncation factor $\tau_r = 10^{12}$. Note that a high amplitude control input is required. The bottom panels, for a simulation with $P = 41$ sample points on K, show (d) the initial (green), target (red circles), and terminal (blue) states simulated using $P = 410$, (e) the optimal control, and (f) the corresponding singular values with relative truncation factor $\tau_r = 10^4$. Note that in panel (d), the up-sampled points are not steered to the target location.

up-sampling of $P = 410$ systems, the additional systems are not guaranteed to be steered to the target figure. The results of the simulation are shown in Figures 2.4(d) to 2.4(f), where it can be seen that the singular values do not decay to zero. If a sampling of $P = 321$ is used in the control synthesis, then the resulting control has a very high amplitude, and the sampled systems are not steered exactly to the desired terminal state. However, very crucially, when the same control is applied to an up-sampling using $P = 3210$ systems, all of these are steered to lie along the square-shaped line drawn out by the sampled systems. Note, furthermore, that the singular values of the operator do eventually decay to negligible values. A relative truncation factor of $\tau_r = 10^{12}$ is used to synthesize the control. The consistency of representations of the prolate spheroidal wave function using discrete prolate spheroidal sequences has been examined [174], and the latter were used to synthesize the same uniform ensemble transfer as shown in Figure 2.1 [141]. Nevertheless, for general ensemble control

problems the relationship between the discretizations of $[0, T]$ and K is an important open question.

2.3.2 Applications to Quantum Transport Problems

Adiabatic processes are ubiquitous in cold atom physics, nuclear magnetic resonance, optics and other fields [187, 200, 3, 39]. Although useful for preparing states robustly with respect to perturbations, these processes may become impractical due to their long duration. This has prompted a surge of theoretical and experimental activities to find shortcuts to adiabaticity. At the heart of modern quantum technology lies the efficient frictionless cooling of trapped atoms [135, 63, 33]. Frictionless cooling of atoms in a harmonic trap involves changing the harmonic frequency of the trap to some lower final value, while keeping the populations of the initial and final levels invariant, thus without generating friction and heating. Achieving this goal in minimum time, instead of adiabatically, is highly desirable in order to minimize the effect of decoherence, which is the undesirable interaction of the system with the environment. Many important applications can be realized given such capability, which can be used to reach extremely low temperatures inaccessible by standard cooling techniques [135], to reduce the velocity dispersion and collisional shifts for spectroscopy and atomic clocks [63], and to perform adiabatic quantum computation [3]. It is also closely related to the problem of steering a system between two thermal states in minimum time, as for example in the transition from graphite to diamond [193]. Optimal frictionless atom cooling in harmonic traps has been recently examined. The goal was to optimally decrease (cool) the frequency of the trapping potential while keeping the populations of the energy levels in the initial and final configuration constant. Time-optimal controls of a bang-bang form and a synthesis of optimal controlled trajectories for frictionless atom cooling were derived [204, 205].

Problems involving optimal quantum transport, such as those listed above, are also subject to parameter variation and uncertainty, which may be of significance to control design. For example, a particular optimal quantum transport problem may be formulated as the optimal control of a linear time-invariant system [206], with uncertainty or inhomogeneity in the trap velocity ω, so that the dynamics are given by

$$\mathrm{d}X = A(t, \omega)X + Bu, \tag{2.13}$$

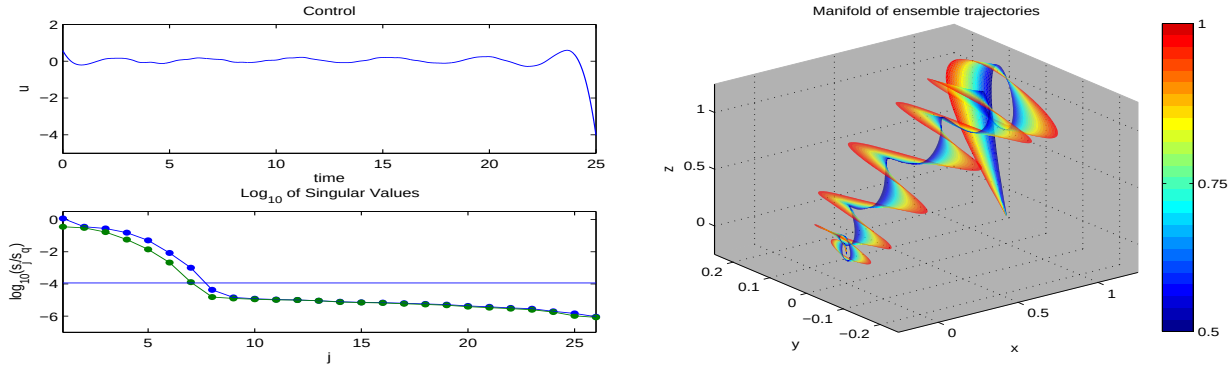

(a) (b)

Figure 2.5: Simulation of the ensemble system (2.13) with initial and target states $X_0 = (0,0,0)'$ and $X_F = (0,0,1)'$. The control is computed for $N = 25000$, $T = 25$, and $P = 26$. The system is simulated using a Runge-Kutta ODE solver, and the error between the terminal and target states is $||X_T - X_F||_K \approx 2.7\times10^{-3}$. (a) The minimum norm control (top) synthesized using $q = 14$ eigenvectors, with corresponding singular values plotted (bottom). The spectrum of the SVD decays quickly, as in the example in Figure 2.1. (b) Manifold of ensemble trajectories.

$$A(t,\omega) = \begin{bmatrix} 0 & 1 & 0 \\ -\omega^2 & 0 & \omega^2 \\ 0 & 0 & 0 \end{bmatrix}, \quad B = \begin{bmatrix} 0 \\ 0 \\ 1 \end{bmatrix},$$

where $X = (x_1, x_2, x_3)'$ and u is a scalar control input. In the example shown in Figure 2.5, the uncertain trap velocity is $\omega \in [0.5, 1]$, the transfer time is $T = 25$, and $X_0 = (0,0,0)'$ and $X_F = (1,0,0)'$ are initial and target states, respectively. The optimal ensemble control generated using a discretization $N = 25000$ and sampling $P = 26$, as well as the corresponding singular values, is shown in Figure 2.5(a). The trajectories depend continuously on the parameter ω, so that the ensemble trajectory in effect sweeps through a manifold in $\mathbb{R}^3$, which is shown in 2.5(b).

2.4 Minimum-Norm Amplitude-Constrained Ensemble Controls for Linear Systems

The method for synthesizing minimum-norm ensemble controls for linear systems that was presented in Section 2.2 can be extended to solve problems where the amplitude of the control input is constrained. An algorithm has been previously proposed for computing bounded-variable least squares (BVLS) [203]. However, this algorithm was designed for

highly over-determined systems with few variables and many constraints, such as in least squares fitting of noisy data for the purpose of parameter estimation. In the present case, the system is highly under-determined, with tens of thousands of variables corresponding to the time-discretization of a control input, and many fewer constraints created through approximation of (2.5) by applying (2.10). Therefore, a fast iterative technique is proposed here to solve constrained linear ensemble control problems, which converges when a solution exists.

Consider the addition of constraints to the minimum-norm ensemble control problem in Section 2.2, to produce the modified problem

$$\begin{aligned} \min \quad & \mathcal{J}[\hat{g}] = \hat{g}'\hat{g} \\ \text{s.t.} \quad & W\hat{g} = \hat{\xi} \\ & l_i \leq \hat{g}_i \leq u_i, \quad i = 1, \ldots, mN. \end{aligned}$$

The key idea is to subdivide the time indices according to active constraint sets for the control function at the kth iteration, which is denoted by $\hat{g}^k$. Let $\mathcal{L}$ and $\mathcal{U}$ denote the sets of indices of $\hat{g}^k$ for which the lower and upper bounds are active. That is, if $\hat{g}_i^k = l_i$ then $i \in \mathcal{L}$, and if $\hat{g}_i^k = u_i$ then $i \in \mathcal{U}$. In addition, let $\mathcal{F}$ contain indices where inequality constraints are inactive, i.e., if $l_i < \hat{g}_i^k < u_i$ then $i \in \mathcal{F}$. Along the same lines, let us denote $\hat{g}_{\mathcal{F}}^k = \{\hat{g}_i^k \mid i \in \mathcal{F}\}$, $l_{\mathcal{L}} = \{l_i \mid i \in \mathcal{L}\}$, $u_{\mathcal{U}} = \{u_i \mid i \in \mathcal{U}\}$ and let the matrices $W_{\mathcal{F}} \in \mathbb{R}^{nP \times |\mathcal{F}|}$, $W_{\mathcal{L}} \in \mathbb{R}^{nP \times |\mathcal{L}|}$, and $W_{\mathcal{U}} \in \mathbb{R}^{nP \times |\mathcal{U}|}$ contain the columns of W corresponding to the indices of $\mathcal{F}$, $\mathcal{L}$, and $\mathcal{U}$, respectively. The iteration is initialized with all indices in $\mathcal{F}$, then the unconstrained minimum-norm control $\hat{g}^0$ is found, and the iteration continues in three alternating stages. First, any values of $\hat{g}^k$ that violate the inequality constraints are set to the extremal permitted value. Second, the KKT conditions are checked, and any elements of $\hat{g}^k$ in the active constraint sets $\mathcal{L}$ or $\mathcal{U}$ that do not satisfy the gradient conditions for a given tolerance of $\varepsilon_\nabla > 0$ are returned to the free set $\mathcal{U}$. Finally, $\hat{g}^{k+1}$ is found by applying the SVD-based method of Section 2.2 by solving for $\hat{g}_{\mathcal{F}}^{k+1}$ where $W_{\mathcal{F}}\hat{g}_{\mathcal{F}}^{k+1} = \xi_{\mathcal{F}}$, where $\xi_{\mathcal{F}} = \xi - W_{\mathcal{L}} l_{\mathcal{L}} - W_{cU} u_{\mathcal{U}}$, and appropriately concatenating $l_{\mathcal{L}}$ and $u_{\mathcal{U}}$.

Algorithm 1: Constrained minimum-norm ensemble control synthesis.

1. Set $\mathcal{F} = \{1, \ldots, mN\}$, and obtain $\hat{g}^0 = W^\dagger \xi$ using method in Section 2.2

2. $\forall\, i \in \mathcal{F}$: If $\hat{g}_i^k \geq u_i$, set $\hat{g}_i^{k+1} = u_i$ and $i \in \mathcal{U}$. If $\hat{g}_i^k \leq l_i$, set $\hat{g}_i^{k+1} = l_i$ and $i \in \mathcal{L}$.

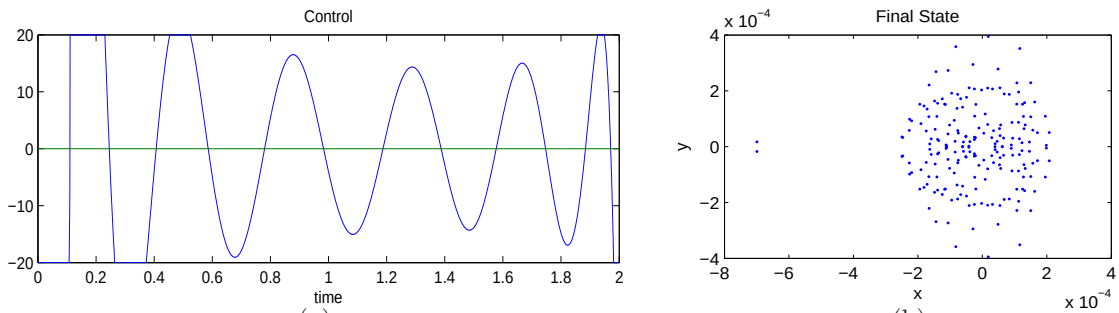

(a) (b)

Figure 2.6: Simulation of system ensemble (2.12) for $N = 3000$, $T = 2$, $P = 100$, and $\omega \in [-10, 10]$. The initial and target states are $X_0(\omega) = (1, 0)'$ and $X_F(\omega) = (0, 0)'$. (a) The optimal control law $(u(t), v(t))$ computed using Algorithm 1 using lower and upper bounds of $l_i = -20$ and $u_i = 20$, respectively. A relative truncation threshold of $\tau_r = 10^4$ is used to synthesize the control at the free indices at each step. (b) Terminal states of the ensemble when the control is applied. The mean terminal error is 1.68×10^{-4}.

3. Check KKT gradient conditions: Let $G = \nabla \mathcal{J}[\hat{g}^k] = W'(\xi - W\hat{g}^k)$. $\forall\, i \in \mathcal{F}$: If $G_i \geq \varepsilon_\nabla$ for $i \in \mathcal{L}$ or $G_i \leq -\varepsilon_\nabla$ for $i \in \mathcal{U}$, set $i \in \mathcal{F}$.

4. Find $\hat{g}^{k+1}_{\mathcal{F}} = W^\dagger_{\mathcal{F}} \xi_{\mathcal{F}}$ by SVD method for $W_{\mathcal{F}}$ and $\xi_{\mathcal{F}} = \xi - W_{\mathcal{L}} l_{\mathcal{L}} - W_{\mathcal{U}} u_{\mathcal{U}}$. Reassemble $\hat{g}^{k+1}$ using $\hat{g}^{k+1}_{\mathcal{F}}$, $\hat{g}^{k+1}_{\mathcal{L}} = l_{\mathcal{L}}$, and $\hat{g}^{k+1}_{\mathcal{U}} = u_{\mathcal{U}}$. Go to 2

The Algorithm 1 was applied to the ensemble of harmonic oscillators of the form 2.12 using upper and lower bounds of $l_i = -20$ and $u_i = 20$, and the results are shown in Figure 2.6. For the discretization parameters $N = 3000$ and $P = 100$ and the time horizon $T = 2$, the algorithm terminated after $k = 48$ iterations.

2.5 Convergence Analysis and Open Problems

Finally, this chapter is concluded with a discussion of convergence issues and related open problems for the numerical ensemble control synthesis method for linear systems described in Section 2.2. The idea of approximating an integral operator using a quadrature approximation is referred to as the Nystr om method [169]. A great deal of literature has been devoted to characterize the consistency, stability, convergence, and regularity of numerical solutions to Fredhom equations of the first kind [11, 12, 89, 181]. In addition, the SVD of approximating matrix operators has been previously used to compute singular systems for Fredholm integral equations [223, 92, 91, 11], although the applications have been primarily in the context of least-squares problems, rather than minimum norm solutions. The

implications for system identification and control have been examined in at least one study [72].

For a Fredholm integral equation of the first kind with a continuous, Hermitian kernel $k(x, y)$, consider a family of quadrature rules $\{J_N\}$ with positive weights such that $\lim_{N\to\infty} J_N(\phi) = \int_a^b \phi(y)\mathrm{d}y$ for every function $\phi \in C[a, b]$, which is used to produce a family of square matrices $\hat{K}_N$ that approximate the integral operator $(K\phi)(y) = \int_a^b k(x, y)\phi(x)dx$ (using N samples of both variables x and y). It is well established (see Theorems 3.4 and 3.5 in [11]) that as $N \to \infty$, the eigenvalues and eigenvectors of $\hat{K}_N$ converge to the eigenvalues and eigenfunctions of the operator K. Observe that WW' and $W'W$ approximate LL^* and L^*L, respectively. Furthermore, the eigenvalues of LL^* and L^*L are squares of the singular values of L. This suggests a natural direction to explore the properties of the SVD-based method in Section 2.2, and possibly to obtain constructive controllability criteria for ensemble systems of more explicit form than 2.7.

The theoretical treatment in previous work provides a foundation for examining ensemble controllability [139], but a straightforward test for this property is not yet available. While it is possible to test for ensemble controllability in certain cases by using Lie algebras [142, 184], the complexity of the systems encountered in many applications makes this problematic in general. It is important to explore the relationship between ensemble controllability, the Picard criterion, and the singular values of the integral operator (2.5) and its matrix analogue W. Investigation in this direction may lead to an implementable numerical controllability test for general ensemble systems. In addition, a thorough numerical analysis is required to better understand the accuracy and conditioning properties of this approach, in order to predict its performance under various circumstances, and to determine whether a computational test for ensemble controllability is indeed feasible.

Chapter 3

Control of Bilinear Ensemble Systems

The challenge of controlling continuously indexed system ensembles was originally motivated by practical factors that arise in nuclear magnetic resonance (NMR) spectroscopy and imaging (MRI) as well as the broader field of quantum control, and has given rise to a new area of mathematical control theory called ensemble control [137]. These rapidly progressing technologies require the manipulation of very large ensembles of quantum systems, e.g., on the order of Avogodro's number (6×10^{23}), whose states cannot be measured during the transfer, and whose dynamics are subject to dispersion in parameters such as frequency. The performance of the necessary controls must be insensitive to parameter variation across the ensemble, as well as to inhomogeneity in the applied radiofrequency (RF) control field [142, 140, 38]. Furthermore, the techniques developed for ensemble control can be applied to robust sensorless manipulation, which is of interest in machining and manipulation tasks where feedback is unavailable and the performance must be immune to uncertainty in model parameters [17]. Such problems are largely neglected in the literature on robust control, which is oriented on the use of feedback [123, 222, 132].

The examination of ensemble control of bilinear systems begins with the notion of ensemble controllability, which determines the existence of controls that achieve state transfers of interest. It has been shown that a bilinear system evolving on SO(3) called the Bloch system, which represents the transition over time of the bulk magnetization of a sample of nuclear spins, is ensemble controllable [137, 140]. More fundamentally, the necessary and sufficient conditions for ensemble controllability of finite-dimensional time-varying linear systems have been derived [138], as described in the previous chapter, and extended to stochastic systems [185]. These conditions depend on the singular system of the operator that characterizes the system dynamics, which can in turn be used to represent the minimum

norm control that accomplishes the transfer as an infinite sum of weighted eigenfunctions [139]. The controllability conditions for general nonlinear ensemble control problems are unknown, and analytical control design methods remain a challenging problem, although analytical solutions exist for a few specific systems [16].

This chapter is devoted to developing constructive numerical methods for synthesizing optimal ensemble controls, rather than to focus on issues of controllability. A recent optimization-based approach is a pseudospectral method that translates an optimal control problem in function space into a finite discrete nonlinear programming problem [143, 191, 144]. This method has been effective for a variety of ensemble control problems, but relies heavily on nonlinear programming techniques due to its inherent computational complexity [192]. Therefore, a need exists for optimization-free, stable, and computationally efficient numerical methods for synthesizing ensemble controls that can accomplish diverse state transfers for a variety of systems. The previous chapter contains a description of a method based on the SVD to constructs minimum norm ensemble controls for finite-dimensional time-varying linear systems [239], as well as stochastic linear systems [185]. In this approach the singular system of the Fredholm integral operator of the first kind that characterizes the dynamics of a linear ensemble system is approximated using the SVD, and the optimal control is approximated as a weighted sum of singular vectors.

Although the former approach is effective for linear ensemble systems, the most compelling practical ensemble control problems in quantum control and robotics involve systems of bilinear form. A natural approach to such problems is to apply methods for linear systems iteratively to linearized bilinear systems to produce a scheme for successive approximations. Such techniques exist for feedback control design for finite-time, free endpoint problems with quadratic cost functionals and bilinear dynamic constraints, and are based on iterative solution of Riccati-type equations [100, 2]. In contrast, we are interested in designing open-loop control solutions to fixed-endpoint problems for bilinear systems such that the control performance is insensitive to system parameter variation, which requires a novel approach.

The subsequent sections describe an iterative fixed-point method for directly synthesizing ensemble controls for bilinear systems [237]. At each step of the iteration, the bilinear ensemble system is approximated by a time-varying linear ensemble system, and the SVD-based method in Section 2.2 is used to synthesize the control used to generate the state trajectory estimate, about which the system is linearized in the following iteration. The

same approach can be adapted to accommodate constraints on the control amplitude by using the method in Section 2.4 as well.

3.1 Ensemble Control Synthesis for Bilnear Systems

Many important problems in control engineering with applications to robotics, medicine, and other fields require the manipulation of bilinear systems [143, 197, 30, 38, 158]. We focus here on time-invariant systems because our approach is easily generalized to the non-autonomous case. Consider the system

$$\dot{X} = A(\beta)X + \left[\sum_{i=1}^{m} u_i(t)B_i(\beta)X\right] + B_0(\beta)u(t), \tag{3.1}$$
$$X \in M \subset \mathbb{R}^n, \quad \beta \in K \subset \mathbb{R}, \quad u \in U \subset \mathbb{R}^m,$$

where $u = (u_1, \ldots, u_m)'$, $X = X(t, \beta)$, $A(\beta) \in \mathbb{R}^{n\times n}$ has elements that are real L_∞ functions defined on a compact set K, and $B_1(\beta), \ldots, B_m(\beta) \in \mathbb{R}^{n\times n}$ and $B_0(\beta) \in \mathbb{R}^{n\times m}$ have elements that are real L_2 functions also defined on K. We denote $A \in L_\infty^{n\times n}(K)$, $B_1, \ldots, B_m \in L_2^{n\times n}(K)$, and $B_0 \in L_2^{n\times m}(K)$. Ensemble controllability for the system (3.1) follows Definition 1. This system can be rewritten as

$$\dot{X} = A(\beta)X + \left[\sum_{j=1}^{n} x_j \widetilde{B}_j(\beta) + B_0(\beta)\right]u(t), \tag{3.2}$$

where $X = (x_1, \ldots, x_n)'$ and $\widetilde{B}_1, \ldots, \widetilde{B}_n \in L_2^{n\times m}(K)$. Hence the one-step ensemble control synthesis scheme for linear systems described in Section 2.2 can be extended to produce an iterative fixed-point method that constructs ensemble controls for bilinear systems by replacing at each iteration the autonomous inhomogeneous component with a time-varying homogeneous approximation involving the output of the previous step. Suppose that the ensemble (3.2) is controllable and is to be guided from $X(0, \beta) = X_0(\beta)$ to $X(T, \beta) = X_F(\beta)$. Given an estimate (X^α, u^α) of the trajectory-control pair where $X^\alpha = (x_1^\alpha, \ldots, x_n^\alpha)'$, $u^\alpha = (u_1^\alpha, \ldots, u_m^\alpha)'$ and α is an iteration index, substituting $x_j(t, \beta) = x_j^\alpha(t, \beta)$ for $j = 1, \ldots, n$ in

(3.2) yields the time-varying linear system

$$\dot{X}(t,\beta) = A(\beta)X(t,\beta) + B^{\alpha}(t,\beta)u(t), \tag{3.3}$$

where

$$B^{\alpha}(t,\beta) = \sum_{j=1}^{n} x_j^{\alpha}(t,\beta)\widetilde{B}_j(\beta) + B_0(\beta). \tag{3.4}$$

The SVD-based method in Section 2.2 is used to synthesize a control $u^{\alpha+1}$ that solves the integral operator equation

$$(L^{\alpha}u)(\beta) = \int_0^T \Phi(0,\sigma,\beta)B^{\alpha}(\sigma,\beta)u(\sigma)d\sigma = \xi(\beta), \tag{3.5}$$

where $\xi(\beta) = \Phi(0,T,\beta)X_F(\beta) - X_0(\beta)$ characterizes the desired state transfer for the linearized system (3.3). This control is applied to (3.2) with $X(0,\beta) = X_0(\beta)$ to produce a new trajectory $X^{\alpha+1}$, and the next iterate $(X^{\alpha+1}, u^{\alpha+1})$, and the process is repeated until $E(\alpha) := \|u^{\alpha+1} - u^{\alpha}\|/\|u^{\alpha}\| < \gamma$ where γ is a relative error tolerance.

In order to avoid the accumulation of numerical errors that cause the iteration to diverge, the entire procedure must be conducted using the discretization scheme (2.10) in Section 2.2. Specifically, we define the vector $\hat{\xi} \in \mathbb{R}^{nP}$ with $n \times 1$ blocks $\hat{\xi}_j = \xi(\beta_j)$ that characterizes the desired state transfer. At the next iteration, a vector $\hat{u}^{\alpha+1} \in \mathbb{R}^{mN}$ with $m \times 1$ blocks $\hat{u}_k^{\alpha+1} = u(t_k)$ constitutes a discretization of the control. The action of L^{α} on a function $g \in \mathcal{H}_T$ is approximated by the action of a block matrix $W^{\alpha} \in \mathbb{R}^{nP\times mN}$, wih $n \times m$ blocks $W_{jk}^{\alpha} = \delta\Phi(0,t_k,\beta_j)B^{\alpha}(t_k,\beta_j)$, on a vector $\hat{g} \in \mathbb{R}^{mN}$, with N blocks $\hat{g}_k = g(t_k)$ of dimension $m \times 1$. Following the steps in Section 2.2, the minimum norm solution $\hat{u}^{\alpha+1}$ that satisfies $W^{\alpha}\hat{u}^{\alpha+1} = \hat{\xi}$ is given by

$$\hat{u}^{\alpha+1} = \sum_{j=1}^{mq} \frac{\hat{\xi}'\bar{u}_j}{s_j}\bar{v}_j \tag{3.6}$$

where $(s_j, \bar{v}_j, \bar{u}_j)$ is the SVD of W^{α}. We then require that the discrete approximation $\hat{X}^{\alpha+1}$ of $X^{\alpha+1}$ is made on the same grid $\{\beta_j\} \times \{t_k\}$ that is used to synthesize W^{α} as the discrete approximation of L^{α}. In particular, we define the quadrature approximation

$\hat{X}_{jk}^{\alpha+1} \approx X^{\alpha+1}(t_k, \beta_j)$ by

$$X_{jk}^{\alpha+1} = \Phi(t_k, 0, \beta_j)[X_0(\beta_j) + \mathcal{W}_{jk}^{\alpha}\mathcal{U}_k^{\alpha}] \tag{3.7}$$

where

$$\mathcal{W}_{jk}^{\alpha} = \begin{bmatrix} W_{j1}^{\alpha} & W_{j2}^{\alpha} & \dots & W_{jk}^{\alpha} \end{bmatrix} \in \mathbb{R}^{nP \times mk},$$

$$\mathcal{U}_k^{\alpha} = \begin{bmatrix} (\hat{u}_1^{\alpha})' & (\hat{u}_2^{\alpha})' & \dots & (\hat{u}_k^{\alpha})' \end{bmatrix}' \in \mathbb{R}^{mk \times 1}.$$

If a control $u^* = (u_1^*, \dots, u_m^*)'$ exists that accomplishes this transfer via the trajectory $X^* = (x_1^*, \dots, x_n^*)'$, it follows that u^* is a solution to the integral operator (2.5) with

$$B(t, \beta) = \sum_{j=1}^{n} x_j^*(t, \beta)\widetilde{B}_j(\beta) + B_0(\beta). \tag{3.8}$$

In certain cases, the successive approximations $(\hat{X}^{\alpha}, \hat{u}^{\alpha})$ converge to a fixed point $(\hat{X}^*, \hat{u}^*)$, which approximates a trajectory-control pair (X^*, u^*) that accomplishes the desired transfer. When $B_i \equiv 0$ for $i = 1, \dots, m$, the system (3.2) is linear in X and the iteration terminates after a single step. In the following section, several example implementations of the above technique are described, with a particular focus on the Bloch system.

3.2 Examples of Bilinear Ensemble Systems

In this section, several examples of ensemble control synthesis for bilinear systems are examined, beginning with the Bloch system, which is ubiquitous in quantum control applications.

3.2.1 The Bloch System

The canonical example of a bilinear control system of particular interest is the Bloch system [30], which describes the evolution of the bulk magnetization of a sample of nuclear spins

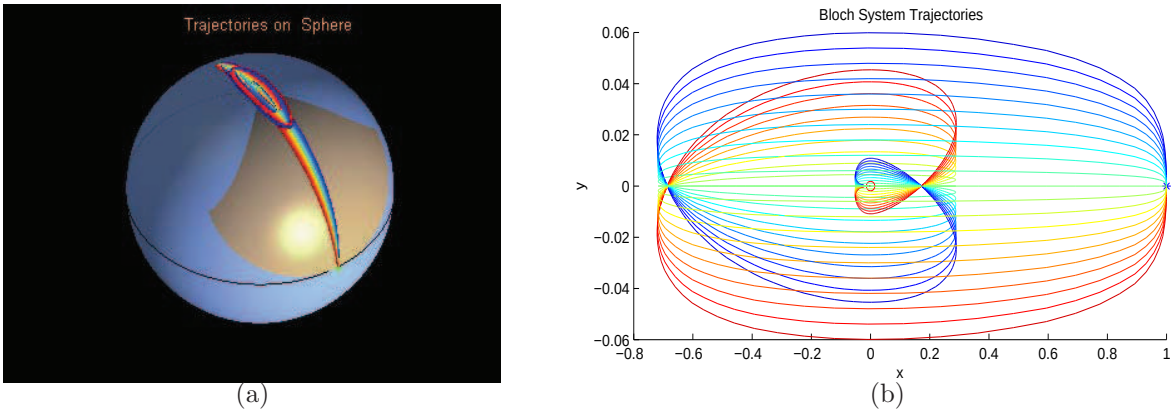

(a) (b)

Figure 3.1: (a) Bloch system trajectories sampled from $\omega \in [-8, 8]$. Trajectories for a control generated for $\omega \in [-5, 5]$, $N = 5000$, and $P = 20$ for a 90° transfer in $T = 1$ (gray lines), and for a control generated for the same transfer of a nominal system with $\omega = 0$ (black lines). (b) Bloch system trajectories sampled from $\omega \in [-1, 1]$, with applied control generated using $N = 2000$ and $P = 20$, viewed from positive z-axis.

immersed in a magnetic field, and which is given by

$$\dot{X} = \begin{bmatrix} 0 & -\omega & \varepsilon u_1 \\ \omega & 0 & -\varepsilon u_2 \\ -\varepsilon u_1 & \varepsilon u_2 & 0 \end{bmatrix} X, \tag{3.9}$$

where $X = (x_1, x_2, x_3)'$ is a unit vector in $\mathbb{R}^3$, $u = (u_1, u_2)'$ is a vector of control parameters, and $\omega \in [-\mu, \mu]$ and $\epsilon \in [1 - \delta, 1 + \delta]$ represent dispersion in Larmor frequency and radio frequency (RF) inhomogeneity, respectively, for $\mu > 0$ and $\delta \in (0, 1)$. This system can be re-written as

$$\dot{X} = \begin{bmatrix} 0 & -\omega & 0 \\ \omega & 0 & 0 \\ 0 & 0 & 0 \end{bmatrix} X + \varepsilon \begin{bmatrix} x_3 & 0 \\ 0 & -x_3 \\ -x_1 & x_2 \end{bmatrix} u. \tag{3.10}$$

It is a well established result that the Bloch system is ensemble controllable with respect to both ω and ε [137, 142, 140, 124]. However, when formulated as in (3.3), the system (3.10) is of the form $\dot{X} = A(\omega)X + \varepsilon B^{\alpha}(t, \omega)u$, and applying the variation of parameters formula makes it clear that it is not ensemble controllable with respect to ε. This can also be shown using a Lie algebraic argument ([139], Example 1). This observation highlights a significant limitation of our method, namely, that the linearization of the bilinear system must be ensemble controllable with respect to all uncertain parameters. We will let $\varepsilon \equiv 1$ be

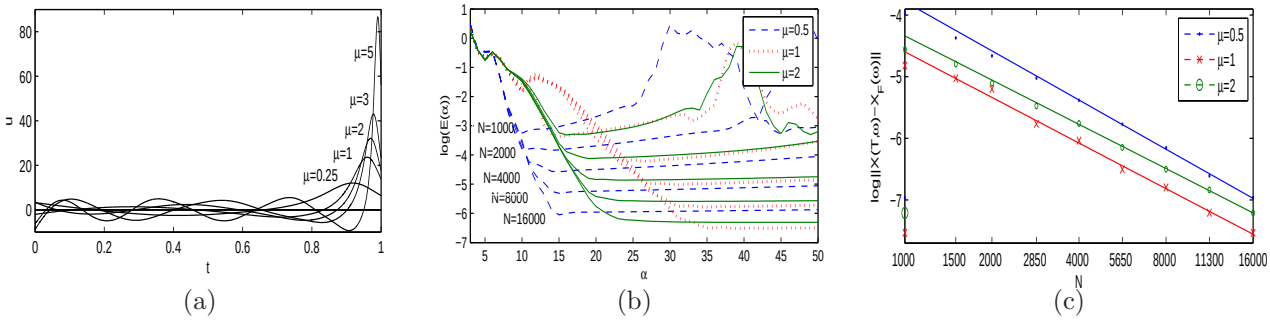

Figure 3.2: (a) Ensemble controls u for the Bloch system with several values of μ generated using $N = 5000$, $P = 20$, $T = 1$ for a 90° transfer in $T = 1$. (b) Log plot of relative change $E(\alpha)$ between successive control iterates and (c) Log-log plot of terminal error as a function of discretization N for $\mu = 0.5$, 1, and 2. Note that the terminal error is smallest for $\mu = 1$.

a constant, and apply the technique to successfully compensate for variation in the parameter ω to produce a broadband excitation pulse.

We now examine the synthesis of an ensemble control that accomplishes a 90° ($\pi/2$) transfer of the state from $X_0(\beta) = (0, 0, 1)'$ to $X_F(\beta) = (1, 0, 0)'$ for the Bloch system, which is a canonical step in NMR. The time interval chosen is $T = 1$. Figure 3.1 compares trajectories sampled from the ensemble with $\mu = 8$, which are produced when the ensemble control constructed for $\mu = 5$ is applied, with those produced when the optimal control for the nominal system with $\omega = 0$ is applied. It is noteworthy that the control performance for this broadband compensation pulse exceeds the specification. Figure 3.2 displays ensemble controls for several values of μ, which achieve various broadband excitation profiles. In each case the transfer is accomplished with $v \equiv 0$, using only the control u. A plot of the relative change in successive control iterates u^α and a log-log plot of the terminal error as a function of discretization N are shown for several values of μ as well. These numerical convergence results indicate that the method is accurate and consistent for this example.

In addition to a $\pi/2$ transfer, the method can rapidly synthesize control inputs that can induce a uniform ensemble transfer between arbitrary points on the Bloch sphere, as well as a nonuniform transfer. Figure 3.3 shows the ensemble controls and resulting trajectories for transfers between arbitrary points on the Bloch sphere, and a non-uniform transfer of the ensemble.

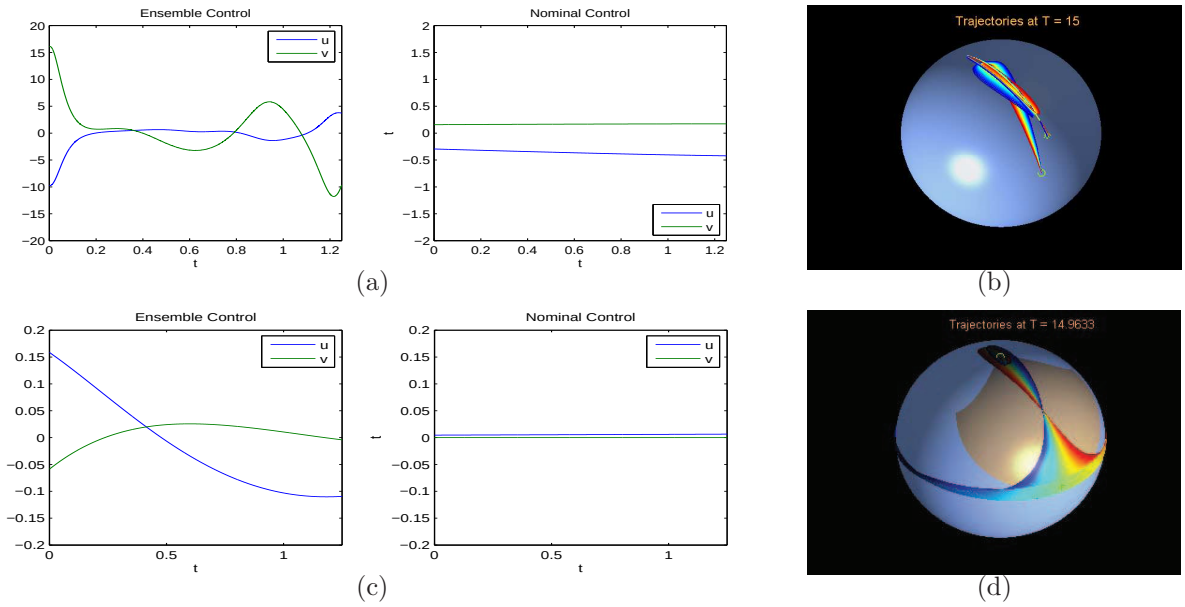

Figure 3.3: (a) Ensemble controls u for the Bloch system with dispersion $\omega \in [-2, 2]$, $\varepsilon \equiv 1$, to be steered from $X_0 = (.44, .8, .42)'$ to $X_F = (.16, .67, .72)'$ in $T = 1.25$, generated using $N = 4000$ and $P = 20$. (b) Resulting trajectories. (c) Ensemble controls u for dispersion $\omega \in [-.5, .5]$, $\varepsilon \equiv 1$, to be steered from $X_0 = (0, 0, 1)'$ to $X_F = (\cos(\pi\omega), \sin(\pi\omega), 0)'$ in $T = 15$, generated using $N = 20000$ and $P = 100$.

3.2.2 Coupled Bloch Systems

The method in Section 3.1 is also effective for controlling time-varying systems with multiple uncertain parameters. Consider an ensemble consisting of pairs of Bloch systems with time-varying coupling, with system dynamics given by

$$\dot{X} = \begin{bmatrix} 0 & -\xi & u_1 & 0 & -\rho t & 0 \\ \xi & 0 & -u_2 & \rho t & 0 & 0 \\ -u_1 & u_2 & 0 & 0 & 0 & 0 \\ 0 & \rho(1-t) & 0 & 0 & -\lambda & u_1 \\ -\rho(1-t) & 0 & 0 & \lambda & 0 & -u_2 \\ 0 & 0 & 0 & -u_1 & u_2 & 0 \end{bmatrix} X \tag{3.11}$$

where $X = (x_1, x_2, x_3, x_4, x_5, x_6)'$, and $u = (u_1, u_2)'$ is a vector of control parameters. Given initial and target states $X_0(\beta) = (0, 0, 1, 0, 0, 1)'$ and $X_F(\beta) = (1, 0, 0, 1, 0, 0)'$ and a time horizon $T = 1$ and discretization $N = 5000$, we find an ensemble control for interaction parameter $\rho = 0.1$ and frequency dispersions $\xi \in [-0.2, 0.2]$ and $\lambda \in [0.8, 1.2]$ using $P = 25$

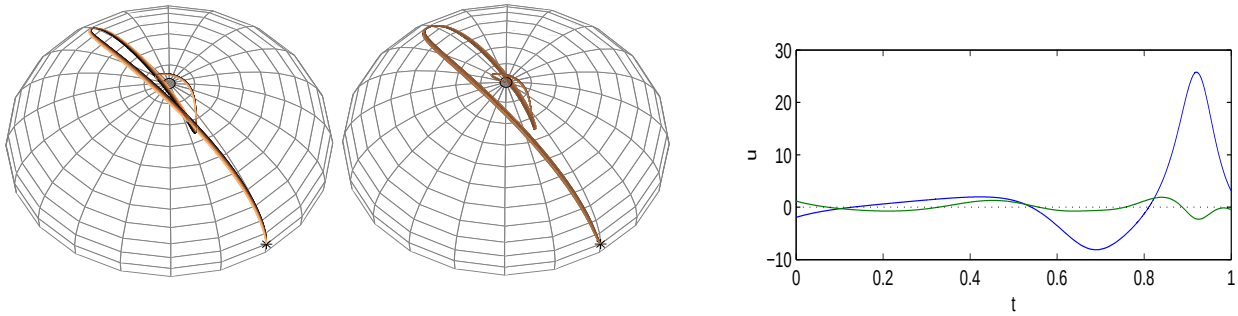

(a) (b)

Figure 3.4: (a) Controlled trajectories of the ensemble of Bloch system pairs (3.11) on $SO(3) \times SO(3)$ with $X_0(\beta) = (0, 0, 1, 0, 0, 1)'$ and $X_F(\beta) = (1, 0, 0, 1, 0, 0)'$; (b) Iteratively computed control for a time horizon $T = 1$, discretization $N = 5000$, interaction parameter $\rho = 0.1$, frequency dispersions $\xi \in [-0.2, 0.2]$ and $\lambda \in [0.8, 1.2]$, and $P = 25$ samples

samples. The resulting trajectories on $SO(3) \times SO(3)$, the ensemble control, and the log of the relative change $E(\alpha)$ between successive control iterates is shown in Figure 3.4.

3.3 Discussion of Convergence and Open Problems

Several limitations to our approach suggest compelling theoretical research directions. First, the necessary and sufficient conditions for controllability of general ensemble systems remains an open problem, and therefore it cannot always be determined a priori for which bilinear systems and state transfers in the space $\mathcal{H}_K$ ensemble controls exist. In addition, the convergence properties of the fixed-point iteration described in Section 3.1 are complex, and problematic to characterize. In this section, we formulate the iterative control synthesis technique for bilinear systems described in Section 3.1 as a nonlinear operator, and discuss its properties.

Consider a controllable finite-dimensional bilinear system of the form

$$\dot{X}(t) = \left[A(t) + \sum_{i=1}^{m} u_i(t) H_i(t) \right] X(t) \tag{3.12}$$

where $X(t) \in \mathbb{R}^n$ is the system state, $U(t) \in \mathbb{R}^m$ is a control input with components u_i. In addition, we require that $A(t) \in \mathbb{R}^{n \times n}$ and $H_i(t) \in \mathbb{R}^{n \times n}$ have elements that are real L_∞ and Ł_2 functions, respectively. Suppose that we wish to steer (3.12) from an initial state

$X(0) = X_0$ to a desired final state $X(T) = X_F$. Towards this aim, we can formulate a fixed point iteration whose fixed point accomplishes the desired state transfer.

The first step is to construct matrices $B_j \in \mathbb{R}^{n\times m}$ such that (3.12) can be rewritten in the form

$$\dot{X}(t) = A(t)X(t) + \left[\sum_{j=1}^{n} x_j(t)B_j(t)\right]U(t). \tag{3.13}$$

The trajectories of the system (3.13) lie in $\mathcal{H}_S = L_2^n[0,T]$, the set of real n-vector-valued square-integrable functions on $[0,T]$, for which we define an inner product for $X, Y \in \mathcal{H}_S$ by

$$\langle X, Y\rangle_S = \int_0^T X'(t)Y(t)\mathrm{d}t. \tag{3.14}$$

With well-defined addition and scalar multiplication, $\mathcal{H}_S$ is a separable Hilbert space, where $||\cdot||_S$ denotes the induced norm, and d_S denotes the induced metric, which is defined by

$$d_S(X,Y) = ||X-Y||_S = \left(\int_0^T ||X-Y||_2^2\mathrm{d}t\right)^{1/2}. \tag{3.15}$$

As a result of the Riesz-Fischer theorem [15], $\mathcal{H}_S$ is a complete metric space. For any nominal trajectory $Y(t) \in \mathcal{H}_S$ with components $y_j(t)$, one can define $B(Y(t)) = \sum_{j=1}^{n} y_j(t)B_j(t)$ to create a time-varying linear system of the form

$$\dot{X}(t) = A(t)X(t) + B(Y(t))U(t). \tag{3.16}$$

It is well-established [25] that the minimum norm control $U^*(t)$ that steers (3.16) from $X(0) = X_0$ to $X(T) = X_F$ is given by

$$U(t) = B'(Y(t))\Phi'(0,t)[W_Y(0,T)]^{-1}\xi, \tag{3.17}$$

where $\Phi(t,0)$ is the transition matrix for the homogeneous system $\dot{X}(t) = A(t)X(t)$, where $\xi = \Phi(0,T)X_F - X_0$, and where

$$W_Y(t_0,t_1) = \int_{t_0}^{t_1} \Phi(t_0,\sigma)B(Y(\sigma))B'(Y(\sigma))\Phi'(t_0,\sigma)\mathrm{d}\sigma \tag{3.18}$$

is the controllability Gramian of (3.16). Then an iteration similar to that described in Section 3.1 is formulated as follows. Substituting an initial nominal trajectory $Y_0(t)$ into (3.17) results in the minimum norm input $U_0 = B'(Y_0(t))\Phi'(0,t)[W_{Y_0}(0,T)]^{-1}\xi$. Applying U_0 to (3.16) and using the variation of parameters formula yields

$$\begin{aligned} X(t) &= \Phi(t,0)\Big(X_0 + \int_0^t \Phi(0,\sigma)B(Y_0(\sigma))U_0^*(\sigma)\mathrm{d}\sigma\Big) \\ &= \Phi(t,0)\Big(X_0 + \int_0^t \Phi(0,\sigma)B(Y_0(\sigma))B'(Y_0(t))\Phi'(0,t)[W_{Y_0}(0,T)]^{-1}\xi\mathrm{d}\sigma\Big) \\ &= \Phi(t,0)\big(X_0 + W_{Y_0}(0,t)[W_{Y_0}(0,T)]^{-1}\xi\big). \end{aligned} \tag{3.19}$$

The next trajectory iterate is obtained from (3.19), and is given by $Y_1(t) = \Phi(t,0)(X_0 + W_{Y_0}(0,t)[W_{Y_0}(0,T)]^{-1}\xi)$. Successively generating the control (3.17) and trajectory (3.19) results in a fixed point iteration $Y_{k+1}(t) = \mathcal{T}[Y_k](t)$ for the trajectory, where $\mathcal{T} : \mathcal{H}_S \to \mathcal{H}_S$ is an operator defined by

$$\mathcal{T}[Y](t) = \Phi(t,0)(X_0 + W_Y(0,t)[W_Y(0,T)]^{-1}\xi). \tag{3.20}$$

We are interested in the conditions under which the sequence Y_k converges to the trajectory Y^* that corresponds to the minimum norm input U^*, which transfers (3.12) from $X(0) = X_0$ to $X(T) = X_F$. For two distinct trajectories $X_1, X_2 \in \mathcal{H}_S$, we can write

$$T[X_1](t) - T[X_2](t) = \Phi(t,0)(W_{X_1}(0,t)[W_{X_1}(0,T)]^{-1} - W_{X_2}(0,t)[W_{X_2}(0,T)]^{-1})\xi, \tag{3.21}$$

so that

$$||T[X_1](t) - T[X_2](t)||_2 \leq ||\xi||_2 \cdot ||\Phi(t,0)||_2 \cdot ||K(X_1, X_2, t)||_2, \tag{3.22}$$

where we define

$$K(X_1, X_2, t) = W_{X_1}(0,t)[W_{X_1}(0,T)]^{-1} - W_{X_2}(0,t)[W_{X_2}(0,T)]^{-1}, \tag{3.23}$$

and where $||A||_2 \triangleq \sup_{||x||_2=1} ||Ax||_2$ denotes the matrix 2-norm. Observe that the matrix K satisfies $||K(X,Y,t)||_2 = ||K(aX,bY,t)||_2$ for any $a \neq 0$ and $b \neq 0$. As a result, the convergence properties of the fixed-point operator 3.20 will be independent of the magnitude of of trajectories, but rather will depend on their location on the unit n-ball. Consequently,

this approach is especially well suited for bilinear systems with unitary evolution, such as the Bloch system (3.9), for which the dynamics (3.12) will satisfy $A(t) = -A'(t)$ and $H_i(t) = -H_i'(t)$. Furthermore, note that the technique for ensemble control synthesis for bilinear systems that is formulated in Section 3.1 is a discretized application of the iteration (3.20), where the minimum norm input (3.17) is replaced with the SVD-based method of Section 2.2. Nevertheless, the convergence properties of this approach remain a challenging open problem. Finally, note that iterative techniques exist for feedback control design for finite-time, free endpoint problems with quadratic cost functionals and bilinear dynamic constraints [2]. The local convergence of this approach has been demonstrated [100], but because these techniques are based on iterative solution to Riccati-type equations, the convergence is highly sensitive to the initial guess, and is not scalable beyond low-dimensional systems due to numerical conditioning issues.

3.4 Bloch System with Constrained Control Amplitude

The iterative control synthesis approach in Section 3.1 can be modified to accommodate constraints on the control amplitude by substituting the minimum-norm synthesis step that uses the method in Section 2.2 with the constrained minimum-norm synthesis method described in Section 2.4. The resulting nested iteration technique yields constrained ensemble controls for bilinear systems, as shown in Figure 3.5 for the Bloch system example of Section 3.2.1. Due to the additional constraints, the iteration may be less stable, so that a regularizing modification can prevent cycling of the solution and expedite convergence. Specifically, Mann's iteration method [150] can be used to produce a recursion of the form

$$\hat{X}^{\alpha+1} = (1 - c_n)\hat{X}^{\alpha} + c_n \hat{\mathcal{T}}[\hat{X}^{\alpha}](t), \tag{3.24}$$

where $c_n \in (0, 1)$ and $\hat{\mathcal{T}}$ denotes one step of the iterative method in Section 3.1. Mann's algorithm was shown to converge weakly to fixed points of nonexpansive mappings if $\sum_{n=0}^{\infty} c_n(1-c_n) = \infty$ holds [229]. Employing Mann's algorithm effectively slows changes between successive iterations of the method of Section 3.1 that may arise from the addition of constraints. In the implementation used here, the coefficients c_n are chosen adaptively to prevent dramatic changes between iterations, while also avoiding stalling.

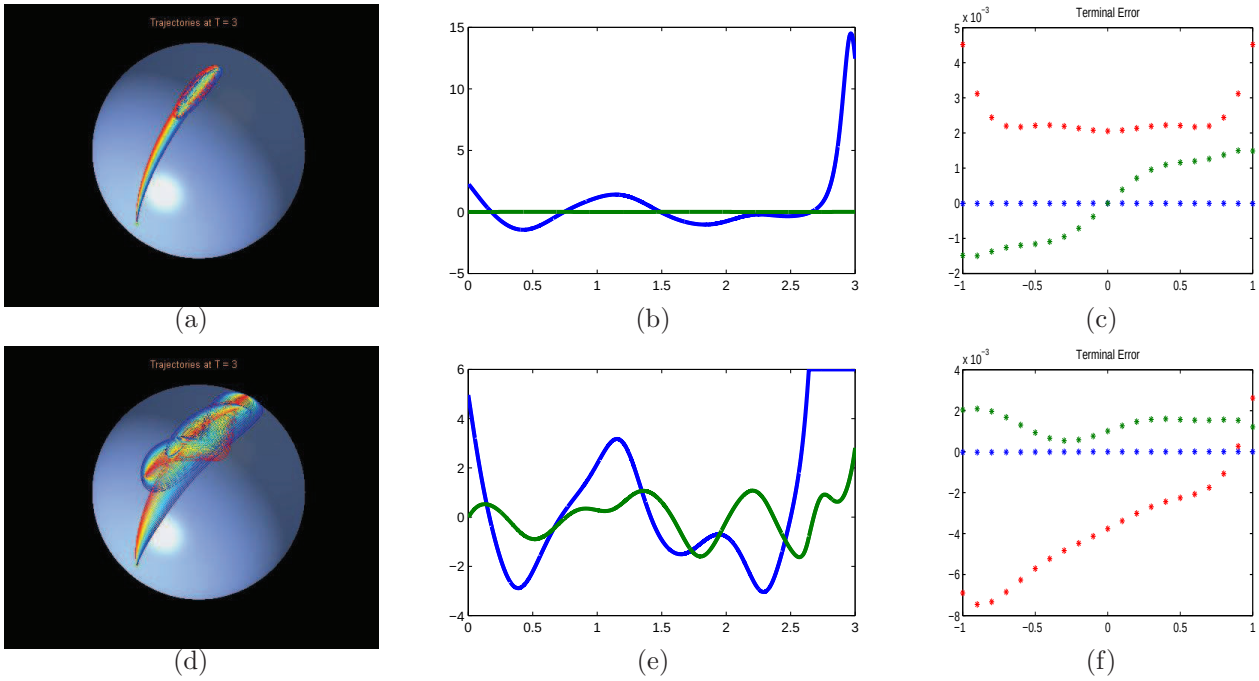

Figure 3.5: Ensemble controls u for the Bloch system with $\omega \in [-1, 1]$, $\varepsilon \equiv 1$, to be steered from $X_0 = (0, 0, 1)'$ to $X_F = (1, 0, 0)'$ in $T = 3$, generated using $N = 20000$ and $P = 20$. (a) Trajectories obtained by applying (b) the unconstrained ensemble control with $||u||_T = 4.604$ found after 29 iterations of the method in Section 3.1, with (c) terminal error on the order of 10^{-3}. (d) Trajectories with (e) the control constrained at $|u| \leq 6$, which is obtained after 86 iterations of the method in Section 3.4 and has $||u||_T = 5.016$, with (f) terminal error also on the order of 10^{-3}.

Chapter 4

Phase Models for Nonlinear Oscillators

Nonlinear oscillating systems are often studied by transforming the complex dynamic equations that describe their behavior into a phase coordinate representation [58, 210]. This approach, which yields simplified yet accurate models that capture essential overall properties of an oscillating system with a stable periodic orbit, was first used to examine interactions among rhythmic biological systems [28, 227, 228]. The classic phase coordinate transformation of nonlinear oscillators [149] was combined with formal averaging [127] and additional simplifications to develop the well-known Kuramoto model of coupled chemical oscillations [131]. This model reduction technique has subsequently been extensively applied, with a particular focus on neural [58, 105] and electrochemical [131, 121, 163] systems. Phase models are also widely used in physics, chemistry, and biology [178] to study systems where the phase, but not the state, can be observed, and where PRC can be approximated experimentally when the dynamics are unknown [71, 217, 122].

The reduction of a system model from a complicated set of differential equations to a simple scalar phase coordinate representation is especially compelling from a control-theoretic perspective because it enables a corresponding reduction in the complexity of optimal control problems involving that system. Optimal control of phase models has been investigated with various objectives, such as to alter the spiking of a single neuron using minimum energy inputs [157] with constrained amplitude [46, 45] and charge balancing [42, 44], as well as to control a network of globally coupled neurons [161]. Several studies have focused on optimal waveforms for entrainment using basic models [195, 95], and recent work has resulted in optimal entrainment controls for general nonlinear oscillators that require no knowledge about

the initial state or phase of the system [236], and can account for uncertainty in oscillation frequency [238]. These investigations have demonstrated that phase coordinate reduction provides a practical approach to the optimal control of complex oscillating systems.

This chapter contains a detailed derivation of the phase coordinate transformation for nonlinear oscillating systems. A fundamental and mathematically rigorous examination of phase reduction provides insight into the application of phase representations for modeling and control of real dynamical systems, and also leads to a straightforward numerical algorithm for computing the PRC. Phase reductions of several complex models of neuronal dynamics, including bursting neurons, are examined. A description of an experimental procedure for obtaining a phase model for the unknown dynamics of a periodic system from limited state observations is also provided. This method has been successfully applied in model identification for electrochemical oscillating systems in a laboratory setting.

4.1 Phase Model Reduction

Consider a full state-space model of an oscillating system, which is described by a smooth ordinary differential equation system of the form

$$\dot{x} = f(x, u), \quad x(0) = x_0, \quad t \in [0, \infty) \tag{4.1}$$

where $x(t) \in \mathbb{R}^n$ is the state and $u(t) \in \mathbb{R}^m$ is a control. Suppose further that (4.1) has an attractive, non-constant limit cycle $\gamma(t) = \gamma(t + T)$, which satisfies $\dot{\gamma} = f(\gamma, 0)$, on the periodic orbit $\Gamma = \{y \in \mathbb{R}^n \ : \ y = \gamma(t), \ 0 \leq t < T\} \subset \mathbb{R}^n$. In order to study the behavior of the system (4.1), its dynamics are reduced to a scalar equation

$$\dot{\psi} = \omega + Z(\psi)u, \tag{4.2}$$

which is called a phase model, where ω is the natural frequency of oscillation, Z is the phase response curve (PRC) and $\psi(t)$ is the phase associated to the isochron on which $x(t)$ is located. An isochron is the manifold in $\mathbb{R}^n$ on which all points have asymptotic phase $\psi(t)$ [26, 172]. The key idea of the transformation is that the phase ψ increases linearly with time on the limit cycle at the rate ω, as seen in Figures 4.1(a) and 4.1(b). The PRC, also referred to as the infinitesimal PRC or iPRC, quantifies the asymptotic phase shift due to an infinitesimal

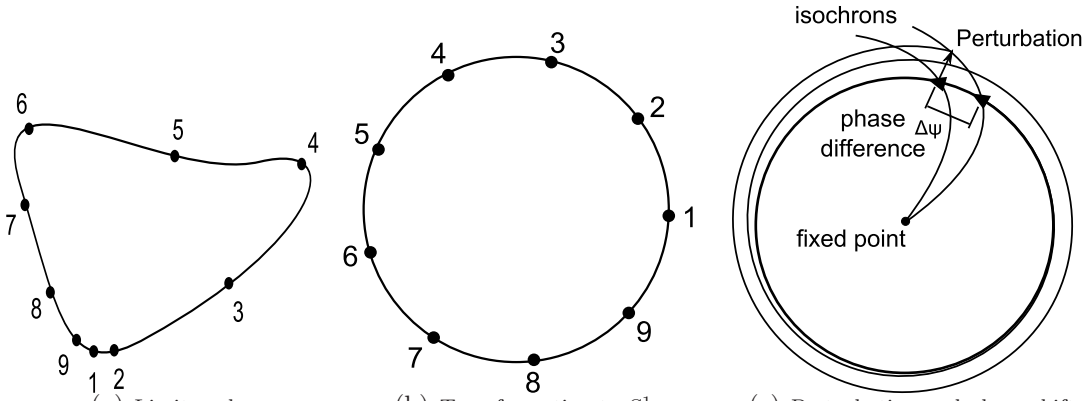

(a) Limit cycle (b) Transformation to S^1 (c) Perturbation and phase shift

Figure 4.1: (a) Locations of oscillator on the limit cycle at equally spaced time intervals. (b) Topological transformation of the limit cycle onto a circle. (c) Illustration of the phase shift that occurs due to a perturbation of the system by an input pulse.

perturbation in the state applied at a given phase on the limit cycle, as illustrated in Figure 4.1(c). It is standard practice to define $\psi(t) = 0 \pmod{2\pi}$ when a designated variable in the state vector x attains its maximum over the orbit Γ. This is due to the significant role of mathematical neuroscience in the development of phase model theory. For biophysical models of cellular neuron oscillators, the first state variable often denotes the membrane potential, which exhibits spiking or relaxation behavior, so that $\psi(t) = 2\pi k$ for $k = 1, 2, \ldots$ occur concurrently with successive spikes. The conditions for validity and accuracy of phase reduced models have been determined [56, 55], and the reduction is accomplished through the well-studied process of phase coordinate transformation [57], which is based on Floquet theory [176, 113]. The model is assumed valid for inputs $u(t)$ such that the solution $x(t, x_0, u)$ to (4.1) remains within a neighborhood U of Γ.

4.1.1 Phase Coordinate Transformation

The following is a basic summary of the technique for phase coordinate transformation, which is derived from the method of Malkin [149]. This derivation leads to a straightforward method for numerical computation of phase response curves, which is subsequently implemented to automatically compute phase models for parameter-dependent nonlinear oscillating control systems for numerous parameter sets. A collection of theorems regarding existence, accuracy, and validity of phase-reduced models has recently been compiled [55].

Recall the oscillating system (4.1) with a limit cycle $\gamma(t) = \gamma(t+T)$ on the periodic orbit Γ. A bijection can be defined between Γ and the circle S^1, which is homeomorphic to the interval $[0, 2\pi)$, hence any point $x \in \Gamma$ can be associated with a scalar phase $\phi \in [0, 2\pi)$ by the transformation $\alpha : \Gamma \to [0, 2\pi)$ with action $\alpha(x) = \phi$. The key idea is to choose the map α such that the phase is proportional to time on the the limit cycle, i.e., $\phi(t) = \omega t$, where $\omega = 2\pi/T$ is the natural frequency of the oscillation. This requirement can be expressed as $\alpha^{-1}(\phi) = \gamma(\phi/\omega)$ or as $\gamma(t) = \alpha^{-1}(2\pi t/T)$.

Denote by $x(t, x_0, u)$ the solution at time t to $\dot{x} = f(x, u)$ for a control input $u(t)$ and an initial condition $x(0) = x_0$. This results in $\gamma(t) = x(t, \alpha^{-1}(0), 0)$, so that if $x(0) = x_0 \in \Gamma$ then $x(t, x_0, 0) = \gamma(t + \alpha(x_0)/\omega)$. It is then possible to define the phase variable $\phi : [0, \infty) \to [0, 2\pi)$ corresponding to the trajectory $x(t, x_0, 0)$ with specific initial condition $x_0 \in \Gamma$ by $\phi(t) = \alpha(x(t, x_0, 0)) = \alpha(\gamma(t + \alpha(x_0)/\omega))$. Because $\gamma(t)$ is periodic, then $\phi(t)$ is periodic, and the given choice of α results in an affine system $\phi(t) = \omega t + \alpha(x_0)$, so that $\dot{\phi}(t) = \omega$. Given a specific $x_0 \in \Gamma$, one can define $\gamma(0) = x_0$, so that $\alpha(x_0) = \alpha(\gamma(0)) = 0$.

Next, denote by $\mathcal{A} = \{y \in \mathbb{R}^n \ : \ \lim_{t\to\infty} x(t, y, 0) \in \Gamma\} \subset \mathbb{R}^n$ the set attracted by the periodic orbit Γ, so if $x_0 \in \mathcal{A}$ then $x(t, x_0, 0) \in \mathcal{A}$ for $t \geq 0$. This allows the transformation α to be extended to solutions $x(t, x_0, 0)$ with $x_0 \in \mathcal{A}$, by implicitly defining an asymptotic phase map $\upsilon : \mathcal{A} \to [0, 2\pi)$ by $\lim_{t\to\infty} \|x(t, x_0, 0) - \gamma(t + \upsilon(x_0)/\omega)\| = 0$. In the case that $x_0 \in \Gamma$, then $\|x(t, x_0, 0) - \gamma(t + \alpha(x_0)/\omega)\| = 0$ for all $t \geq 0$ as described above, so that $\upsilon(x_0) = \alpha(x_0)$. This leads to a natural definition of the asymptotic phase variable $\psi : [0, \infty) \to [0, 2\pi)$ by $\psi(t) = \upsilon(x(t, x_0, 0))$ for $t \geq 0$, which is defined for $x_0 \in \mathcal{A}$. Therefore if $x_1, x_2 \in \mathcal{A}$ satisfy $\upsilon(x_1) = \upsilon(x_2)$, then $\upsilon(x(t, x_1, 0)) = \upsilon(x(t, x_2, 0))$ for all $t \geq 0$. This induces an equivalence class on $\mathcal{A}$ with equivalence $x_1 \sim x_2$ if $\upsilon(x_1) = \upsilon(x_2)$, which results in class elements $[x_0]$ in the quotient space $(\mathcal{A}/\sim) = \Gamma$, so that $\upsilon(x_0) = \alpha([x_0])$. The class element $[x_0]$ is commonly referred to as the isochron corresponding to the phase $\alpha([x_0])$.

This equivalence implies that the asymptotic phase is proportional to time for any trajectory $x(t, x_0, 0) \in \mathcal{A}$. Let $x_1 \in \mathcal{A}$ satisfy $x_1 \in [x_0]$ for $x_0 \in \Gamma$, so that $\upsilon(x_1) = \upsilon(x_0)$. Then $\psi(t) = \upsilon(x(t, x_1, 0)) = \upsilon(x(t, x_0, 0)) = \alpha(x(t, x_0, 0)) = \phi(t) = \omega t + \alpha(x_0) = \omega t + \upsilon(x_0) = \omega t + \upsilon(x_1)$. It follows that the asymptotic phase satisfies $\dot{\psi}(t) = \omega$, as desired. In addition, for any $x_1 \in \mathcal{A}$ one can define $\gamma(0) = [x_1] \in \Gamma$ so that $\upsilon(x_1) = \alpha([x_1]) = \alpha(\gamma(0)) = 0$. The following

diagram displays the relevant mappings and spaces:

$$\begin{tikzcd}
t \in [0,T) \arrow[r, "\alpha \circ \gamma"] \arrow[d, "\gamma"'] & \psi(t) \in [0,2\pi) \\
\gamma(t) \in \Gamma \arrow[ur, "\alpha"'] & x(t) \in \mathcal{A} \arrow[l, "\alpha^{-1} \circ \upsilon"] \arrow[u, "\upsilon"']
\end{tikzcd} \tag{4.3}$$

Finally, the notion of asymptotic phase can be simply extended to the case when $u(t) \neq 0$, provided that $x(t, x_0, u) \in \mathcal{A}$ for $t \geq 0$. One can define a new asymptotic phase map $\nu : \mathcal{A} \to [0, 2\pi)$ that acts by $\psi(t) = \nu(x(t, x_0, u)) = \upsilon(x(t, x_0, u)) = \alpha([x(t, x_0, u)])$, so that $\psi(t)$ at a time $t \geq 0$ evaluates the phase corresponding to the isochron $[x(t, x_0, u)]$.

4.1.2 Infinitesimal Phase Response

It is possible to use a linearization of the system $\dot{x} = f(x, u)$ about its limit cycle $\gamma(t)$ to obtain the ODE for the asymptotic phase variable $\psi(t)$ given infinitesimal inputs $u(t)$. Define the perturbation variable $\Delta x(t) = x(t) - \gamma(t)$, so that the linearization about γ is $\Delta\dot{x}(t) = A(t)\Delta\dot{x}(t) + b(t)u$ where

$$A(t) = \frac{\partial}{\partial x} f(x, 0)\Big|_{x=\gamma(t)} \quad \text{and} \quad b(t) = \frac{\partial}{\partial u} f(\gamma(t), u)\Big|_{u=0}. \tag{4.4}$$

Note that $A(t)$ and $b(t)$ are T-periodic because they depend on $\gamma(t)$, hence we can apply Floquet theory to the linearized system [176]. Consider a transition matrix $\Phi(t)$ that satisfies $\dot{\Phi}(t) = A(t)\Phi(t)$ with $\Phi(0) = I$, and its adjoint $\dot{\Psi}(t) = -A^{\dagger}(t)\Psi(t)$ with $\Psi(0) = I$, where $\dagger$ denotes the Hermitian transpose. Recall that $\Psi^{\dagger}(t)\Phi(t) = \Psi^{\dagger}(0)\Phi(0) \equiv I$, and that $y(t) = \Phi(t)y(0)$ if $\dot{y}(t) = A(t)y(t)$. Recall also Floquet's theorem [113], which states that because $A(t)$ is a continuous, T-periodic matrix, then for all $t \in \mathbb{R}$ any fundamental matrix solution $\Phi(t)$ for $\dot{x} = A(t)x$ can be written in the form $\Phi(t) = Q(t)e^{Bt}$ where $Q(t)$ is a nonsingular, differentiable, T-periodic matrix and B is a constant matrix. Observe that $Q(0) = I$ holds due to $\Phi(0) = I$.

Define the monodromy matrix $M(t) = \Phi(t+T)\Psi^\dagger(t)$, which is the linearized return map of the dynamical system. Applying Floquet's theorem yields

$$\begin{aligned} M(t) &= \Phi(t+T)\Psi^\dagger(t) = \Phi(t+T)\Phi^{-1}(t) \\ &= Q(t+T)e^{B(t+T)}e^{-Bt}Q^{-1}(t) = Q(t)e^{BT}Q^{-1}(t). \end{aligned} \tag{4.5}$$

Therefore $M(t)$ is T-periodic and isospectral, because $M(t)$ is similar to the constant matrix $M(0) = e^{BT}$. The eigenvalues λ_i of $M(t)$ are the Floquet multipliers of the linearization, each of which corresponds to an eigenvalue ρ_i of B, called characteristic exponents, where $\lambda_i = e^{\rho_i T}$. One of the Floquet multipliers is always 1, and by the stable manifold theorem the other $n-1$ multipliers are less than 1 [176].

In the case $u(t) = 0$, the limit cycle satisfies $\dot{\gamma}(t) = f(\gamma(t), 0)$, so that $\ddot{\gamma}(t) = A(t)\dot{\gamma}(t)$ and hence $\dot{\gamma}(t) = \Phi(t)\dot{\gamma}(0)$. In particular,

$$\begin{aligned} \dot{\gamma}(t) &= \dot{\gamma}(t+T) = \Phi(t+T)\dot{\gamma}(0) \\ &= \Phi(t+T)\Phi^{-1}(t)\dot{\gamma}(t) = M(t)\dot{\gamma}(t), \end{aligned} \tag{4.6}$$

hence $\dot{\gamma}(t) = f(\gamma(t), 0)$ is the unique eigenvector of $M(t)$ corresponding to the Floquet multiplier $\lambda = 1$, which has algebraic multiplicity of 1. Let $m(t) \in \mathbb{R}^n$ be the unique eigenvector of $M^\dagger(t)$ corresponding the eigenvalue $\lambda = 1$, so that $M^\dagger(t)m(t) = m(t)$, and scaled such that $m^\dagger(t)\dot{\gamma}(t) = \omega$. It follows that $m^\dagger(t)f(\gamma(t), 0) = m^\dagger(t)\dot{\gamma}(t) = \omega$.

Recall that the mapping ν acts by $\psi(t) = \nu(x(t, x_0, u))$, and which if chosen properly results in $\dot{\psi}(t) = \omega$ when $u = 0$. Then for $x_0 \in \Gamma$,

$$\begin{aligned} m^\dagger(t)f(\gamma(t), 0) = \omega = \dot{\psi} &= \frac{\mathrm{d}}{\mathrm{d}t}\nu(x(t, x_0, 0)) \\ &= \frac{\partial}{\partial x}\nu(x)\Big|_{x=\gamma(t)} \cdot \dot{\gamma}(t) = \frac{\partial}{\partial x}\nu(x)\Big|_{x=\gamma(t)} \cdot f(\gamma(t), 0) \end{aligned} \tag{4.7}$$

We may therefore infer that $m^\dagger(t) = \frac{\partial}{\partial x}\nu(x)\big|_{x=\gamma(t)}$, and deduce that $m(t)$ is T-periodic because $\gamma(t)$ is. When $u(t) \neq 0$, the linearized trajectory satisfies

$$\begin{aligned} \dot{\psi}(t) &= \frac{\partial}{\partial x}\nu(x)\Big|_{x=\gamma(t)+\Delta x(t)} \cdot \dot{x}(t) \\ &= \frac{\partial}{\partial x}\nu(x)\Big|_{x=\gamma(t)+\Delta x(t)} \cdot (f(\gamma(t), 0) + A(t)\Delta x(t) + b(t)u). \end{aligned} \tag{4.8}$$

The infinitesimal PRC is obtained by setting the perturbation to $\Delta x(t) = 0$, so that $\dot{\psi}(t) = \omega + m^\dagger(t)b(t)u$. Now when $\Delta x(t) = 0$ holds then $x(t) = \gamma(t)$ does as well, in which case $\psi(t) = \omega t$ as shown above, so setting $t = \psi(t)/\omega$ results in $m^\dagger(t)b(t) = m^\dagger(\psi/\omega)b(\psi/\omega)$. Consequently, the phase reduction of this linear system yields $\dot{\psi}(t) = \omega + Z(\psi)u$, where $Z(\psi) = m^\dagger(\psi/\omega)b(\psi/\omega)$ is the PRC.

Finally, observe that differentiating both sides of the equation $m^\dagger(t)\dot{\gamma}(t) = \omega$ results in $\dot{m}^\dagger(t)\dot{\gamma}(t) + m^\dagger(t)\ddot{\gamma}(t) = \dot{m}^\dagger(t)\dot{\gamma}(t) + m^\dagger(t)A(t)\dot{\gamma}(t) = 0$, hence

$$\dot{m}(t) = -A^\dagger(t)m(t). \tag{4.9}$$

Integrating both sides of the same expression results in

$$\int_0^T m^\dagger(t)\dot{\gamma}(t)\mathrm{d}t = \int_0^T \omega \mathrm{d}t = 2\pi. \tag{4.10}$$

Practical details involved in computing the PRC are discussed in the following section.

4.2 Computation of Phase Response Curves

One possible approach to obtaining the PRC is to integrate (4.9) and normalize the result according to (4.10), as previously suggested [58]. An alternative is to use optimization on a spectral representation of the PRC [82]. A software package called XPPAUT [59] is commonly used by researchers to perform the computation. In the technique described below, the PRC at each phase value is obtained directly from the eigenvector of the monodromy matrix. This approach is similar to computation of the perturbation projection vector (PPV) for noisy circuit elements [48].

First, the period $T = 2\pi/\omega$ and the limit cycle $\gamma(t)$ must be approximated to a high degree of accuracy. This can be done using a method for determining the steady-state response of non-linear oscillators [6], which is based on perturbation theory [114] and gradient optimization [175]. Observe first that

$$x(t, x_0, 0) = \int_0^T f(x(\tau, x_0, 0), 0)\mathrm{d}\tau + x_0, \tag{4.11}$$

and define an operator $K : \mathbb{R}^{n+1} \to \mathbb{R}^n$ by

$$K(y,T) := \int_0^T f(x(\tau, y, 0), 0)\mathrm{d}\tau + y, \tag{4.12}$$

so that y and T satisfy $K(y,T) = y$ only if $y \in \Gamma$ and T is a multiple of the period of oscillation. The relation $K(y,T) = y$ provides n equations for $n+1$ unknown variables, but because $\gamma(t)$ traverses a range of values on Γ, the first coordinate y_1 of $y = (y_1, \ldots, y_n)'$ lies in a broad range. Hence y_1 can be fixed at any point in this range. Therefore defining the operator $H : \mathbb{R}^n \to \mathbb{R}^n$ by $H(v) = y - K(y,T)$ where $v = (T, y_2, \ldots, y_n)$ and setting $H(v) = 0$ provides n equations in n unknowns. A gradient optimization method is used compute a solution v_* up to the required tolerance. Recall that a standard result on perturbation of initial conditions yields $\frac{\partial}{\partial y}x(t,y,0) = \Phi(t,0;y)$ [114], where $\Phi(t,0;y)$ is the transition matrix of the linearization about $x(t,y,0)$. Therefore the Jacobian of the operator H is given by

$$\frac{\partial H}{\partial y} = \frac{\partial}{\partial y}[y - K(y,T)] = I - \frac{\partial}{\partial y}x(T,y,0) = I - \Phi(T,0;y). \tag{4.13}$$

Additionally,

$$\frac{\partial H}{\partial T} = \frac{\partial}{\partial T}[y - K(y,T)] = -f(x(T,y,0),0), \tag{4.14}$$

therefore the Jacobian $DH(v) = \partial H/\partial v$ of the operator H is

$$\frac{\partial H}{\partial v} = \Big[\ -f(x(T,y,0),0);\quad [I - \Phi(T,0;y)]_2;\quad \ldots\quad ; [I - \Phi(T,0;y)]_n\ \Big] \tag{4.15}$$

where $[I - \Phi(T,0;y)]_k$ is the kth column of $[I - \Phi(T,0;y)]$. The following algorithm can be used to compute T and Γ:

Algorithm 2: Computation of Limit Cycles.

1. Select y_1 in the valid range of the steady state solution, and make an initial guess $v^{(0)} = (T^{(0)}, y_2^{(0)}, \ldots, y_n^{(0)}) \in \mathbb{R}^n$. The first coordinate of $y^{(k)}$ is always y_1. Select a tolerance ε.

2. For each step k, evaluate $H(v^{(k)}) = y^{(k)} - K(y^{(k)}, T^{(k)})$ and compute the derivative $DH(v^{(k)})$ as in (4.15). Apply a gradient optimization step, such as Newton-Raphson, $v^{(k+1)} = v^{(k)} - (DH(v^{(k)}))^{-1}H(v^{(k)})$.

3. If $\|v^{(k+1)} - H(v^{(k+1)})\| > \varepsilon$ go to Step 1.

4. Set $T^* = v_1^{(k+1)}$ and $y^* = (y_1, v_2^{(k+1)}, \ldots, v_n^{(k+1)})$. A limit cycle is given by $\gamma(t) = x(t, y^*, 0)$ for $t \in [0, T^*)$.

Once the limit cycle and period are computed, the PRC can be obtained as follows.

Algorithm 3: Computation of Phase Response Curve.

1. For each $\psi \in [0, 2\pi)$, let $x_\psi = \alpha^{-1}(\psi) = \gamma(\psi/\omega)$, and compute $x(t, x_\psi, 0)$ using $\dot{x}(t) = f(x(t), 0)$ for $x(0) = x_\psi$.

2. Let $A_\psi(t)$ be the linearization of $f(x(t), 0)$ about $\gamma_\psi(t) = \gamma(t+\psi/\omega)$, so that $\gamma_\psi(0) = x_\psi$. Compute $\Phi_\psi(T)$ where $\dot{\Phi}_\psi(t) = A_\psi(t)\Phi_\psi(t)$ with $\Phi_\psi(0) = I$.

3. Set $M_\psi = \Phi_\psi(T)$, and compute the eigenvector μ_ψ of $M_\psi^\dagger$.

4. Let $m_\psi = \omega(\mu_\psi^\dagger f(x_\psi, 0))^{-1} \cdot \mu_\psi$, and finally $Z(\psi) = m_\psi^\dagger b(\psi/\omega)$.

5. Verify computation using (4.10).

4.3 Examples of Phase Reduction

Algorithm 3 can be applied to compute the PRC for any oscillating system as described in Section 4.1. The present modeling and control approach has been developed to be universally applicable to arbitrary oscillating systems. However, the majority of the exploratory numerical work is conducted using the Hodgkin-Huxley system [99], which is a canonical model of complex nonlinear oscillatory behavior in neuroscience. The techniques have been verified for several models of complex dynamics found in neuron and electrochemical systems, as summarized below.

4.3.1 Phase Reduction of Neuron Models

Biophysical modeling of neuronal dynamics has a long history, and has yielded many models of the rich dynamical behavior that arises in neuronal systems at the cellular level [99, 159].

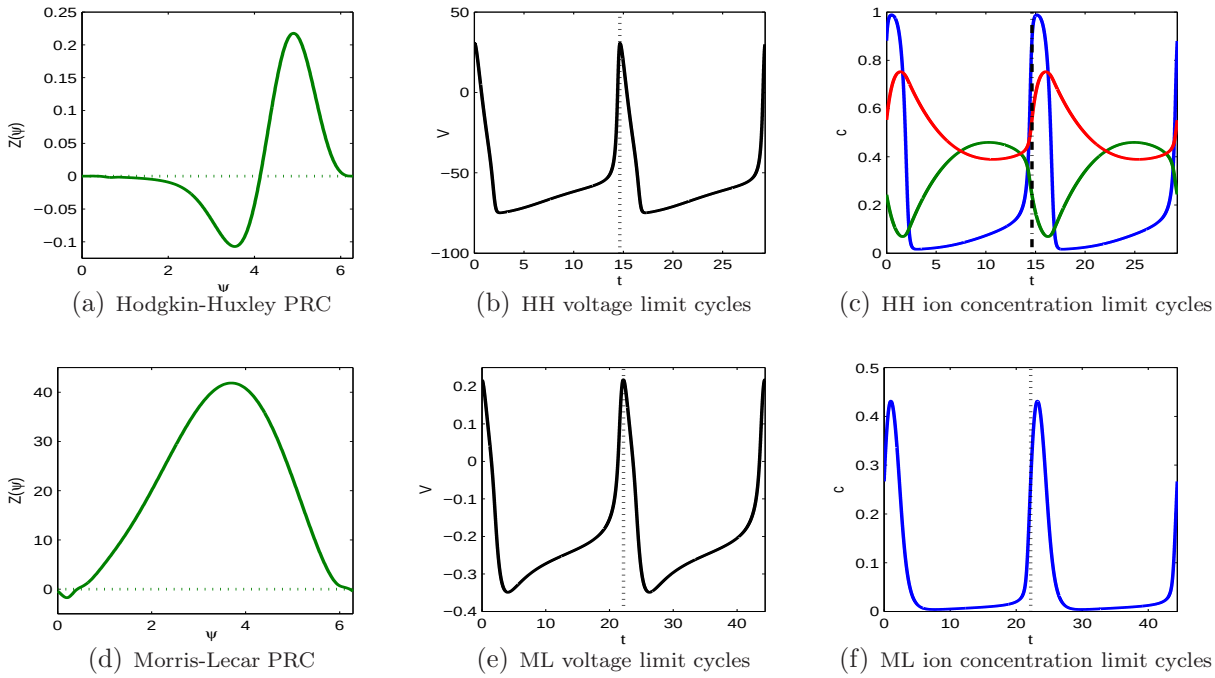

(a) Hodgkin-Huxley PRC (b) HH voltage limit cycles (c) HH ion concentration limit cycles

(d) Morris-Lecar PRC (e) ML voltage limit cycles (f) ML ion concentration limit cycles

Figure 4.2: (a) Hodgkin-Huxley phase response curve (PRC). The natural period and frequency of oscillation are $T \approx 14.638$ ms and $\omega \approx 0.4292$ rad/ms , respectively. (b) Hodgkin-Huxley voltage limit cycles, which exhibit relaxation oscillation that is referred to as "spiking" behavior. The phase $\psi = 0$ corresponds to "spikes", or maxima, of this membrane potential. (c) Hodgkin-Huxley ion concentration limit cycles. (d) Morris-Lecar PRC. The natural period and frequency of oscillation are $T \approx 22.1981$ ms and $\omega \approx 0.2831$ rad/ms, respectively. (e) Morris-Lecar voltage limit cycles, which exhibit "spiking" similar to the Hodgkin-Huxley model. (f) Morris-Lecar ion concentration limit cycles.

In particular, voltage gated conductance-based models for Beta synchrony in the subthalamic nucleus (STN) are of significant interest [51, 34, 207], in particular for understanding burst suppression phenomena [170]. Significant effort has recently been applied to develop highly detailed biophysical models of Beta oscillations in the STN and basal ganglia [153, 188, 216]. Control methodologies that are enabled by the simplification of such models to phase coordinates will provide a means for neuroscientists and medical technologists to leverage these developments to develop and optimize clinical modalities [80, 117, 34].

Two voltage-gated conductance (VGC) models are considered here, specifically the Hodgkin-Huxley model [99] and the Morris-Lecar model [159], which are described in detail in Appendices A.1 and A.2. The phase reductions of these systems are shown in Figure 4.2. In the computational neuroscience community, a neuron model with a PRC that is strictly positive is referred to as a Type I neuron. This category, for which positive stimuli can only advance the phase on the limit cycle, includes the Morris-Lecar model as seen in Figure 4.2(d). If

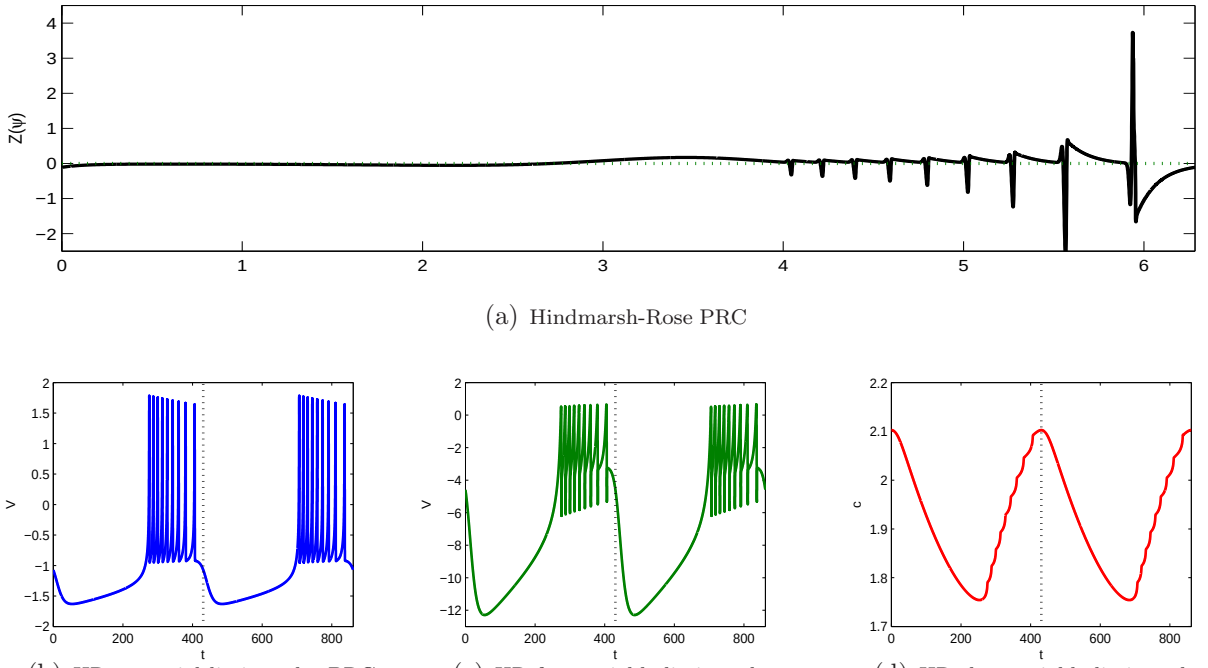

(a) Hindmarsh-Rose PRC

(b) HR potential limit cycles PRC (c) HR fast variable limit cycles (d) HR slow variable limit cycles

Figure 4.3: (a) Hindmarsh-Rose PRC. The natural period and frequency of oscillation are $T \approx 430.7756$ and $\omega \approx 0.0146$ non-dimensionalized units, respectively. (b) Hindmarsh-Rose potential limit cycles, which exhibit intermittent relaxation oscillations referred to as "bursting". (c) Hindmarsh-Rose fast variable limit cycles. (d) Hindmarsh-Rose slow variable limit cycles. The phase $\psi = 0$ corresponds to the point at which the slow variable attains its maximum.

the PRC is both positive and negative on significant portions of the limit cycle, the model is referred to as a Type II neuron. The Hodgkin-Huxley model, whose phase can be delayed or advanced by positive stimuli depending on the position on the limit cycle, is a Type II neuron, as shown in Figure 4.2(a).

In addition to VGC models, the phase coordinate transformation can also be applied to more complex systems that exhibit bursting behavior. Neurons do not exhibit constant oscillation, but rather are induced to produce bursts of oscillatory activity. Understanding and modeling this phenomenon is crucial to developing the ability to control local field potentials in neural tissues, and is consequently of significant interest to neuroscientists [49, 111, 133]. Such phenomena also appear under certain conditions in electrochemical systems [171]. A widely-studied example is the Hindmarsh-Rose model [98], which is described in Appendix A.3. The complex limit cycle, seen in Figures 4.3(b) to 4.3(d), result in a highly complex PRC for the system, which is shown in Figure 4.3(a). This computation of the Hindmarsh-Rose

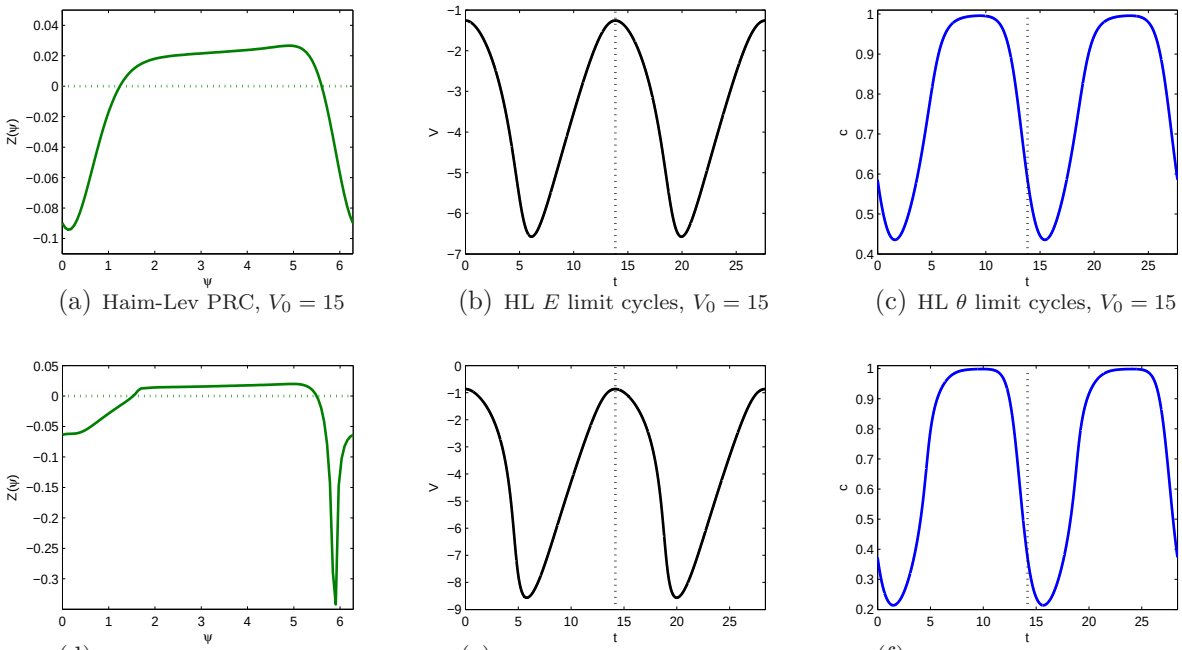

(a) Haim-Lev PRC, $V_0 = 15$ (b) HL E limit cycles, $V_0 = 15$ (c) HL θ limit cycles, $V_0 = 15$

(d) Haim-Lev PRC, $V_0 = 20$ (e) HL E limit cycles, $V_0 = 20$ (f) HL θ limit cycles, $V_0 = 20$

Figure 4.4: (a) Haim-Lev phase response curve (PRC). The natural period and frequency of oscillation are $T \approx 13.8464$ and $\omega \approx 0.4538$ nondimensionalized units, respectively. The domain is $\psi \in [0, 2\pi]$. (b) Haim-Lev potential limit cycles, which exhibit mild relaxation oscillation. The phase $\psi = 0$ corresponds to maxima of the potential variable E. (c) Haim-Lev chemical concentration limit cycles. (d) Increasing the baseline potential to $V_0 = 20$ increases the complexity in the PRC, and greater relaxation behavior in the limit cycle, as seen in (e) and (f).

PRC confirms previous results [199], which were found using an alternate implementation [82].

4.3.2 Phase Reduction of Haim-Lev Electrochemical System

Phase response curves are also important for modeling oscillatory phenomena in electrochemical systems. The control methodologies derived here have been applied to an experimental apparatus for studying the electrodissolution of nickel in sulfuric acid, whose dynamics can be approximated by the Haim-Lev (HL) system given in Appendix A.4. The PRC of the Haim-Lev system is shown in Figure 4.4(a), while the limit cycles of the potential and chemical concentration variables are shown in Figures 4.4(b) and 4.4(c). Observe that increasing the baseline electrode potential V_0 from 15 to 20 results in a qualitative change in the phase response, as seen in Figure 4.4(d).

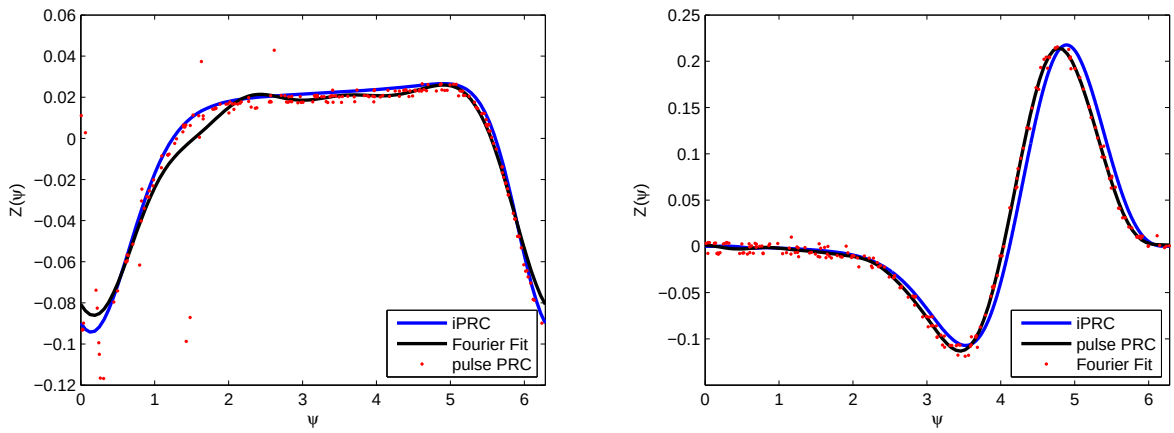

(a) Estimation of HL PRC (b) Estimation of HH PRC

Figure 4.5: (a) Simulation of estimation of the PRC of the Haim-Lev electrochemical oscillator model using the model identification technique in Section 4.4. The dots are obtained using (4.18) and (4.19) on postprocessing of an input pulse train with $M = 20$, $\Delta t = 0.02$, sampling frequency $f_s = 400$, 200 pulses, and a relaxation time of $N = 3$ periods. A Fourier series fit using order 5 is shown in black, compared to the infinitesimal PRC in blue. (b) The same simulation for the Hodgkin-Huxley neuron model, with $M = 10$ and a Fourier series fit of order 8.

4.4 Model Identification for Oscillating Systems

In addition to its utility as a model reduction tool that facilitates analysis and control design for complex oscillating systems, the phase model framework provides a very general method for model identification of such systems for which the dynamics are unknown. Several approaches have been used to estimate the PRC in real oscillating systems subject to noise and disturbances [71, 165, 122]. In this section, a straightforward method for approximating the PRC of noisy oscillators is presented. In particular, this approach does not require online state observations or feedback, but rather relies on post-processing of a pseudo-random input sequence and the observed output.

Suppose that a brief, strong pulse of duration Δt and magnitude M is applied to an oscillator at time t_0, when the phase is $\psi(t_0)$. Specifically, suppose $u(t) = M$ for $t \in [t_0, t_0 + \Delta t]$, and $u(t) = 0$ elsewhere. Let $\psi_1(t_0 + NT)$ and $\psi_0(t_0 + NT)$ represent the phase value N natural periods after the pulse is applied, and in the absence of a pulse, respectively. Because Γ is strongly attractive, the system will relax back to the periodic orbit several cycles after the pulse is applied. Assuming that the pulse duration Δt is brief, $Z(\psi(t))$ is approximately

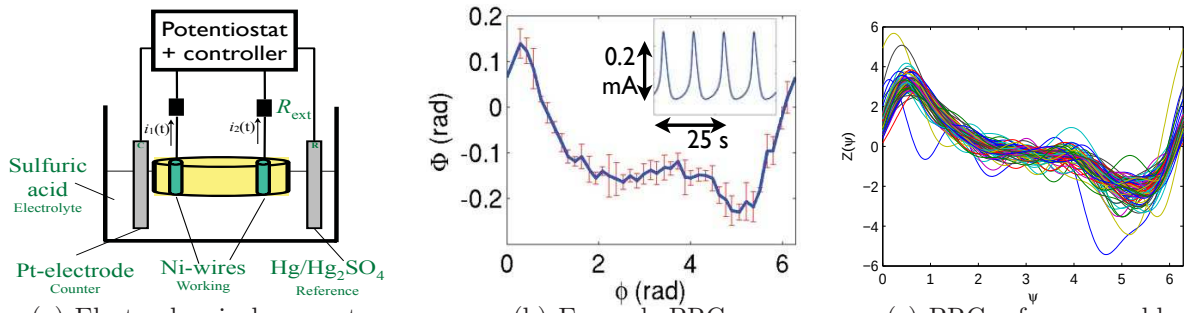

(a) Electrochemical apparatus (b) Example PRC (c) PRCs of an ensemble

Figure 4.6: Engineered experimental system for phase model based control of electrochemical oscillations. (a) Schematic of experimental setup. (b) Typical PRC and waveform (inset) of the electrochemical oscillator [95] for relaxation oscillations occurring at $V = 1.200\,V$, $R_{ext} = 1k\Omega$, computed using a method that requires feedback [122]. (c) PRCs of an array of 79 electrochemical oscillators that were computed simultaneously using the method in Section 4.4. The frequencies are approximately uniformly distributed between 0.4 and 0.46 Hz.

constant on $t \in [t_0, t_0 + \Delta t]$, so that integrating (4.2) results in

$$\psi_0(t_0 + NT) = \omega NT + \psi(t_0), \tag{4.16}$$

$$\begin{aligned}\psi_1(t_0 + NT) &= \omega NT + \psi(t_0) + \int_{t_0}^{t_0+\Delta t} Z(\psi(t))M\mathrm{d}t \\ &\approx \omega NT + \psi(t_0) + Z(\psi(t_0))M\Delta t.\end{aligned} \tag{4.17}$$

Subtracting (4.16) from (4.17) and solving for $Z(\psi(t_0))$ results in

$$Z(\psi(t_0)) = \frac{\psi_1(t_0 + NT) - \psi_0(t_0 + NT)}{M\Delta t} \tag{4.18}$$

The phase difference $\psi_1(t_0 + NT) - \psi_0(t_0 + NT)$ can be approximated using a linear interpolation technique [178]. If $y(t)$ is the observed oscillator output, let T_{-1} and T_N denote the latest time at which $y(t)$ reaches a peak before time t_0, and the time when $y(t)$ reaches the Nth peak after the pulse is applied. Recall that phase is linearly proportional to time, so that for two time points $t_1, t_2 \in [0, T)$ the transformations in the diagram (4.3) satisfy $(\alpha \circ \gamma)(t_1 - t_2) = (\alpha \circ \gamma)(t_1) - (\alpha \circ \gamma)(t_2)$. As a result, the linear interpolation yields

$$\begin{aligned}\psi_1(t_0 + NT) - \psi_0(t_0 + NT) &\approx (\alpha \circ \gamma)(T_N - T_{-1}) - (\alpha \circ \gamma)((N+1)T) \\ &= 2\pi \cdot \frac{(T_N - T_{-1}) - (N+1)T}{T},\end{aligned} \tag{4.19}$$

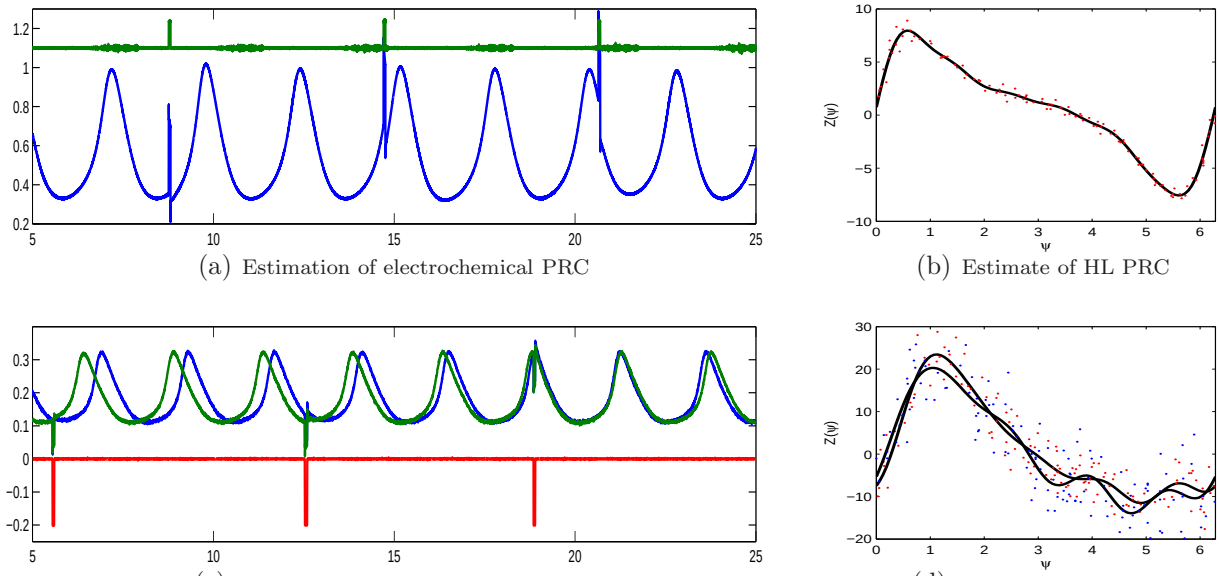

(a) Estimation of electrochemical PRC (b) Estimate of HL PRC

(c) Estimation of electrochemical PRCs (d) Estimate of HL PRCs

Figure 4.7: (a) Input pulse sequence (green) and observed current (blue) of electrochemical apparatus. Baseline potentiostat voltage is set at $V_0 = 1.1$, pulses have amplitude $M = .2$ Volts and width $\Delta t = 0.05$ seconds, and a sample rate $f_s = 1000$ is used for measurement. (b) The PRC obtained using the model identification method in Section 4.4. Period of oscillation is $T \approx 2.62$ sec. (c) Common input and observed current of two oscillators. Here $V_0 = 1.2$, $M = -.2$ Volts, and sample rate $f_s = 200$. (d) The estimated PRCs of two oscillators with similar PRC but different periods of $T_1 = 2.385$ and $T_2 = 2.480$.

after sufficiently many, i.e., N, cycles have passed. Therefore, a sequence of pulses at intervals of $T(N + r_j)$, where $r \in (0, 1)$ is pseudo-random, can be applied to an oscillator, and the peak times and pulse times can be used in a postprocessing step to create a plot of $Z(\psi)$ vs. ψ, which can be fitted using a Fourier series to estimate the PRC.

The above method for phase model identification can be simulated numerically. Figure 4.5 shows the results of such simulations for the Hodgkin-Huxley and Haim-Lev systems, which are described in Appendices A.1 and A.4, respectively. Each data point is the phase shift measured due to an applied pulse, and these points are fitted to a Fourier series, which is compared to the infinitesimal PRC computed using Algorithm 3.

The true advantage of the phase modeling technique for oscillating systems lies in the ability to estimate the phase dynamics of form (4.2). This technique was first validated through numerical simulation as described above, and was subsequently applied to estimate phase models in electrochemical oscillating systems, of which a description can be found in Appendix A.4. A schematic of the experimental apparatus, as well as an example PRC and limit cycle, are shown in Figure 4.6. Examples of input pulses and measured current output

in the apparatus are shown in Figure 4.7. One important advantage of this approach is to enable the concurrent identification of the PRCs for a large ensemble of rhythmic systems with simultaneously measurable output. The same pseudo-random pulse input sequence can be applied to the entire ensemble, and the recorded output measurement signal for each oscillator can then subsequently be processed off-line to produce a collection of phase models, as illustrated in Figure 4.6(c).

Chapter 5

Optimal Entrainment of Nonlinear Oscillators

The process of entrainment, which refers to the dynamic synchronization of an oscillating system to a periodic input, is significant in biology [93, 60, 77, 83], with particular relevance in neuroscience [49, 20, 201], and is also observed in reactive chemical systems [131, 8, 136]. The notion of entrainment is paramount for understanding rhythmic systems, as well as for controlling such systems in an optimal manner [84, 95]. Optimization of this process can significantly improve stimulation techniques in applications involving synchronization or desynchronization of neural systems, such as deep brain stimulation (DBS) [213, 214]. The periodic input can be adjusted to optimize an objective for a specific entrainment feature, such as the rate of entrainment [84], circadian phase resetting [10, 68], and maximum energy transfer between the input and the system [76]. Optimal entrainment also has compelling applications in clinical medicine, such as protocols for coping with jet lag [224, 202], clinical treatments for neurological disorders including epilepsy [118, 80], Parkinson's disease [101], and tinnitus [209], and optimization of cardiac pacemakers [164]. Techniques for controlling the entrainment process can also be used in the design of vibrating mechanical structures [22, 230] and nanoscale electromechanical devices [64, 13] that require frequency control or phase locking, and can enable transformational technologies such as neurocomputers [107] and chaos communication [66]. Various phenomena such as noise-induced synchronization [225], time-scales in synchronization and network dynamics [32, 31], and transient phenomena [84, 235] have been examined.

The entrainment, and hence frequency control, of an oscillating system can be examined by considering its phase response curve (PRC) [110, 109], which quantifies the shift in asymptotic phase due to an infinitesimal perturbation in the state. Phase models have become indispensable in physics, chemistry, and biology for studying oscillating systems where the full state-space model is complicated or even unknown, but where the phase can be estimated from partial state observations, and the PRC can be approximated experimentally [178]. They have been successfully applied to investigate many synchronization phenomena [210], focusing on synchronization emerging in networks of interacting oscillators and on the response of large collections of oscillators to periodic external stimuli [186, 103]. Such models have long been of interest to neuroscientists [179, 58], for whom the intrinsic occurrence and extrinsic imposition of entrainment in networked oscillators is of particular interest [20, 201]. Several studies have been motivated by the prospect of using dynamical systems theory to improve the effectiveness of DBS as a clinical therapy for epilepsy and Parkinson's disease [214, 177, 80]. Concurrently, others have concentrated on the use of phase models in order to attain desired design objectives for electrochemical [121, 163] and neural [105, 108] systems, including recent work that approaches the use of phase models in neuroscience from a control theoretic perspective [221, 160]. The control of neural spiking using minimum energy inputs with constrained amplitude and charge balancing has also recently been examined [46, 47]. These studies have demonstrated that phase-model reduction provides a practical approach to synthesizing near-optimal controls that achieve design goals for oscillating neural systems.

5.1 Theory of Entrainment by Weak Forcing

An essential objective in all entrainment applications is to force the frequency of an oscillator to a desired value. While this can be accomplished using any sufficiently powerful rhythmic signal, it is often desirable to do so using an input that consumes minimum energy, or satisfies another optimization objective. The theory of entrainment by weak forcing is described in this section.

Our goal is to entrain the system (4.2) to a target frequency Ω using a periodic forcing control $u(t)$ of the same frequency, so that the control input has the form $u(t) = v(\Omega t)$, where v is 2π-periodic. The weak forcing assumption is adopted, i.e., $v = \varepsilon v_1$ where v_1 has unit energy and $\varepsilon << 1$, so that given this control the state of the original system (4.1) is guaranteed

to remain in a neighborhood U of Γ in which the phase model (4.2) remains valid [56]. We then define a slow phase variable by $\phi(t) = \psi(t) - \Omega t$, and call the difference $\Delta\omega = \omega - \Omega$ between the natural and target frequencies the frequency detuning. The dynamic equation for the slow phase is then

$$\dot{\phi} = \dot{\psi} - \Omega = \Delta\omega + Z(\Omega t + \phi)v(\Omega t), \tag{5.1}$$

where $\dot{\phi}$ is called the phase drift. In order to study the asymptotic behavior of (5.1) it is necessary to eliminate the explicit dependence on time on the right hand side, which can be accomplished by using formal averaging [131]. Be denoting $\mathcal{P} = \{x : \mathbb{R} \to \mathbb{R} \ : \ x(\theta) = x(\theta + 2\pi)\}$ as the set of 2π-periodic functions on $\mathbb{R}$, we can define an averaging operator $\langle\cdot\rangle : \mathcal{P} \to \mathbb{R}$ by

$$\langle x \rangle = \frac{1}{2\pi}\int_0^{2\pi} x(\theta)\mathrm{d}\theta. \tag{5.2}$$

Defining the forcing phase $\theta = \Omega t$, the weak ergodic theorem for measure-preserving dynamical systems on the torus [127] implies that for any periodic input v, the interaction function

$$\begin{aligned}\Lambda_v(\phi) &= \langle Z(\theta + \phi)v(\theta)\rangle \\ &= \frac{1}{2\pi}\int_0^{2\pi} Z(\theta + \phi)v(\theta)\mathrm{d}\theta \\ &= \lim_{T\to\infty}\frac{1}{T}\int_0^{T} Z(\Omega t + \phi)v(\Omega t)\mathrm{d}t\end{aligned} \tag{5.3}$$

exists as a continuous, 2π-periodic function in $\mathcal{P}$. The formal averaging theorem [104] permits us to approximate (5.1) by the averaged system

$$\dot{\varphi} = \Delta\omega + \Lambda_v^{NM}(\varphi) + \mathcal{O}(\varepsilon^2) \tag{5.4}$$

in the sense that there exists a change of variables $\varphi = \phi + \varepsilon h(\varphi, \phi)$ that maps solutions of (5.1) to those of (5.4). The $\mathcal{O}(\varepsilon^2)$ accuracy of the approximation (5.4) is derived in the following section, as described in [238].

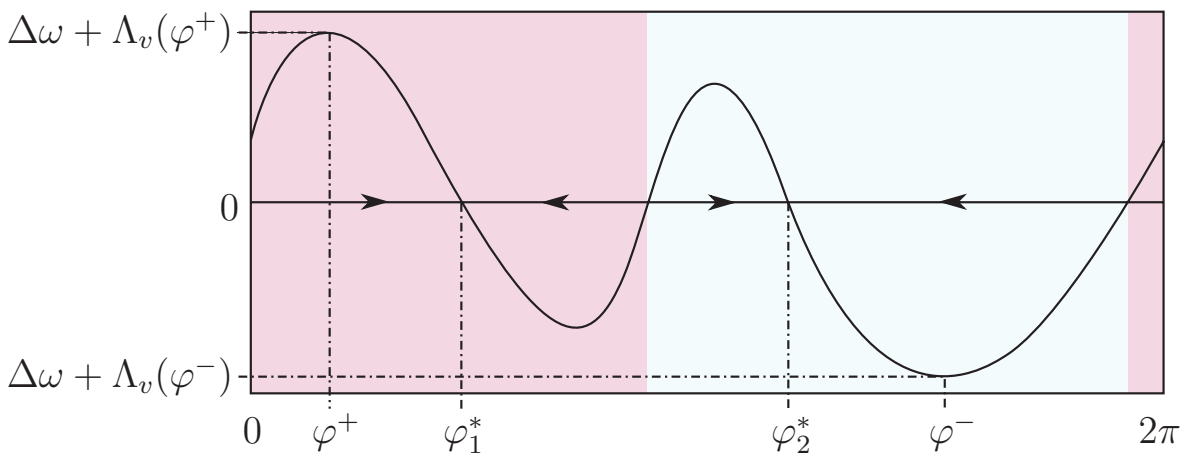

Figure 5.1: Illustration of important properties of an interaction function $\Lambda_v(\varphi)$. The maximum and minimum values $\Lambda_v(\varphi^+)$ and $\Lambda_v(\varphi^-)$, which occur at the phases φ^+ and φ^-, respectively, determine the range of frequency detuning for which the oscillator can be entrained using weak forcing. The roots of the equation $\Delta\omega + \Lambda_v(\varphi) = 0$ determine the average phase shift, relative to $\Omega_f t$, at which the oscillation stabilizes from a given initial phase. For initial phase in the pink (resp. blue) range, the asymptotic phase shift will be φ_1^* (resp. φ_2^*). The arrows indicate the evolution of the phase φ in equation 5.5.

5.1.1 Formal Averaging Approximation

Given a periodic input $v(\Omega t)$ with period T and frequency $\Omega = 2\pi/T$, denote the forcing phase $\theta = \Omega t$, so that $\mathrm{d}\theta = \Omega \mathrm{d}t$. Kuramoto [131] bases his theory on the idea that if the forcing is "weak", then the phase difference $\phi(t) = \psi(t) - \Omega t$ is "slow", so $\phi(t)$ is nearly constant over a single period $[0, T]$. Therefore we substitute $\theta = \Omega t$ and write

$$\begin{aligned}\dot{\phi} &= \Delta\omega + Z(\phi + \Omega t)v(\Omega t) \approx \Delta\omega + \frac{1}{T}\int_0^T Z(\phi + \Omega t)v(\Omega t)\mathrm{d}t \\ &= \Delta\omega + \frac{1}{2\pi}\int_0^{2\pi} Z(\phi + \theta)v(\theta)\mathrm{d}\theta\end{aligned}$$

By defining the interaction function $\Lambda_v(\phi) = \langle Z(\phi + \theta)v(\theta)\rangle$, the phase drift dynamics become $\dot{\phi} = \Delta\omega + \Lambda_v(\phi)$. This approach can be justified more rigorously as follows. Let $\zeta = \phi - \Delta\omega t$, so

$$\begin{aligned}\dot{\zeta} = \dot{\phi} - \Delta\omega \quad &= \quad Z(\phi + \theta)k(\theta) \quad = \quad \varepsilon Z(\zeta + \Delta\omega t + \theta)k_1(\theta) \\ = \varepsilon Z(\zeta + (\Delta\omega/\Omega + 1)\theta)k_1(\theta) \quad &=: \quad \varepsilon g(\zeta, \theta) \quad = \quad \varepsilon g(\zeta, \Omega t)\end{aligned}$$

We now state the following theorem, which is a modification of Theorem 9.4 in [104].

Theorem 2: Formal averaging. Consider a dynamical system $\dot{\zeta} = \varepsilon g(\zeta, \theta)$ where g is 2π-periodic in both ζ and θ. Suppose the average of g, given by

$$\overline{g}(\varphi) = \lim_{T\to\infty} \frac{1}{T}\int_0^T g(\varphi, \Omega t)\mathrm{d}t = \frac{1}{2\pi}\int_0^{2\pi} g(\varphi, \theta)\mathrm{d}\theta = \langle g(\phi, \theta)\rangle$$

exists as a smooth function for $\varphi \in \mathbb{R}$. Then $\dot{\varphi} = \varepsilon\overline{g}(\varphi) + \mathcal{O}(\varepsilon^2)$ approximates $\dot{\zeta} = \varepsilon g(\zeta, \theta)$, in the sense that there is a change of variables $\zeta = \varphi + \varepsilon h(\varphi, \theta)$ where

$$h(\varphi, \theta) = \frac{1}{\Omega}\int_0^\theta [g(\varphi, \sigma) - \overline{g}(\varphi)]\mathrm{d}\sigma$$

that maps solutions of $\dot{\zeta} = \varepsilon g(\zeta, \theta)$ to those of $\dot{\varphi} = \varepsilon\overline{g}(\varphi) + \mathcal{O}(\varepsilon^2)$.

Proof: We first note that $\overline{g}(\varphi) = \langle g(\varphi, \theta)\rangle$ is a result of the weak ergodic theorem for measure-preserving dynamical systems on the torus [127]. Substitute $\zeta = \varphi + \varepsilon h(\varphi, \theta)$ into $\dot{\zeta} = \varepsilon g(\zeta, \theta)$, so

$$\dot{\zeta} = \left(1 + \varepsilon\frac{\partial}{\partial\varphi}h(\varphi, \theta)\right)\dot{\varphi} + \varepsilon\frac{\partial}{\partial\theta}h(\varphi, \theta) = \varepsilon g(\varphi, \theta) + \mathcal{O}(\varepsilon^2).$$

Because $\left(1 + \varepsilon\frac{\partial}{\partial\varphi}h(\varphi, \theta)\right)^{-1} = 1 - \varepsilon\frac{\partial}{\partial\varphi}h(\varphi, \theta) + \mathcal{O}(\varepsilon^2)$, then

$$\begin{aligned}\dot{\varphi} &= \varepsilon g(\varphi, \theta) - \varepsilon\frac{\partial}{\partial\theta}h(\varphi, \theta)\Omega + \mathcal{O}(\varepsilon^2)\\ &= \varepsilon g(\varphi, \theta) - \varepsilon[g(\varphi, \theta) - \overline{g}(\varphi)] + \mathcal{O}(\varepsilon^2) = \varepsilon\overline{g}(\varphi) + \mathcal{O}(\varepsilon^2)\end{aligned}$$

When $\varepsilon << 1$, the solution to $\dot{\varphi} = \varepsilon\overline{g}(\varphi)$ approximates the solution to $\dot{\zeta} = \varepsilon g(\zeta, \theta)$ up to order $\mathcal{O}(\varepsilon)$. □

The averaged phase drift equations therefore satisfy

$$\begin{aligned}\dot{\phi} = \dot{\zeta} + \Delta\omega \;&=\; \Delta\omega + \varepsilon g(\zeta, \theta)\\ = \Delta\omega + \varepsilon\overline{g}(\zeta) + \mathcal{O}(\varepsilon^2) \;&=\; \Delta\omega + \varepsilon\langle g(\zeta, \theta)\rangle + \mathcal{O}(\varepsilon^2)\\ = \Delta\omega + \langle Z(\phi + \theta)v(\theta)\rangle + \mathcal{O}(\varepsilon^2) \;&=\; \Delta\omega + \Lambda_v(\phi) + \mathcal{O}(\varepsilon^2),\end{aligned}$$

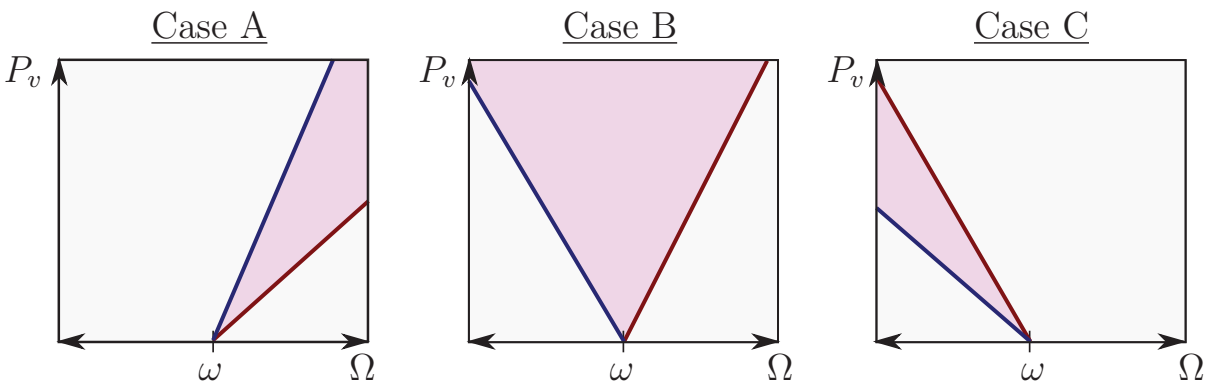

Figure 5.2: Illustration of Arnold tongues for the three cases listed in Table 5.1. The left boundary is shown in blue, and the right boundary is shown in red.

and hence the weak forcing assumption $v = \varepsilon v_1$ with $\varepsilon << 1$ allows us to approximate the phase drift equation by the time-independent averaged equation

$$\dot{\varphi} = \Delta\omega + \Lambda_v(\varphi). \tag{5.5}$$

As a result, we say that the system is entrained by a control $u = v(\Omega t)$ when the phase drift equation (5.5) satisfies $\dot{\varphi} = 0$. This will eventually occur if there exists a phase φ_* satisfying $\Delta\omega + \Lambda_v(\varphi_*) = 0$. In the following section, we investigate and characterize the conditions when entrainment occurs.

5.1.2 Locking Regions of Periodically Forced Oscillators

The averaged equation (5.5) is autonomous, and approximately characterizes the asymptotic behavior of the system (4.2) under periodic forcing. Specifically, we say that the system is entrained by a control $u = v(\Omega t)$ when the phase drift equation (5.5) satisfies $\dot{\varphi} = 0$, which will occur as $t \to \infty$ if there exists a phase φ_* that satisfies $\Delta\omega + \Lambda_v(\varphi^*) = 0$. When both the control waveform v and PRC Z are non-zero, the function $\Lambda_v(\varphi)$ is not identically zero, so when the system is entrained there exists at least one $\varphi_* \in [0, 2\pi)$ that is an attractive fixed point of (5.5). The stable fixed points $\{\varphi_i^*\}$ of (5.5), which are the roots of the equation $\Delta\omega + \Lambda_v(\varphi) = 0$, determine the average phase shift, relative to Ωt, at which the oscillation stabilizes from a given initial phase. In addition, we define the phases $\varphi^+ = \arg\max_\varphi \Lambda_v(\varphi)$ and $\varphi^- = \arg\min_\varphi \Lambda_v(\varphi)$ at which the interaction function achieves its maximum and minimum values, respectively. In order for entrainment to occur,

Case A:	$0 < \Lambda_{\widetilde{v}}(\varphi^-) < \Lambda_{\widetilde{v}}(\varphi^+)$		
Frequency:	$\Omega > \omega$		$\Omega < \omega$
Boundary:	left/top	right/bottom	N/A
$P_v^{NM}(\Omega)$	$-\Delta\omega/\Lambda_{\widetilde{v}}(\varphi^-)$	$-\Delta\omega/\Lambda_{\widetilde{v}}(\varphi^+)$	N/A
Case B:	$\Lambda_{\widetilde{v}}(\varphi^-) < 0 < \Lambda_{\widetilde{v}}(\varphi^+)$		
Frequency:	$\Omega > \omega$		$\Omega < \omega$
Boundary:	left		right
$P_v^{NM}(\Omega)$	$-\Delta\omega/\Lambda_{\widetilde{v}}(\varphi^-)$		$-\Delta\omega/\Lambda_{\widetilde{v}}(\varphi^+)$
Case C:	$\Lambda_{\widetilde{v}}(\varphi^-) < \Lambda_{\widetilde{v}}(\varphi^+) < 0$		
Frequency:	$\Omega > \omega$	$\Omega < \omega$	
Boundary:	N/A	left/bottom	right/top
$P_v^{NM}(\Omega)$	N/A	$-\Delta\omega/\Lambda_{\widetilde{v}}(\varphi^-)$	$-\Delta\omega/\Lambda_{\widetilde{v}}(\varphi^+)$

Table 5.1: Arnold tongue boundaries derived from (5.6), where $\Delta\omega \triangleq \omega - \Omega$.

$-\Lambda_v(\varphi^+) \leq \Delta\omega \leq -\Lambda_v(\varphi^-)$ must hold, so that at least one stable fixed point of Λ_v exists. Thus the range of the interaction function determines which values of the frequency detuning $\Delta\omega$ yield phase locking. These properties are illustrated in Figure 5.1.

The interaction function provides an expedient estimate for the value of the minimum root mean square (RMS) energy $P_v(\Omega) = \sqrt{\langle v^2 \rangle}$ that results in locking of an oscillator to a given frequency Ω using the waveform v. This is accomplished by substituting the expression $v(\theta) = P_v(\Omega)\widetilde{v}(\theta)$ into the equation $\Delta\omega + \Lambda_v(\varphi) = 0$ and simplifying to obtain

$$\omega - \Omega + P_v(\Omega) \cdot \Lambda_{\widetilde{v}}(\varphi) = 0, \tag{5.6}$$

where $\widetilde{v}$ is a unit energy normalization of v. This equation is then solved for $P_v(\Omega)$ at $\varphi = \varphi^+$ and $\varphi = \varphi^-$ to produce linear estimates of boundaries for the regions of pairs $(\Omega, P_v) \in \mathbb{R}^2$ that yield entrainment. These regions are known as Arnold tongues, so named after mathematician who first described a similar phenomenon for recurrent maps on the circle (Section 12 of [7]). The RMS energy is used because the boundary of the entrainment region is approximately linear for weak forcing, and yields a clear visualization [61, 195]. The Arnold tongue boundary estimates obtained using (5.6) can be classified into three different cases that depend on the signs of $\Lambda_{\widetilde{v}}(\varphi^+)$ and $\Lambda_{\widetilde{v}}(\varphi^-)$, which are listed in Table 5.1 and illustrated in Figure 5.2.

Based on the theoretical foundation and fundamental notations presented in this section, we proceed to formulate and solve several design and optimization problems for entrainment of an oscillating system. In the following section, we address the canonical problem of establishing harmonic resonance of a single oscillator with a periodic input of minimum energy at a desired frequency.

5.2 Minimum-Energy Entrainment

In practical applications, it is desirable to achieve entrainment with a control of minimum energy. This problem can be formulated as a variational optimization problem in the following manner. The objective function to be minimized is the energy $\langle v^2 \rangle$, and entrainment can be achieved when $\omega + \Lambda_v(\varphi_+) \geq \Omega$ if $\Omega > \omega$ and $\omega + \Lambda_v(\varphi_-) \leq \Omega$ if $\Omega < \omega$. This inequality is active for the optimal waveform, and hence can be expressed as the equality constraint

$$\begin{aligned} \Delta\omega + \Lambda_v(\varphi_+) &= 0 \qquad \text{if} \qquad \Omega > \omega, \\ \Delta\omega + \Lambda_v(\varphi_-) &= 0 \qquad \text{if} \qquad \Omega < \omega. \end{aligned} \tag{5.7}$$

We formulate the problem for $\Omega > \omega$ to obtain the minimum energy control v_+ using the calculus of variations [74]. The derivation of the case where $\Omega < \omega$ is similar, and results in the symmetric control v_-. The constraint (5.7) can be adjoined to the objective using a multiplier λ, resulting in the cost

$$\begin{aligned} \mathcal{J}[v] &= \left\langle v^2 \right\rangle - \lambda(\Delta\omega + \Lambda_v(\varphi_+)) \\ &= \left\langle v^2 \right\rangle - \lambda\left(\Delta\omega + \frac{1}{2\pi}\int_0^{2\pi} Z(\theta + \varphi_+)v(\theta)\mathrm{d}\theta\right) \\ &= \frac{1}{2\pi}\int_0^{2\pi} [v(\theta)(v(\theta) - \lambda Z(\theta + \varphi_+)) - \lambda\Delta\omega]\mathrm{d}\theta. \end{aligned} \tag{5.8}$$

Applying the Euler-Lagrange equation, $L_x(\theta, v(\theta), v'(\theta)) = \frac{\mathrm{d}}{\mathrm{d}\theta}L_y(\theta, v(\theta), v'(\theta))$ for $L(t, x, y) = x(t)(x(t) - \lambda Z(t + \varphi_+)) - \lambda\Delta\omega$, we obtain the necessary condition for an optimal solution, which yields a candidate function

$$v(\theta) = \frac{\lambda}{2}Z(\theta + \varphi_+), \tag{5.9}$$

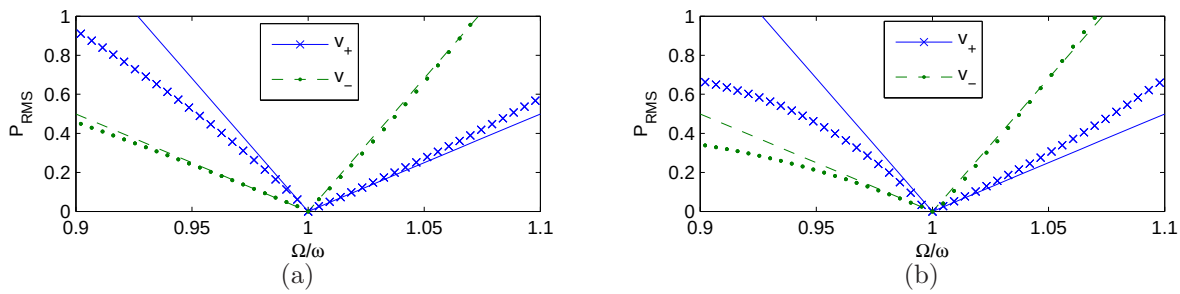

Figure 5.3: Arnold tongues for minimum energy waveforms for frequency increase (v_+) and decrease (v_-) of the Hodgkin-Huxley oscillator. Theoretical boundaries predicted by phase reduction theory are shown as lines, and values computed using 5.3(a) the Hodgkin-Huxley PRC and 5.3(b) the Hodgkin-Huxley equations are shown as points. These values are computed using a line search over the RMS forcing energy, and 5.3(a) closely approximates 5.3(b).

which we substitute into the constraint (5.7) and solve for the multiplier, $\lambda = -2\Delta\omega/\langle Z^2\rangle$. Consequently the minimum energy controls are

$$\begin{aligned} v_+(\theta) &= -\frac{\Delta\omega}{\langle Z^2\rangle} Z(\theta+\varphi_+) \qquad \text{if} \quad \Omega > \omega, \\ v_-(\theta) &= -\frac{\Delta\omega}{\langle Z^2\rangle} Z(\theta+\varphi_-) \qquad \text{if} \quad \Omega < \omega. \end{aligned} \tag{5.10}$$

In practice we omit the phase ambiguity φ_+ or φ_- in the solution (5.10) because entrainment is asymptotic. The minimum energy input that entrains (4.2) to a frequency Ω in the neighborhood of its natural frequency ω is given by (5.10) where $\theta = \Omega t$. A useful way to characterize the limits on control design using phase models is to examine the boundaries of the theoretical Arnold tongues for the controls v_+ and v_-, as well as computed values of the RMS forcing energy required to entrain the Hodgkin-Huxley system using these controls, which are shown in Figure 5.3.

In this section, we have shown that the minimum energy periodic control $u(t) = v(\theta)$ that entrains a single oscillator with natural frequency ω to a target frequency Ω is a re-scaling of the PRC, where $\theta = \Omega t$ is the forcing phase [236, 238]. Observe that this control will entrain oscillators with natural frequencies between ω and Ω to the target Ω as well.

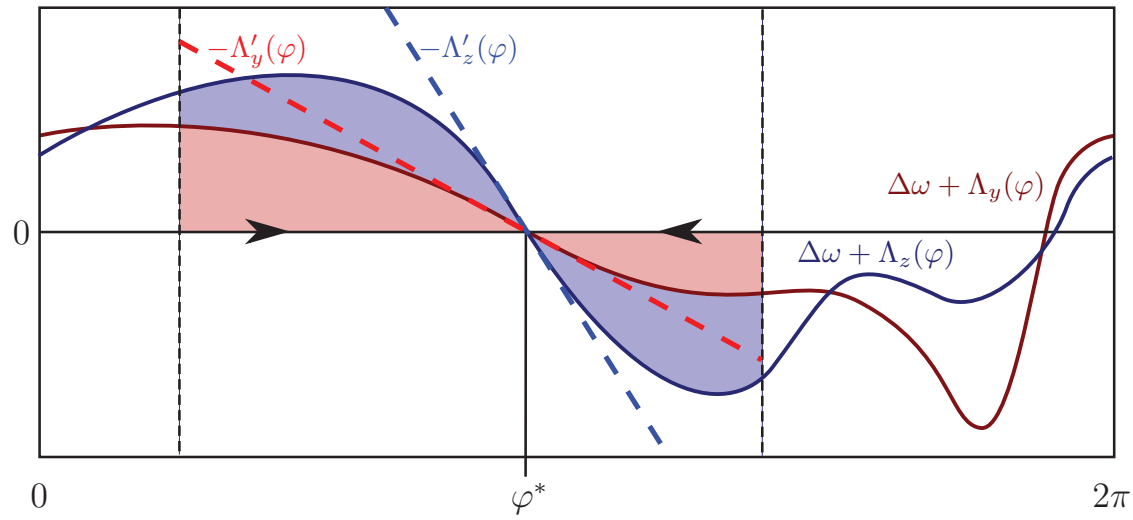

Figure 5.4: Illustration to explain the objective function for fast entrainment. The averaged equation (5.31) is shown for two control waveforms y (red) and z (blue) that both result in the same attractive fixed phase φ^*. Observe that $-\frac{\mathrm{d}}{\mathrm{d}\varphi}\Lambda_z(\varphi^*) > -\frac{\mathrm{d}}{\mathrm{d}\varphi}\Lambda_y(\varphi^*)$, as indicated by the dashed lines. As a result, $|\dot{\varphi}|$ is greater in the phase region between the dashed lines for the waveform z, as indicated by the shaded regions, so that the system converges to φ^* faster when forced using z. Therefore, we maximize the objective $\mathcal{J}[v] = -\frac{\mathrm{d}}{\mathrm{d}\varphi}\Lambda_v(\varphi^*)$ for fast entrainment in problem (5.11).

5.3 Fast Entrainment

An alternative essential objective to minimizing input energy is to minimize the time to entrainment at a given forcing signal energy, in order to establish a fixed phase relationship between the system and forcing signal as soon as possible after the forcing is applied [84]. This notion of fast entrainment can also be used to minimize the time required to re-establish entrainment after interruptions caused by disturbances [96]. This problem is of particular interest to researchers in circadian biology who are interested in optimal protocols for rapidly correcting circadian misalignment [198].

In this section, an asymptotically optimal waveform is derived to maximizes the average rate of entrainment for general weakly forced nonlinear oscillators [235]. The rate of entrainment is characterized by the coefficient of exponential decay in the phase difference between the system and forcing signal. We present a theory by which the entrainment time scale is minimized for a specified forcing energy, where the optimal waveform is a sum of the PRC and its derivative with weights that depend on the difference between the natural and forcing frequencies. These findings can be applied to weakly nonlinear oscillators just past the Hopf

bifurcation, as well as strongly nonlinear relaxation oscillators. We confirm our results with numerical simulations using the Hodgkin-Huxley model, as well as in experiments on the oscillatory chemical reaction arising through the electrodissolution of nickel in sulfuric acid, which is described in Appendix A.4.

Our goal here is to entrain the system (4.2) to a target frequency Ω as quickly as possible by using a periodic control v of fixed power $P = \langle v^2 \rangle$. Ideally, the interaction function would be of a piecewise-constant form, so that the averaged slow phase φ converges to a fixed point φ_* at a uniform rate from any initial value. However, the discontinuity as $\varphi \to \varphi_*$ would result in a singularity in the control v, making it infeasible in practice. An alternative is to maximize $|\dot{\varphi}_*|$, the rate of convergence of the averaged slow phase in the neighborhood of its attractive fixed point φ_*. The calculus of variations can then be used to obtain a smooth optimal candidate solution that also performs well in practice. When the system (5.5) is entrained by a control v, there exists an attractive fixed point φ_* satisfying $\Lambda_v(\varphi_*) + \Delta\omega = 0$ and $\Lambda_v'(\varphi_*) < 0$, where $'$ is the differentiation operator, as illustrated in Figure 5.4.

In order to maximize the rate of entrainment in a neighborhood of φ_* using a control of power P, the value of $|\dot{\varphi}|$ should be maximized for values of φ near φ_*, which occurs when $-\Lambda_v'(\varphi_*)$ is large. This results in the following problem formulation for fast entrainment:

$$\max_{v \in \mathcal{P}} \quad \mathcal{J}[v] = -\Lambda_v'(\varphi_*) \tag{5.11}$$

$$\text{s.t.} \quad \left\langle v^2 \right\rangle = P \tag{5.12}$$

$$\Lambda_v(\varphi_*) + \Delta\omega = 0. \tag{5.13}$$

The constraints can be adjoined to the objective using multipliers λ and μ to yield

$$\begin{aligned}
\mathcal{J}[v] &= -\Lambda_v'(\varphi_*) + \lambda(\left\langle v^2 \right\rangle - P) + \mu(\Lambda_v(\varphi_*) + \Delta\omega) \\
&= -\langle Z'(\theta + \varphi_*) v(\theta) \rangle + \lambda(\left\langle v^2 \right\rangle - P) + \mu(\langle Z(\theta + \varphi_*) v(\theta) \rangle + \Delta\omega) \\
&= \frac{1}{2\pi} \int_0^{2\pi} \big(v(\theta)[\mu Z(\theta + \varphi_*) - Z'(\theta + \varphi_*) + \lambda v(\theta)] - \lambda P + \mu\Delta\omega \big) \mathrm{d}\theta.
\end{aligned} \tag{5.14}$$

The associated Euler-Lagrange equation is

$$\mu Z(\theta + \varphi_*) - Z'(\theta + \varphi_*) + 2\lambda v(\theta) = 0, \tag{5.15}$$

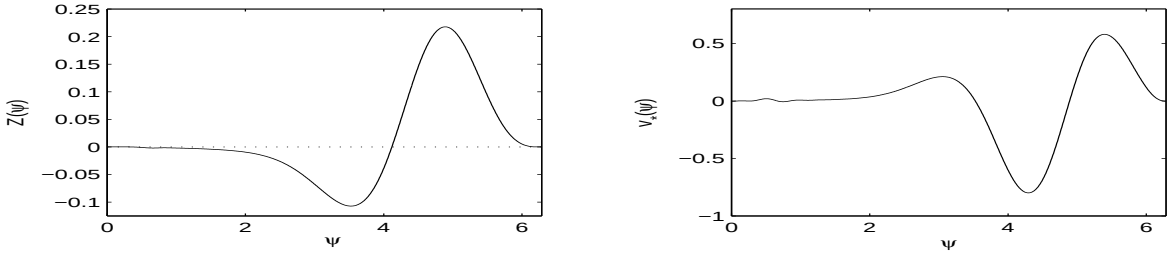

(a) (b)

Figure 5.5: (a) PRC of the HH model; (b) Optimal fast entrainment waveform v for HH system at $\Omega = \omega$ and $P = 0.1$ mW.

and solving for v yields the candidate solution

$$v(\theta) = \frac{1}{2\lambda}[Z'(\theta + \varphi_*) - \mu Z(\theta + \varphi_*)]. \tag{5.16}$$

The multipliers λ and μ can be found by substituting (5.16) into the constraints (5.12) and (5.13). This yields the equations

$$\frac{1}{4\lambda^2}\big[\langle (Z')^2\rangle - 2\mu\langle Z'Z\rangle + \mu^2\langle Z^2\rangle\big] = P, \tag{5.17}$$

$$\frac{1}{2\lambda}\big[\langle Z'Z\rangle - \mu\langle Z^2\rangle\big] = -\Delta\omega. \tag{5.18}$$

Because Z is 2π-periodic, one can show, e.g., using Fourier series, that $\langle Z'Z\rangle = 0$, so that (5.18) easily yields $\mu = 2\Delta\omega\lambda/\langle Z^2\rangle$. Substituting this result into (5.17) leads to a quadratic equation (5.17) for λ. Now, by substituting (5.16) into $\Lambda'(\varphi_*) = \langle Z(\theta + \varphi_*)v(\theta)\rangle$ we obtain $\Lambda'(\varphi_*) = \langle (Z')^2\rangle/(2\lambda)$, so we choose $\lambda < 0$ when solving (5.17) for λ in order to maximize the objective in (5.11). Thus the optimal waveform and multiplier simplify to

$$v(\theta) = \frac{Z'(\theta)}{2\lambda} - \frac{\Delta\omega Z(\theta)}{\langle Z^2\rangle}, \quad \lambda = -\frac{1}{2}\sqrt{\frac{\langle (Z')^2\rangle}{P - \frac{(\Delta\omega)^2}{\langle Z^2\rangle}}}, \tag{5.19}$$

where we disregard the phase shift φ_*, because the entrainment process is asymptotic. For zero frequency detuning, the optimal waveform is a re-scaling of the derivative Z' of the PRC. As $|\Delta\omega|$ increases, v continuously transforms towards Z, which is the minimum energy waveform for frequency control [236]. This transition reflects the conceptual trade-off between the fast entrainment objective (5.11) and frequency control constraint (5.13), which can be satisfied only when $P > (\Delta\omega)^2/\langle Z^2\rangle$.

The proposed technique for constructing optimal fast entrainment waveforms can be applied to any nonlinear oscillator, and requires no knowledge about its initial state. Entrainment is achieved over the minimum number of cycles possible for a given control energy such that phase model approximation and averaging remain valid. The conditions required for such approximations to be appropriate for entrainment have been explored in previous work [56, 238]. When the initial slow phase of the system is far from a stable fixed point, several cycles may be required for convergence to the phase-locked state to be realized, and this occurs least on average for the optimal waveform. In contrast to previous studies on the control of oscillators using phase models [26, 157, 95, 56, 46, 236], the derivative of the phase response curve (PRC) plays an important role in addition to the PRC itself. The methodology is promising for fast re-establishment of entrainment in oscillators that intermittently break phase locking due to environmental or internal effects, such as biological systems with fluctuations in chemical reaction rates due to the small number of molecules in a cell [5]. Finally, observe that our methodology is suitable for weak phase resetting, while strong resetting requires control approaches that do not depend on averaging but involve substantial changes to the state of the oscillator. In the following section, we present computational simulations and experimental results that support our findings.

5.3.1 Fast Entrainment Experiments

Consider a system with a sinusoidal PRC, given by $Z(\theta) = a\sin(\theta)$. Using angle sum identities and the fact that in this case $\langle (Z')^2 \rangle = \langle Z^2 \rangle$, one can show that v is of form $v(\theta) = P\sin(\theta)$. Indeed, for the case of a sinusoidal PRC, a sinusoidal input optimizes the minimum energy [236] and rapid phase-locking objectives simultaneously. However, the utility of our approach is most evident for oscillating systems with complex dynamics, in particular those that exhibit relaxation, and hence higher harmonics in the PRC. As an example, consider the Hodgkin-Huxley (HH) system [99], which is a fundamental model used in the study of neural dynamics [238]. When the baseline current I_b injected into the axon is sufficiently high, the voltage V spikes repeatedly. Our goal is to modulate the additional injected current $I(t)$ to entrain the spiking frequency to a desired target Ω in as short a time as possible. We first reduce the HH system to a phase model as in (4.2) where $u = I(t)$, where $\omega \approx 0.429$ rad/sec, and the PRC Z is given in Figure 5.5(a). After selecting the control power P and the target frequency Ω, we use (5.19) to compute the

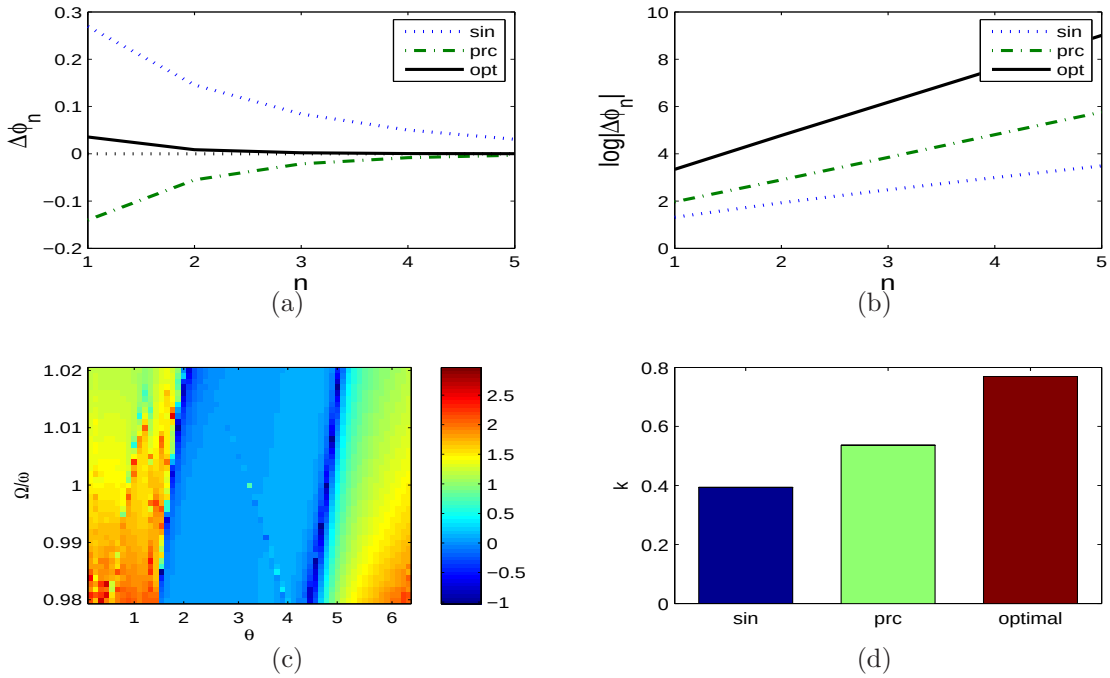

Figure 5.6: Simulations with the HH model: (a) Convergence of phase difference $\Delta\varphi_n$ between inter-spike intervals; (b) Exponential fit for k when $\Omega = 1.01\omega$ and $P = 0.5$. The k-values are 0.5415, 0.9510, and 1.4139 for sine, PRC, and optimal waveforms, respectively. (c) Initial convergence rates k (in color) for 5 cycles with $\Omega \in [0.98\omega, 1.02\omega]$ and $\theta(0) \in [0, 2\pi]$ when using the optimal waveform. (d) Average initial k on $(\Omega, \theta(0)) \in [0.98\omega, 1.02\omega] \times [0, 2\pi]$ for sine, PRC, and optimal waveforms is 0.3933, 0.5365, and 0.7691, resp. Initial divergence takes place in 7.69%, 12.73%, and 6.04% of initial conditions for sine, PRC, and optimal waveforms, respectively.

optimal waveform v, which is shown in Figure 5.5(b). Numerically, we use the Fourier series coefficients of Z to evaluate expressions derived from the PRC, such as Z', $\langle Z^2 \rangle$, and so on. In this computational example, we focus on initial convergence rates for fast entrainment, which can be quantified by the rate k at which the phase difference between successive inter-spike intervals converges exponentially to zero, according to $\Delta\varphi_n = e^{-kn}$, as shown in Figure 5.6. The optimal waveform (5.19) achieves a significantly greater average rate k for all values of Ω and initial states on Γ.

The experimental utility of the phase model technique for fast entrainment is demonstrated by manipulating an oscillatory chemical process [136, 235]. The process was produced using a standard three-electrode setup that consisted of a 1 mm diameter nickel working, a $Hg/Hg_2SO_4/(sat)K_2SO_4$ reference, and a Pt coated Ti rod counter electrode immersed in 3 mol/L sulfuric acid solution at 10 ^{o}C. The nickel working electrode was polarized with a

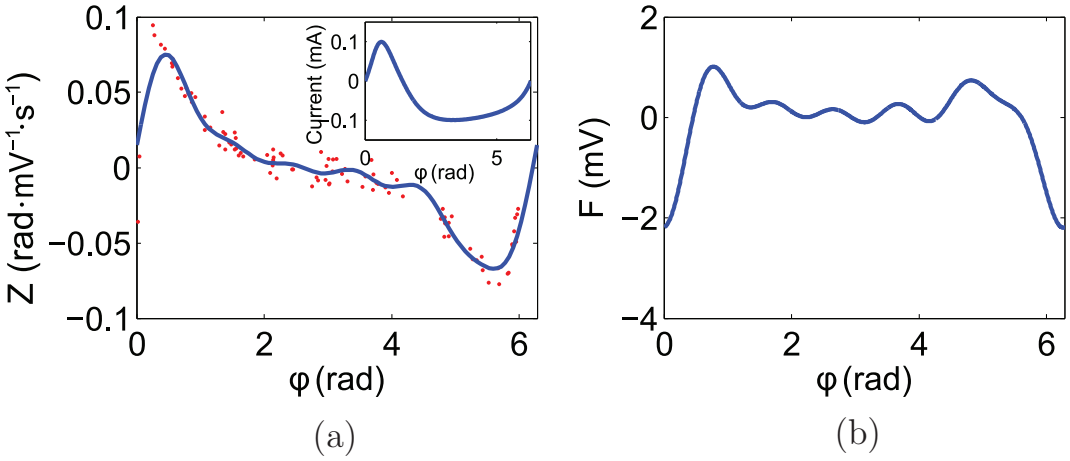

(a) (b)

Figure 5.7: Electrodissolution experiments: (a) PRC and current waveform (inset) of the electrochemical oscillations. The PRC is measured by stimulating the system using a sequence of pulses (A=200mV magnitude and τ =0.05 s pulsewidth) and measuring the corresponding phase shift (Φ) as a function of the phase; $Z = \Phi/(A\tau)$ rad/mV/s measurements (dots) and Fourier fit with 5 harmonics (curve). (b) Optimal waveform using (5.19) with $\Omega = \omega$, $P = 0.5$, and the PRC in (a).

potentiostat (Gamry Instruments, Reference 600) at a circuit potential $V = V_0 + AF(\theta)$, where A and F are the forcing amplitude and waveform, respectively, and V_0 is the base potential. Each forcing waveform F has power $P = 0.5$. The current, proportional to the dissolution rate, was measured by the potentiostat at a rate of 200 Hz. When 1 kOhm resistance was attached to the nickel wire, nonlinear current oscillations with a period of 2.11 s were obtained at $V_0 = 1.15$ V as shown in the inset of Figure 5.7. In each instance of the experiment, the PRC, such as the example in Figure 5.7a, was obtained using the pulse perturbation method [95, 122]. The phase of the oscillation was obtained using the linear interpolation technique [178] by setting the phase of the n-th current peak to $2\pi n$. The transformation of the PRC as the circuit potential increases has been previously analyzed in detail [122].

Using (5.19), an optimal fast entrainment waveform was constructed for equal forcing and natural frequencies, $\Omega = \omega$, in order to remove the effect of the frequency control constraint (5.13). When the optimal waveform with amplitude of $A = 12.5$ mV was applied to entrain the free-running chemical oscillator, the phase difference between the current oscillations and the forcing signal, shown in Figure 5.8a, monotonically decreased until a final phase difference of $\phi_f = 5.51$ rad was attained after 30 seconds.

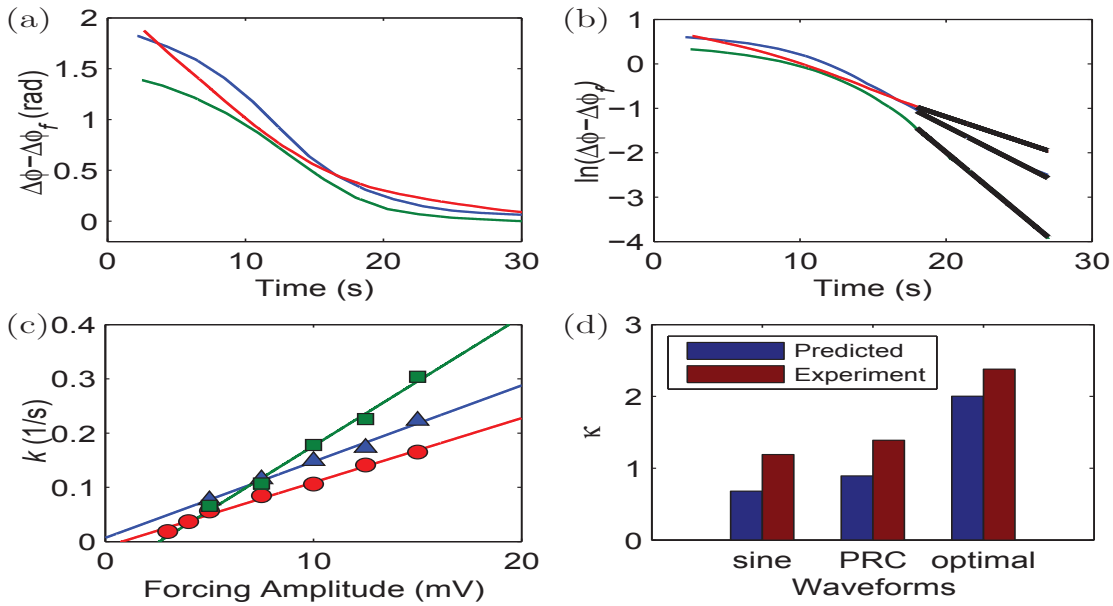

Figure 5.8: Electrodissolution experiments: (a) Phase difference $\Delta\phi(t)$ for sine (dashed), PRC (thin), and optimal (thick) forcing at $A = 12.5$ mV. (b) Semilog plot of $\Delta\phi(t)$ from (a). For $t > 20$ seconds after forcing is applied, $\Delta\phi(t)$ decays exponentially to zero. Rates of entrainment (slope of the linear fits): $k(\text{sin}) = 0.1093\ s^{-1}$, $k(Z) = 0.167\ s^{-1}$, $k(\text{optimal}) = 0.243\ s^{-1}$. (c) Rate of entrainment as a function of forcing amplitude for sin (○), PRC (△), and optimal (□) forcing. The slopes κ in $s^{-1}\text{mV}^{-1}$ of the fitted lines characterize the performance of the waveforms for fast entrainment. (d) Normalized entrainment rates predicted from PRC estimates (blue: $\kappa(\text{sin})$=0.68, $\kappa(PRC)$=0.89, $\kappa(\text{optimal})$=2.00) and measured experimentally (red: $\kappa(\text{sin})$=1.19, $\kappa(PRC)$=1.39, $\kappa(\text{optimal})$=2.38) are highest for the optimal waveform.

The behavior of the phase difference $\Delta\phi(t) = \phi(t) - \phi_f$ after 20 seconds can be closely described by an exponential decay $\ln[\Delta\phi(t)/\Delta\phi(0)] = -kt$, which is shown in Figure 5.8b, with a rate of entrainment $k = 0.243\ s^{-1}$ for the optimal waveform. This rate was found to be lower for other waveforms such as sine and the PRC Z itself, as shown in Figures 5.8a and 5.8b. To compensate for measurement errors and data processing inaccuracies, we measured the rate k at 7 amplitudes A between 2.5 and 15 mV. The slopes κ of the k vs. A plots in Figure 5.8c correspond to $-\Lambda_v'(\varphi_*)$ for normalized PRC and v, and are compared, along with values predicted using the estimated PRC for each experiment, in Figure 5.8d. The optimal waveform performs significantly better.

5.4 Subharmonic Entrainment

Previous work on optimal control of the entrainment process has focused on the harmonic case, which corresponds to a one-to-one (1:1) relationship between the frequencies of the stimulus and oscillator. Many physical processes, however, undergo subharmonic N:M entrainment, which transpires when N cycles of the stimulus occur for every M cycles of the oscillator [77]. Originally examined in the context of loudspeaker dynamics [40], subharmonic synchronization can emerge among weakly coupled oscillators [61, 87], and can be induced in forced or injection-locked oscillators to produce entrainment [43, 208]. Subharmonic locking phenomena are of interest in a wide range of fields, and neuroscience in particular. Applications exist in magnetoencephalography [212], the study of brain connectivity [102], dynamic neural regulation [108], as well as in the clinical treatment of epilepsy [101, 118, 129]. Subharmonic entrainment plays a central role in our understanding of human perception of beat and meter [134, 36, 168], as well as sound in general, and an ability to affect this phenomenon will lead to innovative therapies for tinnitus [209, 215]. Indeed, the functional connectivity of the cerebral cortex may be shaped by mutual entrainment of bursting neurons across multiple time scales in a coevolutionary manner [102, 133, 88]. Previous studies have found that subharmonic synchronization phenomena are ubiquitous in biological systems. In fact, respiration and heartbeat in human beings is typically entrained at a 1:4 ratio [194], and evidence exists that human sleep latency is entrained by the lunar cycle [29, 69], which is a 1:28 ratio. Other investigations have focused on engineering subharmonic locking in electronic circuits [148, 211], antenna systems [231], and voice coil audio systems [24, 167]. In this section, a method is derived for engineering weak, periodic signals that achieve subharmonic entrainment in nonlinear oscillating systems without the use of state feedback.

5.4.1 Theory of subharmonic entrainment by weak forcing

The following derivation parallels the content of Section 5.1. The goal is to entrain the system (4.2) to a target frequency Ω using a periodic forcing control $u(t)$ of frequency Ω_f, such that M cycles of the oscillator occur for every N cycles of the input. When such N:M entrainment occurs, then the target and forcing frequencies satisfy $M\Omega_f = N\Omega$, so that the control input has the form $u(t) = v(\frac{N}{M}\Omega t)$, where v is 2π-periodic. From here on, it is assumed that N and M are coprime integers. As in Section 5.1, the weak forcing assumption

is used, and a slow phase variable is defined by $\phi(t) = \psi(t) - \Omega t$, and $\Delta\omega = \omega - \Omega$ is again the frequency detuning between the natural and target frequencies. The dynamic equation for the slow phase is then

$$\dot{\phi} = \dot{\psi} - \Omega = \Delta\omega + Z(\Omega t + \phi)v\left(\frac{N}{M}\Omega t\right), \tag{5.20}$$

where $\dot{\phi}$ is called the phase drift. Here the forcing phase is $\eta = \Omega_f t = \frac{N}{M}\Omega t$, and a change of variables $\theta = \eta/N$ is made. Then the weak ergodic theorem for measure-preserving dynamical systems on the torus [127] implies that for any periodic function v, the interaction function

$$\begin{aligned}\Lambda_v^{NM}(\phi) &\triangleq \langle Z(M\theta + \phi)v(N\theta)\rangle \\ &= \frac{1}{2\pi}\int_0^{2\pi} Z(M\theta + \phi)v(N\theta)\mathrm{d}\theta \\ &= \lim_{T\to\infty}\frac{1}{T}\int_0^T Z(\Omega t + \phi)v\left(\frac{N}{M}\Omega t\right)\mathrm{d}t \end{aligned} \tag{5.21}$$

exists as a continuous, 2π-periodic function in $\mathcal{P}$. In addition, because both Z and v are 2π-periodic, Λ_v^{NM} can be expressed by integrating with respect to η or to $\xi = M\theta = \Omega t$ to yield two equivalent expressions given by

$$\begin{aligned}\Lambda_v^{NM}(\phi) &= \frac{1}{2\pi N}\int_0^{2\pi N} Z\left(\frac{M}{N}\eta + \phi\right)v(\eta)\mathrm{d}\eta \\ &= \frac{1}{2\pi N}\sum_{j=0}^{N-1}\int_0^{2\pi} Z\left(\frac{M}{N}[2\pi j + \eta] + \phi\right)v(\eta)\mathrm{d}\eta, \end{aligned} \tag{5.22}$$

$$\begin{aligned}\Lambda_v^{NM}(\phi) &= \frac{1}{2\pi M}\int_0^{2\pi M} Z(\xi + \phi)v\left(\frac{N}{M}\xi\right)\mathrm{d}\xi \\ &= \frac{1}{2\pi M}\sum_{\ell=0}^{M-1}\int_0^{2\pi} Z(\xi + \phi)v\left(\frac{N}{M}[2\pi\ell + \xi]\right)\mathrm{d}\xi. \end{aligned} \tag{5.23}$$

In particular, the expression (5.22) can be written as

$$\Lambda_v^{NM}(\phi) = \langle Y^{NM}(\eta, \phi)v(\eta)\rangle \tag{5.24}$$

where we define the function

$$Y^{NM}(\eta,\phi) = \frac{1}{N}\sum_{j=0}^{N-1} Z\bigg(\frac{M}{N}[2\pi j+\eta]+\phi\bigg). \tag{5.25}$$

We henceforth write $Y^{NM}(\eta) \triangleq Y^{NM}(\eta,0)$. At this point, let us establish several important expressions that will be used throughout the following sections. First, we define a function Q as the 1:1 interaction function of Z with itself by

$$Q(\phi) \triangleq \langle Z(\theta+\phi)Z(\theta)\rangle. \tag{5.26}$$

By defining an inner product $(\cdot,\cdot):\mathcal{P}\times\mathcal{P}\to\mathbb{R}$ by $(f,g)=\langle fg\rangle$, the Cauchy-Schwarz inequality yields $|Q(\phi)|\leq\langle Z^2\rangle = Q(0)$, and the periodicity of Z results in $Q(\phi)=\langle Z(\theta+\phi)Z(\theta)\rangle = \langle Z(\theta)Z(\theta-\phi)\rangle = Q(-\phi)$. We can then define

$$V^{NM}(\phi) \triangleq \frac{1}{N}\sum_{j=0}^{N-1} Q\bigg(\frac{M}{N}2\pi j+\phi\bigg), \tag{5.27}$$

which inherits the properties $|V^{NM}(\varphi)|\leq V^{NM}(0)$ for all $\varphi\in[0,2\pi)$ and $V^{NM}(-\varphi) = V^{NM}(\varphi)$ from the properties of Q. We will subsequently write $V_0^{NM}\triangleq V^{NM}(0)$ and $V_*^{NM} = \min_{\phi\in[0,2\pi]} V^{NM}(\phi)$. The expression (5.27) is important because using $v(\theta)=Y^{NM}(\theta,\psi)$ in (5.23) yields

$$\begin{aligned}
\Lambda^{NM}_{Y^{NM}(\theta,\psi)}(\phi) &= \frac{1}{2\pi M}\sum_{\ell=0}^{M-1}\int_0^{2\pi} Z(\xi+\phi)Y^{NM}\bigg(\frac{N}{M}[2\pi\ell+\xi],\psi\bigg)\mathrm{d}\xi \\
&= \frac{1}{2\pi N}\sum_{j=0}^{N-1}\int_0^{2\pi} Z(\xi+\phi)Z\bigg(\xi+\frac{M}{N}2\pi j+\psi\bigg)\mathrm{d}\xi \\
&= \frac{1}{N}\sum_{j=0}^{N-1} Q\bigg(\frac{M}{N}2\pi j+\phi-\psi\bigg) = V^{NM}(\phi-\psi).
\end{aligned} \tag{5.28}$$

In addition, using (5.24) we see that the energy of the function Y^{NM} is given by

$$\langle Y^{NM}Y^{NM}\rangle = \Lambda^{NM}_{Y^{NM}}(0) = V_0^{NM}. \tag{5.29}$$

The functions Y^{NM}, Q, and V^{NM}, as defined in (5.25), (5.26), and (5.27), respectively, will appear repeatedly in the subsequent derivations of optimal subharmonic entrainment controls.

As in the case of 1:1 entrainment, the formal averaging theorem [104] permits us to approximate (5.20) by the averaged system

$$\dot{\varphi} = \Delta\omega + \Lambda_v^{NM}(\varphi) + \mathcal{O}(\varepsilon^2) \tag{5.30}$$

in the sense that there exists a change of variables $\varphi = \phi + \varepsilon h(\varphi, \phi)$ that maps solutions of (5.20) to those of (5.30). A detailed derivation for the 1:1 case is given in Section 5.1.1, and this can be easily extended to the N:M case. Therefore the weak forcing assumption the phase drift equation to be approximated by

$$\dot{\varphi} = \Delta\omega + \Lambda_v^{NM}(\varphi). \tag{5.31}$$

The averaged equation (5.5) is autonomous, and approximately characterizes the asymptotic behavior of the system (4.2) under periodic forcing. Specifically, we say that the system is entrained by a control $u = v(\Omega_f t)$ when the phase drift equation (5.31) satisfies $\dot{\varphi} = 0$, which will occur as $t \to \infty$ if there exists a phase φ_* that satisfies $\Delta\omega + \Lambda_v^{NM}(\varphi^*) = 0$. When both the control waveform v and PRC Z are non-zero, the function $\Lambda_v^{NM}(\varphi)$ is not identically zero, so when the system is entrained there exists at least one $\varphi_* \in [0, 2\pi)$ that is an attractive fixed point of (5.31). The stable fixed points $\{\varphi_i^*\}$ of (5.31), which are the roots of the equation $\Delta\omega + \Lambda_v^{NM}(\varphi) = 0$, determine the average phase shift, relative to $\Omega_f t$, at which the oscillation stabilizes from a given initial phase. As before, we define the phases $\varphi^+ = \arg\max_\varphi \Lambda_v^{NM}(\varphi)$ and $\varphi^- = \arg\min_\varphi \Lambda_v^{NM}(\varphi)$, so for at least one stable fixed point of Λ_v^{NM} to exist and entrainment to occur, $-\Lambda_v^{NM}(\varphi^+) \leq \Delta\omega \leq -\Lambda_v^{NM}(\varphi^-)$ must hold. Thus the range of the interaction function determines which values of the frequency detuning $\Delta\omega$ yield phase locking. These properties are illustrated in Figure 5.1 for the 1:1 case, which also illustrates an N:M interaction function if Λ_v is replaced with Λ_v^{NM}.

As in the 1:1 case, the interaction function can be used to estimate the values of the minimum root mean square (RMS) energy $P_v^{NM}(\Omega_f) = \sqrt{\langle v^2 \rangle}$ that results in locking of an oscillator to a given frequency Ω_f at a subharmonic N:M ratio using the waveform v. Parallel to the derivation in Section 5.1.2, this is accomplished by substituting the expression $v(\theta) = P_v^{NM}(\Omega_f)\widetilde{v}(\theta)$ and the relation $\Omega_f = \frac{N}{M}\Omega$ into the equation $\Delta\omega + \Lambda_v^{NM}(\varphi) = 0$ and simplifying

to obtain

$$\omega - \frac{M}{N}\Omega_f + P_v^{NM}(\Omega_f) \cdot \Lambda_{\widetilde{v}}^{NM}(\varphi) = 0, \tag{5.32}$$

where $\widetilde{v}$ is a unit energy normalization of v. This equation is then solved for $P_v^{NM}(\Omega_f)$ at $\varphi = \varphi^+$ and $\varphi = \varphi^-$ to produce the Arnold tongues, as described in Table 5.1. Based on the theoretical foundation and fundamental notations presented in this section, we proceed to formulate and solve optimization problems for subharmonic entrainment of an oscillator. In the following section, we address the canonical problem of establishing subharmonic resonance of a single oscillator to a periodic input of minimum energy at a desired frequency.

5.4.2 Minimum energy subharmonic entrainment of an oscillator

The subharmonic entrainment of an oscillator by using a control of minimum energy can be formulated as a variational optimization problem that generalizes the problem solved in Section 5.2. The objective function to be minimized is the control energy $\langle v^2 \rangle$, and the design constraint is $\omega + \Lambda_v^{NM}(\varphi^+) \geq \Omega$ if $\Omega > \omega$ and $\omega + \Lambda_v^{NM}(\varphi^-) \leq \Omega$ if $\Omega < \omega$. This inequality is active when optimal entrainment occurs, and hence can be expressed as the equality constraint

$$\Delta\omega + \Lambda_v^{NM}(\varphi^+) = 0 \quad \text{if} \quad \Omega > \omega, \tag{5.33}$$

$$\Delta\omega + \Lambda_v^{NM}(\varphi^-) = 0 \quad \text{if} \quad \Omega < \omega. \tag{5.34}$$

We formulate the problem for $\Omega > \omega$ to obtain the minimum energy control for frequency increase v_+ using the calculus of variations [74]. The derivation of the case where $\Omega < \omega$ is similar, and results in the symmetric control v_-. The constraint (5.33) can be adjoined to the cost $\langle v^2 \rangle$ using a multiplier λ, leading to the objective

$$\begin{aligned} \mathcal{J}[v] &= \left\langle v^2 \right\rangle - \lambda(\Delta\omega + \Lambda_v^{NM}(\varphi^+)) \\ &= \left\langle v^2 \right\rangle - \lambda\Delta\omega - \frac{\lambda}{2\pi}\int_0^{2\pi} Y^{NM}(\eta, \varphi^+) v(\eta) \mathrm{d}\eta \\ &= \frac{1}{2\pi}\int_0^{2\pi} \big(v(\eta)\big[v(\eta) - \lambda Y^{NM}(\eta, \varphi^+)\big] - \lambda\Delta\omega\big)\mathrm{d}\eta, \end{aligned} \tag{5.35}$$

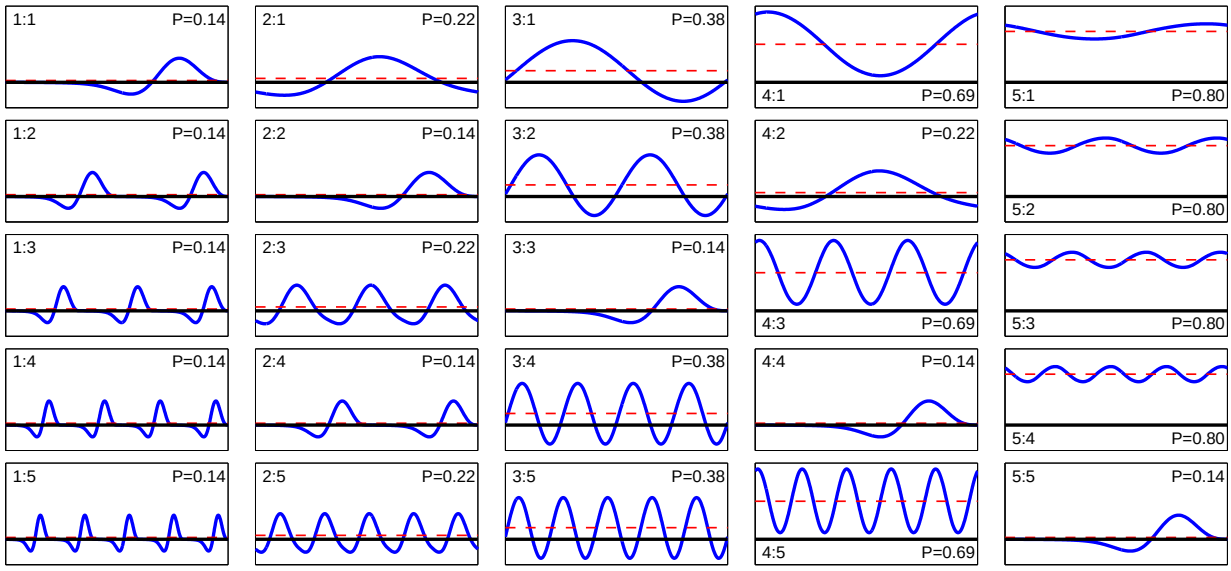

Figure 5.9: Minimum energy subharmonic entrainment controls v_+ for increasing the frequency of the Hodgkin-Huxley neuron model by 3%. The controls for N, $M = 1, \ldots, 5$ are shown, and the domain and range in each plot are $[0, 2\pi]$ and $[-.4, 1.2]$, respectively. The black line indicates the x-axis, and the red dashed line is the average value of the control. The subharmonic ratio and RMS control power are indicated. Observe that if $N = 1$, the control is simply repeated M times to effectively produce 1:1 entrainment, which requires the lowest energy. As N grows large for a fixed M, the controls converge to a constant Υ given in equation (5.40).

where the expression (5.24) is substituted for Λ_v^{NM}. Applying the Euler-Lagrange equation [74], we obtain the necessary condition for a candidate optimal solution

$$v_m(\eta) = \frac{\lambda}{2} Y^{NM}(\eta, \varphi^+). \tag{5.36}$$

Recalling (5.28), we obtain

$$\Lambda_{v_m}^{NM}(\varphi) = \frac{\lambda}{2} \Lambda_{Y^{NM}(\theta,\varphi^+)}^{NM}(\phi) = \frac{\lambda}{2} V^{NM}(\varphi - \varphi^+). \tag{5.37}$$

Therefore the constraint (5.33) results in

$$0 = \Delta\omega + \Lambda_{v_m}^{NM}(\varphi^+) = \Delta\omega + \frac{\lambda}{2} V_0^{NM}, \tag{5.38}$$

so the multiplier is given by $\lambda = -2\Delta\omega / V_0^{NM}$. Consequently, we can express the minimum-energy control that entrains the system (4.2) to a target frequency Ω using a periodic forcing

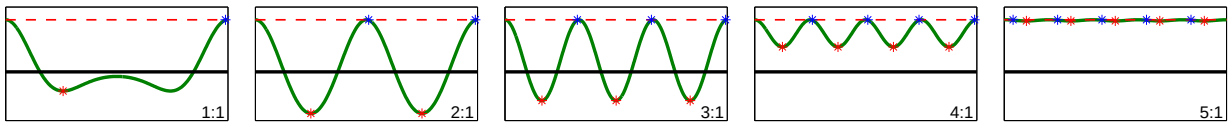

Figure 5.10: Interaction functions Λ_v^{NM} for minimum energy subharmonic entrainment controls v_+ for increasing the frequency of the Hodgkin-Huxley neuron model by 3%, where the domain and range in each plot are $[0, 2\pi]$ and $[-0.012, 0.016]$, respectively. Interaction functions for subharmonic entrainment depend only on N. The black line indicates the x-axis, and the red dashed line is placed at $\Lambda_{v_+}^{NM}(\varphi^+)$, which is equal to the frequency detuning $\Delta\omega = \omega - \Omega$ by design. As N grows large, the interaction function converges to small variation about $\Delta\omega$. Red and blue stars mark the phases $\{\varphi_i^-\}$ and stable fixed points $\{\varphi_i^*\}$ of (5.31), each of which occur N times.

control $u(t) = v(\Omega_f t)$, where v is 2π-periodic and $\Omega_f = \frac{N}{M}\Omega$, as

$$v_m(\eta) = \begin{cases} v_+(\eta) = -\dfrac{\Delta\omega}{V_0^{NM}} \cdot Y^{NM}(\eta, \varphi^+) & \text{if} \quad \Omega > \omega, \\ \\ v_-(\eta) = -\dfrac{\Delta\omega}{V_0^{NM}} \cdot Y^{NM}(\eta, \varphi^-) & \text{if} \quad \Omega < \omega, \end{cases} \tag{5.39}$$

where $\eta = \Omega_f t$ is the forcing phase. In practice, we may omit the phase ambiguity φ^+ or φ^- in (5.39) because entrainment is asymptotic. The optimal waveforms for minimum-energy entrainment of the Hodgkin-Huxley system are shown in Figure 5.9 for values of N, $M = 1, \ldots, 5$, and the corresponding interaction functions are shown in Figure 5.10. Observe that in Figure 5.9, the 1:M minimum-energy control will repeat the 1:1 optimal waveform M times during the control cycle. As the ratio N/M grows large, the controls converge to a constant given by

$$\Upsilon = -\Delta\omega \cdot \frac{\int_0^{2\pi} Z(\theta)\mathrm{d}\theta}{\int_0^{2\pi} Q(\varphi)\mathrm{d}\varphi}, \tag{5.40}$$

as seen by substituting the limiting expressions as $N \to \infty$ for Y^{NM} and V^{NM} from equations (5.25) and (5.27) into the solution (5.39).

Finally, by invoking (5.29), we see that the minimum energy waveform (5.39) for subharmonic entrainment of a single oscillator has energy given by

$$\langle v_m^2 \rangle = \left(\frac{\Delta\omega}{V_0^{NM}}\right)^2 \langle Y^{NM}(\eta, \varphi^+) Y^{NM}(\eta, \varphi^+) \rangle = \frac{(\Delta\omega)^2}{V_0^{NM}}. \tag{5.41}$$

We have shown that the minimum energy periodic control $u(t) = v(\frac{N}{M}\Omega t)$ that achieves subharmonic entrainment of a single oscillator with natural frequency ω to a target frequency Ω is a re-scaling of the function $Y^{NM}(\eta)$ given in (5.25), where $\eta = \frac{N}{M}\Omega t$ is the forcing phase. In the case that $N = M = 1$, these results reduce to the solution in the harmonic (1:1) case in Section 5.2, which is a re-scaling of the PRC Z [236, 238]. In addition, it is important to note that very similar optimal inputs for altering the frequency of oscillating neural systems in the phase model representation have been obtained using other methods in the harmonic case [157, 46]. The fundamental conclusion is that when the desired change in the frequency of the oscillator is small and the applied input to the system is weak, the optimal control in the harmonic case is a re-scaling of the PRC. Therefore we expect that applying alternative methods [157, 46] to compute inputs for minimum energy subharmonic control of oscillators will also result in solutions similar to (5.39).

The above optimal waveforms are examined in several numerical simulations that validate the theoretical results that have been derived above for minimum-energy subharmonic entrainment. Specifically, we compare the theoretical Arnold tongues for the waveforms that were derived from the phase-reduced Hodgkin-Huxley system with computed Arnold tongues for the phase-reduced and full state-space systems. Because of the periodicity of Z, v, and Λ_v^{NM}, all of these functions are conveniently represented using Fourier series, as described in Appendix B. These representations are used to synthesize optimal waveforms, which are then applied to simulations to test for entrainment of ordinary differential equation systems for phase models and state-space systems. Numerical integrations are performed using the 4th order Runge-Kutta method.

For the waveform v_- as in (5.39), which is used to entrain a single oscillator, the results are shown in Figures 5.11 and 5.12. In this case the natural frequency ω of the oscillator is fixed, and the minimum RMS energy $P_v^{NM}(\Omega_f)$ is obtained as a function of the forcing frequency Ω_f. The theoretical Arnold tongue is computed by using Table 5.1, with Λ_v^{NM} used in stead of Λ_v, while the actual Arnold tongues for the phase-reduced and state-space system are computed by fixing values of Ω_f and using a line search to compute the boundary of the entrainment region. A bisection search is initialized using guesses of .9 and 1.1 times the theoretical estimate of $P_v^{NM}(\Omega_f)$, and is terminated when the upper and lower bound are within 0.01 times that estimate. To determine whether a unit energy waveform $\widetilde{v}$ entrains a phase model (4.2) for a given pair $(\Omega_f, P_{\widetilde{v}}^{NM})$ of forcing frequency and control energy, the control input $u(t) = P_{\widetilde{v}}^{NM} \cdot \widetilde{v}(\Omega_f t)$ is applied to the phase model, which is initialized at a solution of

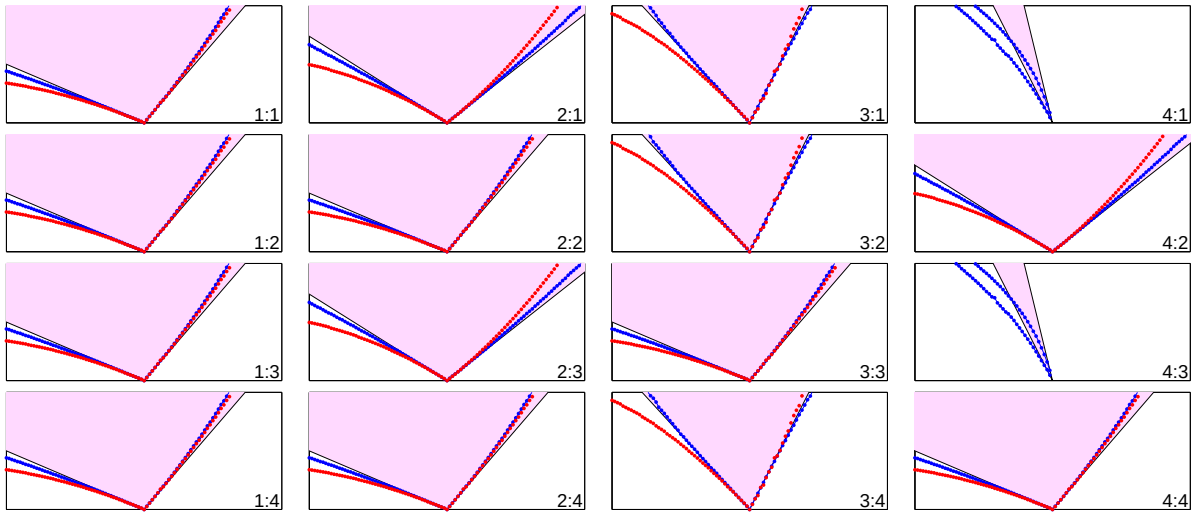

Figure 5.11: Arnold tongues for minimum energy subharmonic entrainment controls v_- for Hodgkin-Huxley neurons, where the target frequency is $\Omega = 0.99\omega$. The domain in each panel is the forcing frequency Ω_f on the interval of 90% to 110% of $\frac{N}{M}\omega$ where ω is the natural frequency, and the range is $[0, 1]$. The entrainment ratio is indicated at the bottom right. The shaded region is the theoretical Arnold tongue as determined by Table 5.1. The actual boundaries of the Arnold tongues are computed as well for entrainment of the phase model, as shown in blue, and for the full state-space model, as shown in red. For the 4:1 and 4:3 cases, the tongues become too narrow to compute for the state-space model.

$\Delta\omega + \Lambda_v^{NM}(\varphi) = 0$, such as φ_1^* in the illustration in Figure 5.1. The system (4.2) is integrated numerically, and then the time-series $\psi_k := \psi(kT_e)$, $k = 1, 2, \ldots$, where $T_e = 2\pi/\Omega$ is the desired period for the entrained system, is examined to check for convergence to a steady state value. Convergence of this time-series implies that the forced system has the desired period T_f. In practice, we check whether ψ_k for $k = 46, \ldots, 50$ remains within an error tolerance of $\epsilon_1 = 10^{-1}$. This approach provides enough time to guarantee that the system has converged to steady-state, in the case that entrainment occurs. Our experiments have shown that this straightforward approach is sufficient to approximate the minimum RMS energy $P_v^{NM}(\Omega_f)$ with error below 1% of the actual value. We extend the same technique to compute Arnold tongues for the full state-space system (4.1) by applying to it the same control, and examining the time-series $y_k := x_1(kT_e)$, $k = 1, 2, \ldots$, where $x_1(t)$ is the first state variable. To obtain a reasonably accurate estimate of the boundary, we accept that convergence has occurred when y_k for $k = 200, \ldots, 250$ remains within an error tolerance of $\epsilon_2 = 10^{-2}$.

The effect of the subharmonic forcing ratio on the entrainment properties of a phase model and given input waveform can be inferred directly from the definition of the interaction function in (5.21). The locking range of a control waveform, and hence the Arnold tongue,

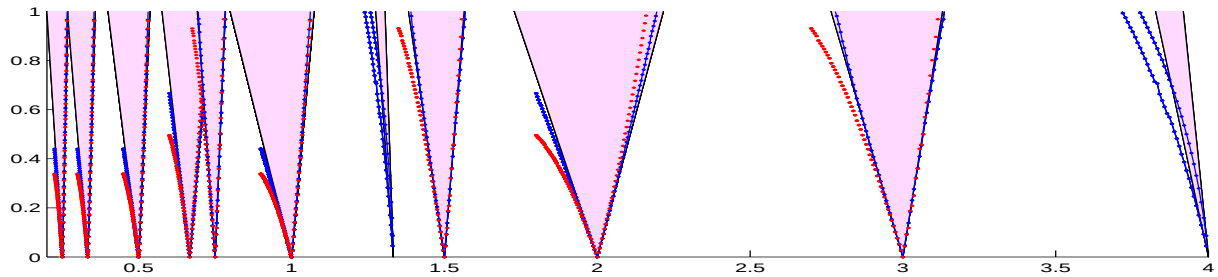

Figure 5.12: Arnold tongues for minimum energy subharmonic entrainment controls v_m for Hodgkin-Huxley neurons, where the target frequency is $\Omega = 0.99\omega$. All of the Arnold tongues in Figure 5.11 are shown together on one plot, where the domain is Ω_f/ω, i.e., the ratio between the forcing and natural frequencies.

depends on the properties of the interaction function, as illustrated in Figure 5.1 and Table 5.1. An examination of the cases where one or both of the PRC and input are sinusoidal is particularly useful. If the PRC is $Z(\theta) = \sin(\theta)$, then it is evident that N:M entrainment is not possible when $N > M$, because the orthogonality of the trigonometric basis functions of the Fourier series would result in $\Lambda_v^{NM}(\varphi) = 0$. Conversely, if the input is $v(\theta) = \sin(\theta)$, then N:M entrainment is not possible when $N < M$ for the same reason. This leads to the lemma regarding the existence of subharmonic locking regions, which is given in Appendix B.

Furthermore, observe also that as N increases in Figure 5.10, the interaction function quickly narrows to a very small range, which no longer contains the origin, so that the Arnold tongue will skew to one side. This is illustrated in Case C of Figure 5.2, and is observed in practice for the 4:1 and 4:3 cases in Figure 5.11. This is due to the rapid decrease of energy in successive terms of the Fourier series for the Hodgkin-Huxley PRC. In fact, N:M entrainment can be established only if there is significant energy in the Nth term of this series. Because the coefficients of the Fourier series for the Hodgkin-Huxley PRC are nearly negligible beyond the fourth order, the Arnold tongues also become extremely thin, and so that subharmonic entrainment with $N = 5$ (and $M < 5$) cannot be established in practice for this system.

5.4.3 Fast subharmonic entrainment of an oscillator

An alternative objective to minimizing control energy is to entrain a system to a desired frequency as quickly as possible using a control of given energy. This problem is examined for the harmonic (1:1) case for arbitrary nonlinear oscillating systems in Section 5.3, and the

solution for the subharmonic (N:M) case extends those results by applying the techniques derived in Section 5.4.1.

Our goal here is to entrain the system (4.2) to a target frequency Ω as quickly as possible by using a periodic control v of fixed energy $P = \langle v^2 \rangle$ and forcing frequency Ω_f that satisfies $M\Omega_f = N\Omega$. Employing averaging theory as in Section 5.4.1 yields the phase drift equation (5.31), where the interaction function would ideally be of a piecewise-constant form, so that the averaged slow phase φ converges to a fixed point φ^* at a uniform rate from any initial value. However, a discontinuity at $\varphi \to \varphi^*$ would result in an unbounded control v, as explained in Lemma 2 of Appendix B, which makes such a control infeasible in practice. An alternative is to maximize $|\dot{\varphi}_*|$, the rate of convergence of the averaged slow phase in the neighborhood of its attractive fixed point φ^*. The calculus of variations can then be used to obtain a smooth optimal candidate solution that also performs well in practice. When the system (5.31) is entrained by a control v, there exists an attractive fixed point φ^* satisfying $\Lambda_v^{NM}(\varphi^*) + \Delta\omega = 0$ and $\frac{\mathrm{d}}{\mathrm{d}\varphi}\Lambda_v^{NM}(\varphi^*) < 0$, similar to Figure 5.4. Observe that by inspecting (5.24), one can write

$$\frac{\mathrm{d}}{\mathrm{d}\varphi}\Lambda_v^{NM}(\varphi^*) = \frac{\mathrm{d}}{\mathrm{d}\varphi}\langle Y^{NM}(\eta,\varphi^*)v(\eta)\rangle = \big\langle Y_\varphi^{NM}(\eta,\varphi^*)v(\eta)\big\rangle, \tag{5.42}$$

where Y^{NM} is as defined in (5.25) and $Y_\varphi^{NM}(\eta,\varphi)$ is its derivative, given by

$$Y_\varphi^{NM}(\eta,\varphi) = \frac{\mathrm{d}}{\mathrm{d}\varphi}Y^{NM}(\eta,\varphi) = \frac{1}{N}\sum_{j=0}^{N-1} Z'\left(\frac{M}{N}[2\pi j + \eta] + \varphi\right), \tag{5.43}$$

with $Z'(\theta+\varphi) = \frac{\mathrm{d}}{\mathrm{d}\varphi}Z(\theta+\varphi)$. As was done for Z in Section 5.4.1, we can define the interaction function of Z' with itself by

$$K(\varphi) \triangleq \langle Z'(\theta+\varphi)Z'(\theta)\rangle, \tag{5.44}$$

which is maximized at $\varphi = 0$ with the maximum value $K(0) = \langle Z'Z'\rangle$. The periodicity of Z implies that $|K(\varphi)| \le \langle Z'Z'\rangle$ for all $\varphi \in [0, 2\pi)$, and $K(\varphi) = K(-\varphi)$. We then define

$$S^{NM}(\varphi) \triangleq \frac{1}{N}\sum_{j=0}^{N-1} K\left(\frac{M}{N}2\pi j + \varphi\right), \tag{5.45}$$

which inherits the properties $|S^{NM}(\varphi)| \leq S^{NM}(0)$ for all $\varphi \in [0, 2\pi)$ and $S^{NM}(-\varphi) = S^{NM}(\varphi)$ from the function K. We will use the notation $S_0^{NM} \triangleq S^{NM}(0)$ and $S_*^{NM} = \min_{\phi\in[0,2\pi]} S^{NM}(\phi)$. By substituting Z' for Z and Y_φ^{NM} for Y^{NM} in (5.28), we can obtain

$$\frac{\mathrm{d}}{\mathrm{d}\phi}\Lambda^{NM}_{Y_\varphi^{NM}(\theta,\psi)}(\phi) = \frac{1}{N}\sum_{j=0}^{N-1} K\left(\frac{M}{N}2\pi j + \phi - \psi\right) = S^{NM}(\phi - \psi). \tag{5.46}$$

In addition, combining (5.42) and (5.46), the energy of the function Y_φ^{NM} is given by

$$\left\langle Y_\varphi^{NM} Y_\varphi^{NM}\right\rangle = \Lambda^{NM}_{Y_\varphi^{NM}}(0) = S_0^{NM}. \tag{5.47}$$

The functions K and S^{NM}, as defined in (5.44) and (5.45), respectively, will appear repeatedly in the following derivation of fast subharmonic entrainment controls.

In order to maximize the rate of entrainment in a neighborhood of φ^* using a control of energy P, the value of $|\dot{\varphi}|$ should be maximized for values of φ near φ^*, which occurs when $-\frac{\mathrm{d}}{\mathrm{d}\varphi}\Lambda_v^{NM}(\varphi^*)$ is large, as illustrated in Figure 5.4 for the 1:1 case. This results in the following optimal control problem formulation for fast subharmonic entrainment:

$$\max_{v\in\mathcal{P}} \quad \mathcal{J}[v] = -\frac{\mathrm{d}}{\mathrm{d}\varphi}\Lambda_v^{NM}(\varphi^*) \tag{5.48}$$

$$\text{s.t.} \quad \left\langle v^2\right\rangle = P \tag{5.49}$$

$$\Lambda_v^{NM}(\varphi^*) + \Delta\omega = 0. \tag{5.50}$$

The constraints can be adjoined to the objective using multipliers λ and μ to yield

$$\begin{aligned}\mathcal{J}[v] &= -\frac{\mathrm{d}}{\mathrm{d}\varphi}\Lambda_v^{NM}(\varphi^*) + \lambda(\left\langle v^2\right\rangle - P) + \mu(\Lambda_v^{NM}(\varphi^*) + \Delta\omega)\\ &= -\left\langle Y_\varphi^{NM}(\eta,\varphi^*)v(\eta)\right\rangle + \lambda(\left\langle v^2\right\rangle - P) + \mu\langle Y^{NM}(\eta,\varphi^*)v(\eta)\rangle + \mu\Delta\omega\\ &= \frac{1}{2\pi}\int_0^{2\pi}\left(v(\eta)\left[\mu Y^{NM}(\eta,\varphi^*) - Y_\varphi^{NM}(\eta,\varphi^*) + \lambda v(\eta)\right] - \lambda P + \mu\Delta\omega\right)\mathrm{d}\eta.\end{aligned} \tag{5.51}$$

The associated Euler-Lagrange equation is

$$\mu Y^{NM}(\eta,\varphi^*) - Y_\varphi^{NM}(\eta,\varphi^*) + 2\lambda v(\eta) = 0, \tag{5.52}$$

and solving for v yields the candidate solution

$$v_f(\eta) = \frac{1}{2\lambda}\big[Y_\varphi^{NM}(\eta,\varphi^*) - \mu Y^{NM}(\eta,\varphi^*)\big]. \tag{5.53}$$

The multipliers λ and μ can be found by substituting (5.53) into the constraints (5.49) and (5.50). This yields the equations

$$\frac{1}{4\lambda^2}\big[\big\langle Y_\varphi^{NM}Y_\varphi^{NM}\big\rangle - 2\mu\big\langle Y_\varphi^{NM}Y^{NM}\big\rangle + \mu^2\langle Y^{NM}Y^{NM}\rangle\big] = P, \tag{5.54}$$

$$\frac{1}{2\lambda}\big[\big\langle Y_\varphi^{NM}Y^{NM}\big\rangle - \mu\langle Y^{NM}Y^{NM}\rangle\big] = -\Delta\omega, \tag{5.55}$$

where averaging is done with respect to the variable η. Because Z is 2π-periodic, then Z' is as well, as are Y^{NM} and Y_φ^{NM} in both arguments. Thus one can show, e.g., using Fourier series, that $\langle Z'Z\rangle = 0$, and $\big\langle Y_\varphi^{NM}Y^{NM}\big\rangle = 0$ also, so that (5.55) yields

$$\mu = \frac{2\Delta\omega\lambda}{V_0^{NM}}, \tag{5.56}$$

where $V_0^{NM} = \langle Y^{NM}Y^{NM}\rangle$ can be seen from (5.29). Substituting this result into (5.54) leads to a quadratic equation for λ given by

$$\frac{1}{4\lambda^2}S_0^{NM} + \frac{(\Delta\omega)^2}{V_0^{NM}} = P. \tag{5.57}$$

Substituting (5.53) into the equation (5.42), and recalling that $\big\langle Y_\varphi^{NM}Y^{NM}\big\rangle = 0$, yields

$$\begin{aligned}\frac{\mathrm{d}}{\mathrm{d}\varphi}\Lambda_{v_f}^{NM}(\varphi^*) &= \frac{1}{2\lambda}\big[\big\langle Y_\varphi^{NM}(\eta,\varphi^*)Y_\varphi^{NM}(\eta,\varphi^*)\big\rangle - \mu\big\langle Y_\varphi^{NM}(\eta,\varphi^*)Y^{NM}(\eta,\varphi^*)\big\rangle\big]\\ &= \frac{1}{2\lambda}\big\langle Y_\varphi^{NM}Y_\varphi^{NM}\big\rangle = \frac{1}{2\lambda}S_0^{NM}.\end{aligned} \tag{5.58}$$

In particular, $S_0^{NM} > 0$, so we choose $\lambda < 0$ when solving (5.57) for λ in order for the expression (5.58) to be negative in order for the objective in (5.48) to be maximized. It follows that the optimal waveform and multiplier can be obtained from (5.53), (5.56) and

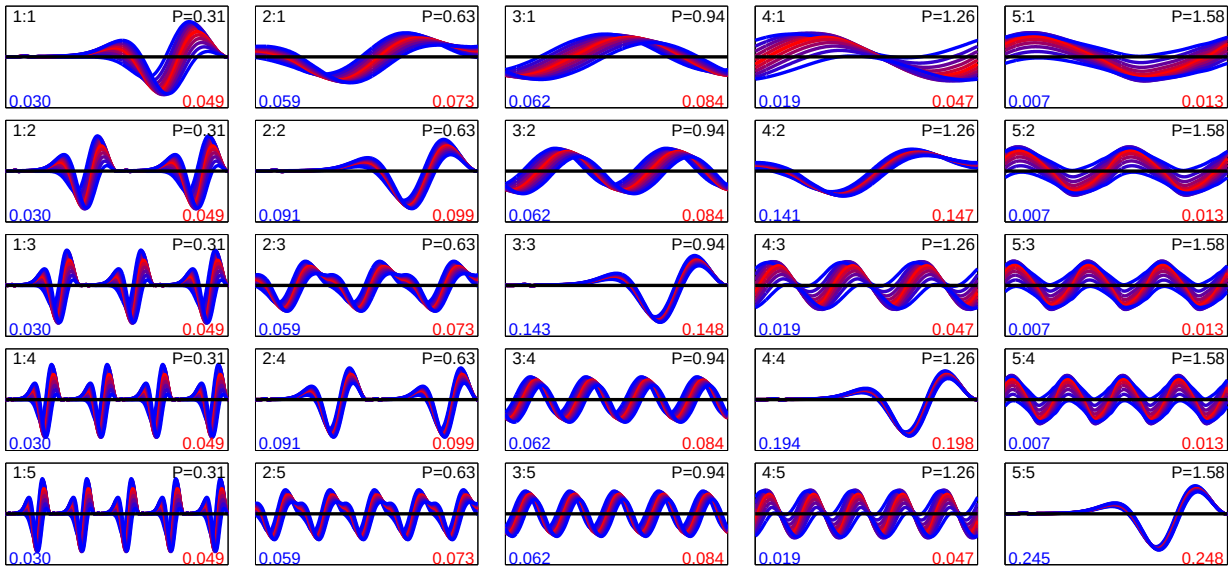

Figure 5.13: Fast subharmonic entrainment controls v_f for the Hodgkin-Huxley neuron model with frequency detuning of 0% (in red) to ±5% (in blue). The controls for N, $M = 1, \ldots, 5$ are shown rescaled to unit power, with the domain and range in each plot at $[0, 2\pi]$ and $[-3.7, 3.7]$, respectively. The black line indicates the x-axis. The entrainment ratio and RMS control energy are indicated; higher power is necessary to achieve a given detuning as the ratio N:M increases. The entrainment rate, which is characterized by the slope of $\Lambda_{v_f}^{NM}(\varphi^*)$, is noted in blue at bottom left for maximum detuning at ±5%, and in red at bottom right for zero detuning.

(5.57) as

$$v_f(\eta) = \frac{Y_\varphi^{NM}(\eta, \varphi^*)}{2\lambda} - \frac{\Delta\omega Y^{NM}(\eta, \varphi^*)}{V_0^{NM}}, \quad \lambda = -\frac{1}{2}\sqrt{\frac{S_0^{NM}}{P - \frac{(\Delta\omega)^2}{V_0^{NM}}}}, \tag{5.59}$$

where phase-locking occurs fastest when the oscillator is in the neighborhood of the phase $\psi(t) = \varphi^*$ at the start of entrainment with v_f. For zero frequency detuning, the optimal waveform is a re-scaling of Y_φ^{NM}, which is a sum of shifted derivatives of the PRC function. As $|\Delta\omega|$ increases, v continuously transforms towards a rescaling of Y^{NM}, which is the minimum energy waveform for subharmonic entrainment, as derived in the previous section. This transition reflects the conceptual trade-off between the fast entrainment objective (5.48) and frequency control constraint (5.50), which can be satisfied only when $P > (\Delta\omega)^2/V_0^{NM}$, as shown in (5.41). When $N = M = 1$, these results reduce to the harmonic (1:1) case [235]. Figure 5.13 shows the fast subharmonic entrainment controls for the Hodgkin-Huxley model for values of N, $M = 1, \ldots, 5$ at detunings between −5% and 5%, and Figure 5.14 shows several corresponding interaction functions. It is important to note that the choice of control

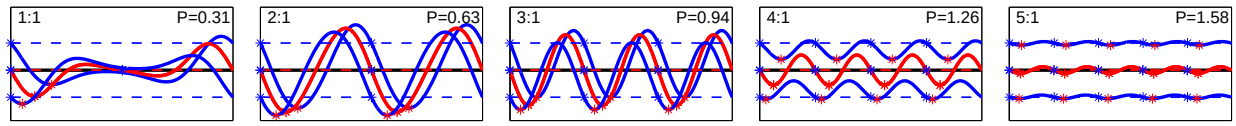

Figure 5.14: Interaction functions Λ_v^{NM} for fast subharmonic entrainment controls v_f for the Hodgkin-Huxley neuron model with frequency detuning of 0% (in red) and ±5% (in blue), where the domain and range in each plot is $[0, 2\pi]$ and $[-0.04, 0.05]$, respectively. The entrainment ratio and control energy are indicated, and the black line indicates the x-axis. As N grows large, the interaction function converges to small variation about $\Delta\omega$, which is indicated in each case by a dashed line. Red and blue stars mark the phases $\{\varphi_i^-\}$ and stable fixed points $\{\varphi_i^*\}$ of (5.31), each of which occur N times.

energy P significantly impacts the control waveform in the case of non-zero detuning, as seen in the panels on the diagonal of Figure 5.13.

The optimal waveforms for fast subharmonic entrainment given by (5.59) have been applied to the Hodgkin-Huxley model in order to verify their performance. We compare the observed entrainment rates near the asymptotic value of the slow phase with the theoretical value predicted by the gradient of the interaction function, as illustrated in Figure 5.4. We first note that near the attractive fixed point φ^*, we can model the dynamics of the averaged slow phase φ, which evolves according to (5.5), using a first order Taylor series approximation about φ^*. This takes the form

$$\dot{\varphi} = \Delta\omega + \Lambda_v^{NM}(\varphi^*) + \frac{\mathrm{d}}{\mathrm{d}\varphi}\Lambda_v^{NM}(\varphi^*)(\varphi - \varphi^*) = \frac{\mathrm{d}}{\mathrm{d}\varphi}\Lambda_v^{NM}(\varphi^*)(\varphi - \varphi^*), \tag{5.60}$$

where $\Delta\omega + \Lambda_v^{NM}(\varphi^*) \equiv 0$ because φ^* is the fixed point that yields $\dot{\varphi} = 0$ for (5.5). Setting $\varphi_0 = \varphi - \varphi^*$, the equation (5.60) becomes

$$\dot{\varphi}_0 = \frac{\mathrm{d}}{\mathrm{d}\varphi}\Lambda_v^{NM}(\varphi^*)\varphi_0 \tag{5.61}$$

when φ_0 is near zero. Recall that the slow phase itself is defined by $\phi(t) = \psi(t) - \Omega t = \psi(t) - \frac{M}{N}\Omega_f t$, and follows the dynamics (5.1). Due to the weak forcing assumption, (5.1) can be approximated near the steady state value ϕ^* by (5.61) where φ_0 is replaced with $\phi_0 = \phi(t) - \phi^*$. Hence the slow phase ϕ decays exponentially to ϕ^* according to $\ln|\phi - \phi^*| = c_0 + \frac{\mathrm{d}}{\mathrm{d}\varphi}\Lambda_v^{NM}(\varphi^*)t$, where c_0 is independent of time. This leads to the following methods for approximating entrainment rates when simulating phase models and state-space systems.

For simulations involving the phase model, we examine the slow phase by simulating the phase model (4.2) where u is the subharmonic fast entrainment input given by (5.59). In particular, we create a time-series $\phi_k := \phi(kT_e) = \psi(kT_e) - \Omega k T_e$, $k = 1, 2, \ldots$, that samples

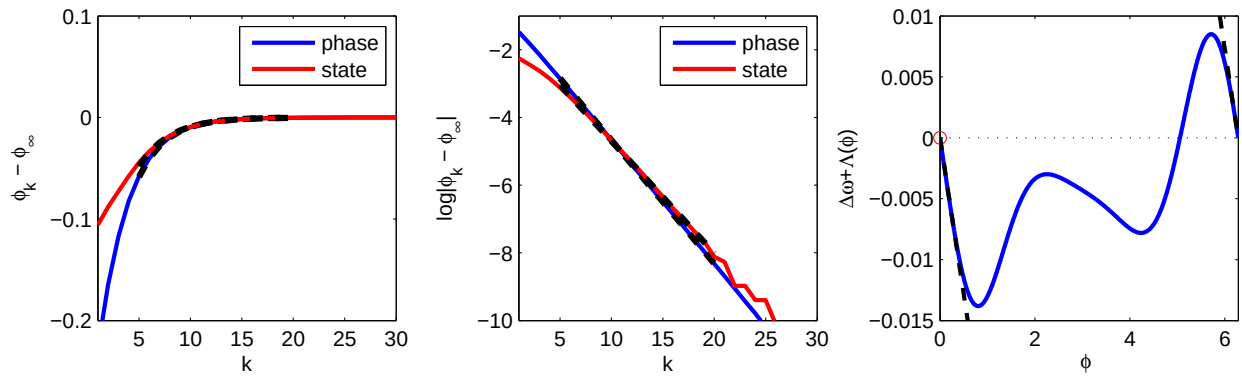

Figure 5.15: Comparing entrainment rates for the Hodgkin-Huxley model. Left: Phase difference from steady-state value $\psi_k - \psi_\infty$ as a function of period k for harmonic (1:1) fast entrainment simulations of the phase model (blue) and state-space model (red). Dashed lines show exponential fits. The target frequency is $\Omega = 1.01\omega$. Center: Linear fits with slopes κ_1 and κ_2 of the log of the phase difference from steady state for the phase model and state-space model, according to (5.62) and (5.65), respectively. The phase converges exponentially to the steady-state. Right: The dashed line is tangent to $\dot{\varphi} = \Delta\omega + \Lambda(\varphi)$ at the attractive phase $\varphi = \varphi^* = 0$. The slope of the line is $\frac{\mathrm{d}}{\mathrm{d}\varphi}\Lambda_v^{NM}(\varphi^*)$, which is the theoretical value of the convergence rate when the oscillator is in the neighborhood of φ^*. For the simulations, the system is initialized so that $\phi(0) = \psi^* - 0.4$ radians. In this example $\kappa_1 = -0.0252$, $\kappa_2 = -0.0229$, and $\frac{\mathrm{d}}{\mathrm{d}\varphi}\Lambda_v^{NM}(\varphi^*) = -0.0256$.

the slow phase system (5.1), where $T_e = 2\pi/\Omega$ is the desired period for the entrained system. The behavior of the phase difference $\phi_k - \phi^*$ in the neighborhood of ϕ^* can be closely described by an exponential decay

$$\ln|\phi_k - \phi^*| = c_0 + \kappa_1 k T_e, \tag{5.62}$$

where κ_1 is a negative coefficient that quantifies entrainment rate for the phase model. Alternatively, (5.62) leads to the relation

$$\ln|\phi_{k+1} - \phi_k| = c_1 + \kappa_1 k T_e, \tag{5.63}$$

where c_1 is independent of k.

When simulating entrainment of the state-space model, the slow phase $\phi(t)$ must be approximated by locating the peaks of the first state variable x_1. We first form the time-series $z_j := x_1(t_j)$, $j = 1, 2, \ldots$, where t_j is the time of the jth peak. Recall that we define $\psi(t) = 0 \pmod{2\pi}$ to occur when x_1 attains a peak in its cycle, so that $\psi(t_j) = 2\pi j$. We can then define a new slow phase sequence by $\phi_j := \phi(t_j) = \psi(t_j) - \Omega t_j$, which yields $t_j = (2\pi j - \phi_j)/\Omega$,

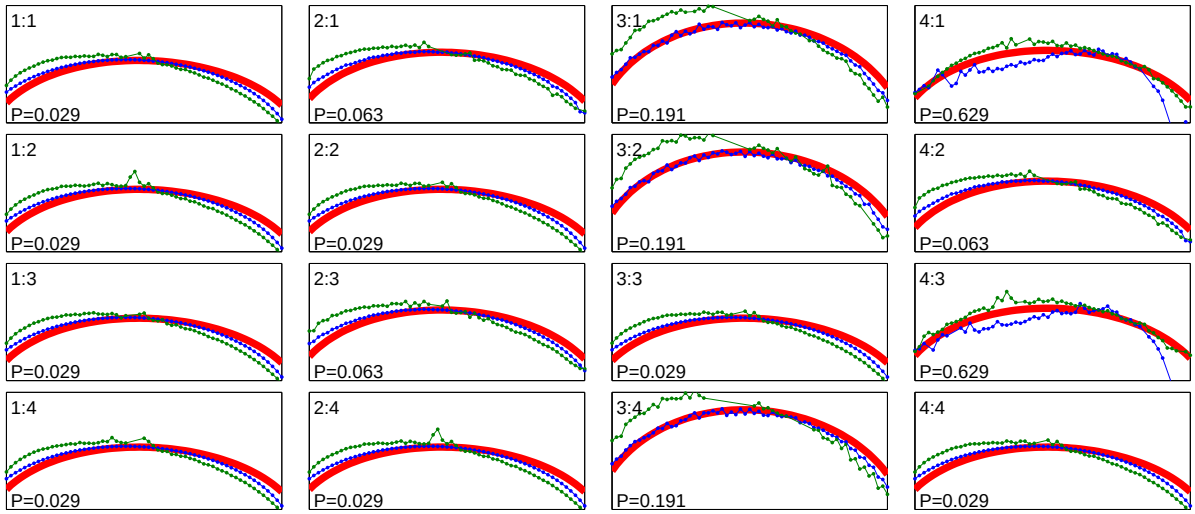

Figure 5.16: Entrainment rates resulting from subharmonic fast entrainment controls v_f in 5.59 for the Hodgkin-Huxley neuron model. The domain in each panel is the forcing frequency Ω_f on the interval of 97% to 103% of $\frac{N}{M}\omega$ where ω is the natural frequency, and the range is $[0.007, 0.050]$. The entrainment ratio is indicated at the top left, and the control waveform energy, which is adjusted to be slightly greater than the minimum to guarantee entrainment for all the detuning values for each subharmonic ratio, is given at the bottom left. The red line is the theoretical entrainment rate $\frac{\mathrm{d}}{\mathrm{d}\varphi}\Lambda_v^{NM}(\varphi^*)$, and the computed values of κ_1 and κ_2 are shown in blue and green, respectively.

and hence $t_{j+1} - t_j = T_e - (\phi_{j+1} - \phi_j)/\Omega$, which yields

$$\phi_{j+1} - \phi_j = 2\pi \frac{T_e - (t_{j+1} - t_j)}{T_e}. \tag{5.64}$$

Using the slow phase sequence $\{\phi_j\}$ instead of $\{\phi_k\}$ in (5.63) and applying (5.64) yields

$$\ln \left| 2\pi \frac{T_e - (t_{j+1} - t_j)}{T_e} \right| = c_2 + \kappa_2 j T_e, \tag{5.65}$$

where c_2 is independent of j and κ_2 is a negative coefficient that quantifies the entrainment rate for the state-space model.

The coefficients κ_1 and κ_2 are in practice very near to the theoretical entrainment rate $\frac{\mathrm{d}}{\mathrm{d}\varphi}\Lambda_v^{NM}(\varphi^*)$, and we expect κ_1 to be consistently closer to the theoretical value, because the latter is derived from the phase model. The procedures for obtaining κ_1 and κ_2 are illustrated in Figure 5.15, which illustrates an example of harmonic (1:1) fast entrainment of the Hodgkin-Huxley system phase model and state-space model where $\Omega = 1.01\omega$, and where the theoretical and computed entrainment rates are found to be very similar. In addition, the same experiment is repeated for subharmonic (N:M) entrainment and for a range of values of

the detuning $\Delta\omega$, and the results are given in Figure 5.16. The values are in close agreement, although the computation becomes problematic at higher entrainment ratios. Observe that the entrainment rate is highest near the center of each panel in Figure 5.16, which corresponds to $\Delta\omega \equiv 0$. This is because the frequency of the oscillator does not need to be altered, so that the entrainment rate maximization objective (5.48) takes precedence in the problem formulation posed in (5.48)-(5.50). Conversely, when the detuning is greater, i.e., when Ω is farther from ω, the optimal theoretical and observed entrainment rate is lower, because the the frequency entrainment design constraint (5.50) influences the problem significantly.

The solution waveforms derived in this chapter are optimal in the case of the weak forcing assumption, as described in Section 5.1. Many approximations are made in the process of phase reduction and averaging, so that the controls presented above are optimal only in an asymptotic sense, as the input energy $\langle v^2 \rangle$ approaches zero. An analysis of the accuracy and divergence from optimality of the produced controls, taking into account control amplitude, accuracy of phase reduction, and effects of averaging is a challenging problem that is left for future work. It is important to emphasize that the techniques presented here provide a straightforward way to compute near optimal controls numerically, and have been applied successfully in an experimental setting [235]. Furthermore, the simulation shown in Figure 5.12 demonstrates that the optimal waveforms obtained using the phase modeling technique produce a similar result to the theory when applied to both the phase model and original model. This strongly supports the hypothesis that optimal entrainment controls derived using a phase model are very near optimal for the original system, provided the oscillator remains within a neighborhood of its limit cycle.

In this chapter, we have developed a methodology for the design of optimal entrainment controls for a single oscillator by taking advantage of the phase model reduction technique. In the following chapter, these results are extended to techniques for optimal entrainment of ensembles of oscillators, as well as methods for manipulating their complex interactions to produce dynamic patterns.

Chapter 6

Entrainment of Nonlinear Oscillator Ensembles

Much of the work on the control of nonlinear oscillators is based on the assumption that each dynamical unit behaves according to pre-defined underlying dynamics, such as the Hodgkin-Huxley equations [99], which constitute a widely studied model of action potential propagation in a squid giant axon. However, in practical applications of neural control and engineering, the systems in question are collections of biological neurons that exhibit variation in parameters that characterize the system dynamics, specifically the frequency of oscillation and sensitivity to external stimuli. Although such a system consists of a finite collection of subsystems, it contains so many unobservable elements, each with parameter uncertainty, that its collective dynamics are most practically modeled by indexing the subsystems by a parameter varying on a continuum. The control of such neural systems therefore lies within an emerging and challenging area in mathematical control theory called ensemble control, which encompasses a class of problems involving the guidance of an uncountably infinite collection of structurally identical dynamical systems with parameter variation by applying a common open-loop control [137]. In the context of phase model reduction, the appropriate indexing parameter for such a collection of oscillating systems is natural frequency [238]. Therefore, a practical approach to the optimal design of inputs that entrain a collection of neurons is to first consider a family of phase models with common nominal PRC and natural frequency varying over a specified interval. Optimal waveforms that entrain a collection of phase oscillators with the greatest range of frequencies by weak periodic forcing have been characterized for certain oscillating chemical systems [95], and this approach has been extended to a method for optimal entrainment of oscillating systems with arbitrary PRC [236, 238]. In this chapter, we present a method for engineering weak, periodic signals

that entrain ensembles of structurally similar uncoupled oscillators with variation in system parameters to a desired target frequency without the use of state feedback. The theory is developed in the context of subharmonic entrainment, in order to produce the most general results possible, which can be reduced to the 1:1 case by using $N = M = 1$. The same controls can also be viewed as optimal inputs for the entrainment of a single oscillating system with parameter uncertainty in a known range. In the following section, we begin by examining the reduction of an ensemble of oscillators to phase coordinates, and investigate the utility of this approximation using the Hodgkin-Huxley neuron model as an example.

6.1 Phase Reduction Approximation for Oscillator Ensembles

In practice, physical systems exhibit variation in parameters that characterize the system dynamics, which must be taken into account when designing optimal entrainment controls. We approach this issue by modeling an ensemble of systems as a collection of phase models with a common PRC that is derived using a nominal parameter set, and the frequencies span the range of natural frequencies resulting from phase model reduction of systems with parameters in a specified range. A justification of this approach and a sensitivity analysis is provided in Section 5 in [238]. The following extension of this modeling and control technique to subharmonic (N:M) entrainment parallels our previous work [238] by incorporating the theory derived in Section 5.4, as well as a more rigorous optimality proof and additional generalizations.

Specifically, we consider a collection of systems

$$\dot{x} = f(x, u, p), \tag{6.1}$$

where $x \in \mathbb{R}^n$ is the state, $u \in \mathbb{R}$ is a scalar control, and $p \in \mathcal{D} \subset \mathbb{R}^d$ is a vector of constant parameters varying on a hypercube $\mathcal{D}$ containing a nominal parameter vector p^0. Each system can be reduced to a scalar phase model

$$\dot{\psi} = \omega(p) + Z(\psi, p)u, \tag{6.2}$$

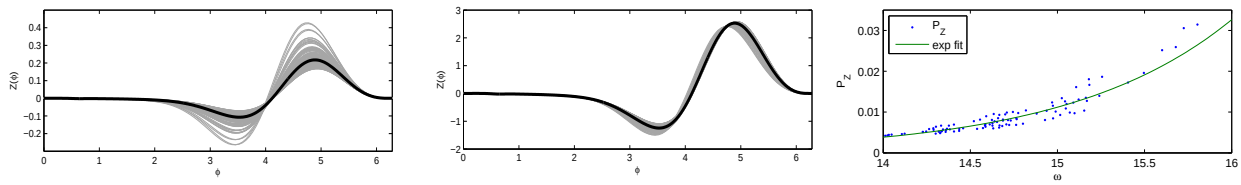

(a) (b) (c)

Figure 6.1: 6.1(a) Phase response curves of the Hodgkin-Huxley neuron model and 6.1(b) the same curves normalized to unit energy. Each of the 2^7 grey curves corresponds to a PRC obtained when each of the parameters V_{Na}, V_K, V_L, $\overline{g}_{Na}$, $\overline{g}_K$, $\overline{g}_L$, and c is perturbed by 2% above or below its nominal value, i.e. to the corner points in a parameter space hypercube. In plot 6.1(b) the PRCs of the perturbed systems are similar to the black curve, which is the PRC corresponding to the nominal parameter set. 6.1(b) shows the energy P_Z of PRC at each corner point as a function of the corresponding natural frequency (dots), as well as an exponential fit.

where the natural frequency and PRC depend on the parameter vector p. In order to design a control that entrains the ensemble for all $p \in \mathcal{D}$, we approximate it by

$$\{\dot{\theta} = \omega(p) + Z(\theta, p^0)u \ : \ p \in \mathcal{D}\}, \tag{6.3}$$

where $Z(\theta, p^0)$ is the PRC obtained from (6.1) using the nominal parameter vector.

In this section, we provide the results of several numerical simulations that further justify our approach to the entrainment of neural ensembles. In particular, we examine the effect of parameter variation on the phase response curve and optimal entrainment control for an ensemble of neurons. We also provide a visualization of the uncertainty in the entrainment properties of a neuron ensemble that arises due to such parameter variation. This is done by computing an Arnold tongue distribution, in which the minimum RMS energy required for entrainment of the ensemble to a given target frequency Ω is a random variable with a probability density on the positive real line, instead of a single value, for each $\omega \in (\omega_1, \omega_2)$. We demonstrate that the optimal entrainment waveform is minimally sensitive to variation in underlying system parameters, that it is always superior to a generic waveform such as a sinusoid or square pulse train, and that its amplitude can be appropriately chosen to entrain the neuron with the most problematic parameter set in the ensemble.

The following sensitivity analysis can be performed to examine the effect of parameter variation on the PRC of an oscillator. Suppose that $p = (p_1, \ldots, p_d)$ are the parameters that characterize the system dynamics (6.1), with nominal values $p^0 = (p_1^0, \ldots, p_d^0)$. We compute

the PRC $Z(\theta, p)$ at each corner of a hypercube $\mathcal{D} = \prod_{i=1}^{d}(\beta_i, \gamma_i)$, where (β_i, γ_i) is a small confidence interval for p_i^0. The corner points of $\mathcal{D}$ are examined in particular in order to analyze the aggregate effect of uncertainty in all parameters. If the 2^d curves so obtained are similar to the nominal PRC, then the optimal controls derived using the latter will be near optimal for entrainment of an uncertain ensemble. Such a robustness property is important in practical neural entrainment applications, because biological oscillators exhibit significant variation from any nominal model. Our analysis of the sensitivity of the Hodgkin-Huxley PRC to parameter variation appears in Figure 6.1, in which we have used $(\beta_i, \gamma_i) = (0.98p_i^0, 1.02p_i^0)$ for the $d = 7$ parameter values in the model. For each of the corner points of $\mathcal{D}$ we plot in Figure 6.1(b) the PRC of the Hodgkin-Huxley system, normalized to unit energy, and find that it does not vary significantly from the nominal curve. This supports our assertion that the optimal entrainment waveform is minimally sensitive to variation in underlying system parameters. Note that the energy of the PRC can take different values for the same value of ω, depending on the original system parameters, and approximately follows an exponential trend, as shown in Figure 6.1(c).

Although minor variations in Hodgkin-Huxley neuron model parameter values do not significantly effect the shape of the PRC, they do have a significant effect on the amplitude, and hence the entrainment properties of a neuron ensemble forced by a fixed waveform v. The resulting uncertainty is visualized as an Arnold tongue distribution, which is the probability distribution of the minimum RMS control energy required to entrain an ensemble of oscillators, with parameter set distributed on a given probability space $\mathcal{D}$, as a function of natural frequency ω. In practice, we can estimate this empirically for a hypercube $\mathcal{D}$ with uniform probability measure by uniformly randomly generating samples $p_k \in \mathcal{D}$ of the parameter for $k = 1, \ldots, N$, for which we compute the natural frequency ω_k of the perturbed Hodgkin-Huxley model and the minimum RMS control energy $P_k(v)$ required to entrain the kth model using v. This results in N samples that are plotted on the energy-frequency plane, as shown in Figure 6.2(a), which displays the empirical Arnold tongue distribution, using $N = 500$ samples, for a sinusoidal control waveform and for the optimal waveform v_* that maximizes the range of entrainment. From visual inspection one concludes that the optimal waveform entrains the perturbed model using lower energy than the sinusoid in the majority of cases. More distinctly, Figure 6.2(b) displays the ratio between the minimum RMS energy levels required to entrain each parameter set p_k using the optimal control and a sinusoid, as a function of the natural frequency ω_k. Not only is the ratio below unity in most cases, with an average of 0.78, but there is also a clear trend line at 0.8 in the frequency range

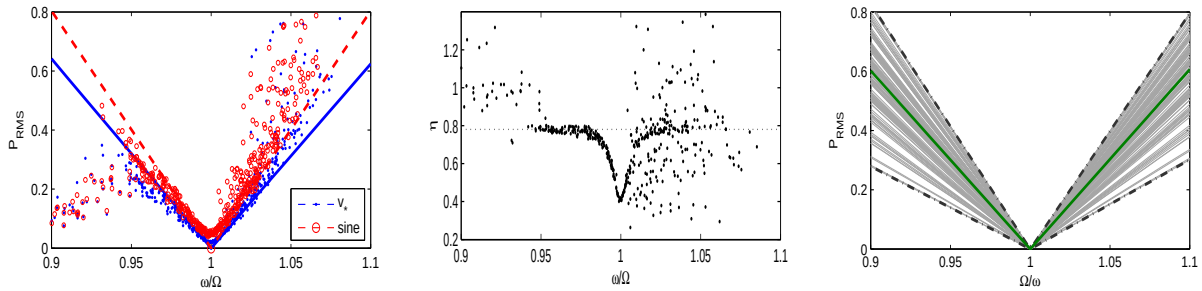

(a) (b) (c)

Figure 6.2: (a) Arnold tongue distributions for an ensemble of Hodgkin-Huxley neurons with uniform random parameter variation on $(\beta_i, \gamma_i) = (.95p_i^0, 1.05p_i^0)$, where $p^0(p_1^0, \ldots, p_7^0)$ are nominal values for the parameter set V_{Na}, V_K, V_L, $\overline{g}_{Na}$, $\overline{g}_K$, $\overline{g}_L$, and c. The target Ω is the nominal natural frequency. There are $N = 500$ randomly perturbed parameter sets used to generate empirical distributions (points) for entrainment with a sinusoid v_s (red $\circ$), and with v_* (blue $\cdot$), the optimal waveform for entrainment to $\Omega = \frac{1}{2}(\omega_1 + \omega_2)$. Solid lines are theoretical Arnold tongue boundaries. (b) The ratio $\eta_k = P_k(v_*)/P_k(v_s)$ plotted as a function of ω/Ω, the natural frequency of the neuron with parameter set p_k (rescaled by the target frequency). (c) The optimal waveform requires an average of 22% less RMS energy for entrainment than a sinusoid. Theoretical Arnold tongues for entrainment of Hodgkin-Huxley neurons with parameter sets at the corner points of $\mathcal{D}$ with $(\beta_i, \gamma_i) = (0.98p_i^0, 1.02p_i^0)$, where the target Ω is the nominal natural frequency. The Arnold tongues for the nominal parameter set (green) and the corner points (grey) are bounded by those of the best- and worst- case scenarios. Each is generated using the PRC Z_p for parameter set p.

$0.95 < \omega < 0.99$, with a much lower ratio for natural frequencies near the target Ω. This result strongly supports the assertion that the optimal ensemble entrainment waveform derived using our method is superior to traditional waveforms such as the sinusoid, not only for phase-reduced models, but also for the underlying non-reduced dynamical system model.

For a given oscillator ensemble, given a confidence region hypercube $\mathcal{D}$ for the parameter set P, the PRC can be computed at each corner point of $\mathcal{D}$ and can be used to approximate the corresponding Arnold tongue when the perturbed system is entrained by the optimal waveform v_* for the nominal parameter set. In order to assure robust entrainment of the entire ensemble, the RMS energy of v_* should be chosen such that it entrains the oscillator with the worst case parameter set, whose theoretical Arnold tongue is indicated by the top dashed line in Figure 6.2(c). The nominal oscillator is entrained with an RMS energy 24% lower than the worst case scenario. This difference is very near the average of 22% less RMS energy that the optimal waveform requires to entrain an oscillator with parameter uncertainty. It follows that simply by using the waveform v_* instead of a square wave or

sinusoid one can significantly enhance the likelihood that entrainment of an ensemble will be robust to such parameter variation. The technique for deriving such optimal waveforms v_* is presented in the following sections.

6.2 Minimum-Energy Entrainment of Oscillator Ensembles

The following derivation of minimum-energy waveforms for the entrainment of oscillator ensembles is presented in the general subharmonic context. A collection of parameterized dynamical systems of the form (6.1) are assumed to be well-represented by an ensemble of the form (6.3). Our strategy is to derive a minimum energy periodic control signal $u(t) = v(\Omega_f t)$ that guarantees entrainment for each system in the ensemble (6.3), which is of the form

$$\mathcal{F} = \{\dot{\psi} = \omega + Z(\psi)u \ : \ \omega \in [\omega_1, \omega_2]\}, \tag{6.4}$$

to a frequency Ω, where the target and forcing frequencies satisfy $M\Omega_f = N\Omega$. We approach the subharmonic entrainment of oscillator ensembles by applying the theory in Section 5.4.1 to the derivation of optimal ensemble controls in Section 4 of [238], which appears in [240]. We call the range of frequencies that are entrained by the control v applied at the frequency Ω_f with subharmonic ratio $N{:}M$ the subharmonic locking range $R_\Omega^{NM}[v] = [\omega_-, \omega_+]$, and when $[\omega_1, \omega_2] \subseteq R_\Omega^{NM}[v]$ we say that the ensemble $\mathcal{F}$ is entrained. This requirement results in two constraints, which can be visualized with the help of Figure 6.3, of the form

$$\begin{array}{rclclcl} \Delta\omega_+ & \triangleq & \omega_+ - \Omega & = & -\Lambda_v^{NM}(\varphi^-) & \geq & \omega_2 - \Omega \ \triangleq \ \Delta\omega_2, \\ \Delta\omega_- & \triangleq & \omega_- - \Omega & = & -\Lambda_v^{NM}(\varphi^+) & \leq & \omega_1 - \Omega \ \triangleq \ \Delta\omega_1. \end{array} \tag{6.5}$$

The objective of minimizing control energy $\langle v^2 \rangle$ given the constraints (6.5) gives rise to the optimization problem

$$\begin{array}{ll} \min & \mathcal{J}[v] = \langle v^2 \rangle, \quad v \in \mathcal{P} \\ \text{s.t.} & \Delta\omega_2 + \Lambda_v^{NM}(\varphi^-) \leq 0, \\ & -\Delta\omega_1 - \Lambda_v^{NM}(\varphi^+) \leq 0. \end{array} \tag{6.6}$$

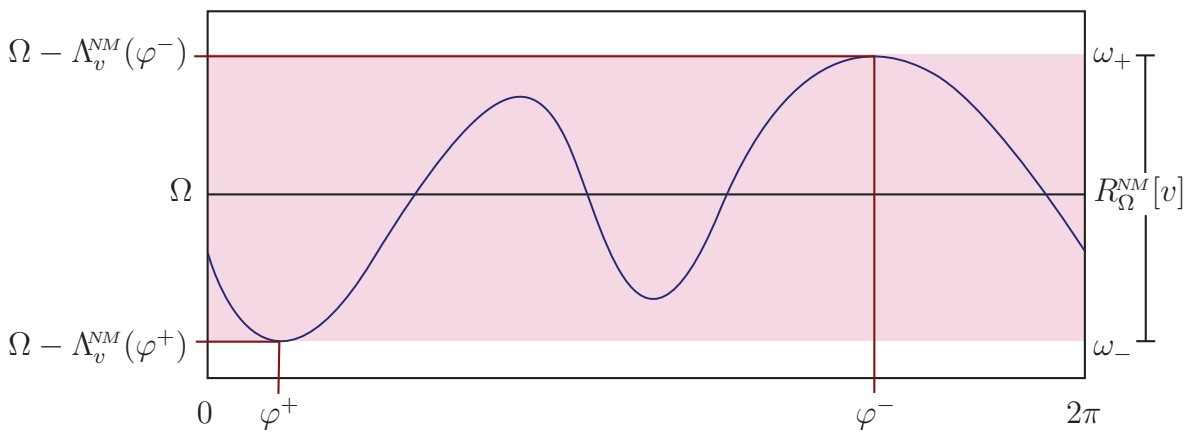

Figure 6.3: This graphic illustrates the constraints (6.5). The curve shown is $\Omega - \Lambda_v^{NM}(\varphi)$, and the frequency locking region $R_\Omega^{NM}[v] = [\omega_-, \omega_+]$ is indicated by pink shading. When $[\omega_1, \omega_2] \subseteq R_\Omega^{NM}[v]$, then the collection (6.4) is entrained to Ω.

We refer to the event that one of v_+ (when $\omega_2 < \Omega$) or v_- (when $\omega_1 > \Omega$) in (5.39) can solve the problem (6.6) as Case I. Understanding the Arnold tongues that characterize subharmonic entrainment of ensembles in the form of $\mathcal{F}$, as illustrated in Figure 6.4, will clarify the conditions when (5.39) is optimal, and when another class of solutions, which we call Case II, is superior. We derive this condition, which depends on the ensemble parameters ω_1 and ω_2 and Z as well as the target frequency Ω and the subharmonic ratio $N{:}M$.

6.2.1 The ensemble Arnold tongue

In contrast to the description in Section 5.1.2 of the Arnold tongue associated with a single oscillator and a given waveform, for an ensemble $\mathcal{F}$ we are interested in the relationship between the locking range $R_\Omega^{NM}[v]$ and the RMS control power. Therefore, we define the ensemble Arnold tongue as the set of pairs $(\omega, P_v^{NM}) \in \mathbb{R}^2$ that result in entrainment of an oscillator in $\mathcal{F}$ with natural frequency ω to a frequency Ω_f at a subharmonic $N{:}M$ ratio using the waveform v, where w is the natural frequency of the oscillator. The equation (5.6) is modified to $\omega - \Omega + P_v^{NM}(\omega) \cdot \Lambda_{\tilde{v}}^{NM}(\varphi) = 0$, where the left and right boundaries of the Arnold tongue are approximated by solving for $P_v^{NM}(\omega)$ as a function of ω and substituting $\varphi = \varphi^-$

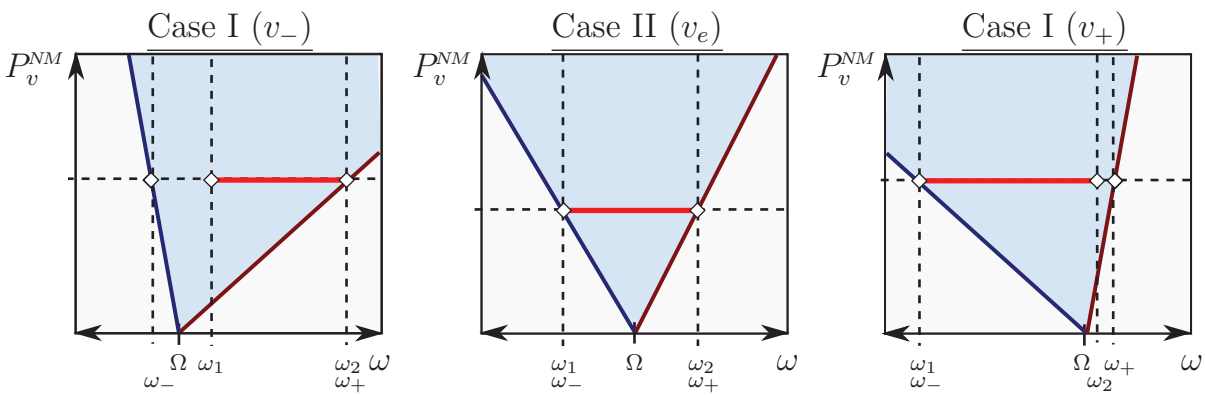

Figure 6.4: Illustration of ensemble Arnold tongues for Case I (both v_- and v_+) and Case II controls, which are used when constraints on $\Lambda_v^{NM}(\varphi^-)$ and $\Lambda_v^{NM}(\varphi^+)$ are active. Note that one-sided tongues as in Figure 5.2 can occur in either case, depending on N, M, and the PRC Z. The range $[\omega_1, \omega_2]$ of frequencies in the ensemble $\mathcal{F}$ is marked with a red bar.

and $\varphi = \varphi^+$, respectively. This yields

$$P_v^{NM}(\omega) = \begin{cases} (\Omega - \omega)/\Lambda_{\widetilde{v}}^{NM}(\varphi^-), & \text{right} \\ (\Omega - \omega)/\Lambda_{\widetilde{v}}^{NM}(\varphi^+), & \text{left}, \end{cases} \tag{6.7}$$

as a linear estimate of the ensemble Arnold tongue boundary, where $\widetilde{v} = v/\sqrt{\langle v^2 \rangle}$ is the unit power normalization of v as before. Illustrations of Arnold tongues for the two possible cases are illustrated in Figure 6.4. The notion of ensemble Arnold tongues guides the derivation in the following subsections of the possible optimal control solutions and criteria for optimality of these different cases.

6.2.2 Case I: One constraint is active

To derive the conditions when (5.39) is optimal, we focus on the entrainment of $\mathcal{F}$ to a frequency $\Omega \in [\omega_1, \omega_2]$ using v_- when $\Delta\omega_+ = \Delta\omega_2 > -\Delta\omega_1$ (i.e., when ω_2 is further from Ω than ω_1) while noting that the case where v_+ is optimal for $\Delta\omega_2 < -\Delta\omega_1 = -\Delta\omega_-$ (i.e., when ω_1 is further from Ω than ω_2) is symmetric. Because ω_2 is the natural frequency in the ensemble farthest from Ω, we use $\Delta\omega = \Delta\omega_2$ in (5.39), and then check whether $[\omega_1, \omega_2] \subseteq R_\Omega^{NM}$. Then the first constraint in (6.6) is active, which yields

$$-\Delta\omega_+ = \Lambda_v^{NM}(\varphi^-) = -\Delta\omega_2, \tag{6.8}$$

so that $\omega_+ = \omega_2$ is the upper bound on the locking range $R_\Omega^{NM}[v]$, as desired. It remains to determine $\Lambda_v^{NM}(\varphi^+) = \Omega - \omega_-$, from which we obtain the lower bound ω_- on $R_\Omega^{NM}[v]$. Using the expression (5.24) for $\Lambda_v^{NM}(\varphi)$ together with the solution for v_- in (5.39) using $\Delta\omega = \Delta\omega_2$, we find that

$$\Lambda_{v_-}^{NM}(\varphi) = \langle Y^{NM}(\eta, \varphi) v_-(\eta) \rangle = -\frac{\Delta\omega_2}{V_0^{NM}} V^{NM}(\varphi - \varphi^-). \tag{6.9}$$

Observe that $\Lambda_v^{NM}(\varphi)$ is maximized when $V^{NM}(\varphi - \varphi^-)$ is minimized, and hence to find $\Lambda_v^{NM}(\varphi^+)$ it suffices to find the minimum value V_*^{NM} of V^{NM}. It follows that

$$\Lambda_{v_-}^{NM}(\varphi^+) = -\frac{\Delta\omega_2}{V_0^{NM}} V_*^{NM}, \tag{6.10}$$

and the lower bound of $R_\Omega^{NM}[v]$ is $\omega_- = \Omega - \Lambda_v^{NM}(\varphi^+)$. If $\omega_- < \omega_1$, then $[\omega_1, \omega_2] \subseteq R_\Omega^{NM}[v]$, hence the control v_- in (5.39), with $\Delta\omega = \omega_2 - \Omega$, is the minimum energy solution to problem (6.6), and entrains $\mathcal{F}$ to the frequency Ω.

Therefore to determine whether the problem is optimally solved by v_-, the decision criterion is obtained by combining the definition $\Lambda_v^{NM}(\varphi^+) = -\Delta\omega_-$ with (6.8) and (6.10) to yield the boundary estimate $\Delta\omega_- = \Delta\omega_+ V_*^{NM}/V_0^{NM}$. Thus if the relation

$$\Delta\omega_1 > \Delta\omega_- = \frac{\Delta\omega_2}{V_0^{NM}} V_*^{NM} \tag{6.11}$$

is satisfied, then v_- with $\Delta\omega = \Delta\omega_2$ will be optimal. The derivation of the condition when v_+ is optimal is symmetric, and results in a boundary estimate $\Delta\omega_+ = \Delta\omega_1 V_*^{NM}/V_0^{NM}$. It follows that if the condition

$$\Delta\omega_2 < \Delta\omega_+ = \frac{\Delta\omega_1}{V_0^{NM}} V_*^{NM} \tag{6.12}$$

holds, then the control v_+ with $\Delta\omega = \Delta\omega_1$ is optimal for entraining $\mathcal{F}$ to the frequency Ω. When neither (6.11) or (6.12) holds, then neither v_- or v_+ in (5.39) is the solution to (6.6). In the following subsection, we derive the optimal solution for that case.

6.2.3 Case II: Both constraints are active

In Case I above, when (5.39) is optimal for entraining the ensemble (6.4), only one of the constraints in problem (6.6) is active. When neither of the conditions (6.11) and (6.12) is satisfied, the solution to problem (6.6) occurs when both constraints are active. To derive this solution, we adjoin the constraints in (6.6) to the minimum energy objective function using multipliers μ_- and μ_+, which gives rise to the cost functional

$$\begin{aligned}\mathcal{J}[v] &= \left\langle v^2 \right\rangle - \mu_-(\Delta\omega_2 + \Lambda_v^{NM}(\varphi^-)) - \mu_+(-\Delta\omega_1 - \Lambda_v^{NM}(\varphi^+)) \\ &= \frac{1}{2\pi}\int_0^{2\pi} \Big(v(\eta)[v(\eta) - \mu_- Y^{NM}(\eta,\varphi^-) + \mu_+ Y^{NM}(\eta,\varphi^+)] \\ &\qquad - \mu_-\Delta\omega_2 + \mu_+\Delta\omega_1 \Big) \mathrm{d}\eta, \end{aligned} \tag{6.13}$$

where we have used the expression (5.24) for Λ_v^{NM}. Solving the Euler-Lagrange equation yields

$$v_e(\theta) = -\frac{1}{2}[\mu_+ Y^{NM}(\eta,\varphi^+) - \mu_- Y^{NM}(\eta,\varphi^-)], \tag{6.14}$$

which we substitute back into problem (6.6) to obtain

$$\begin{aligned}\left\langle v_e^2 \right\rangle &= \frac{1}{4}\langle \big(\mu_+ Y^{NM}(\eta,\varphi^+) - \mu_- Y^{NM}(\eta,\varphi^-)\big)^2 \rangle \qquad (6.15)\\ &= \frac{1}{4}(\mu_+^2 + \mu_-^2)V_0^{NM} - \frac{1}{2}\mu_+\mu_- V^{NM}(\Delta\varphi),\end{aligned}$$

$$\Lambda_{v_e}^{NM}(\varphi^+) = -\frac{1}{2}\mu_+ V_0^{NM} + \frac{1}{2}\mu_- V^{NM}(\Delta\varphi), \tag{6.16}$$

$$\Lambda_{v_e}^{NM}(\varphi^-) = \frac{1}{2}\mu_- V_0^{NM} - \frac{1}{2}\mu_+ V^{NM}(\Delta\varphi), \tag{6.17}$$

where $\Delta\varphi = \varphi^+ - \varphi^-$ is the range spanned by $\Lambda_v^{NM}(\varphi)$ for $\varphi \in [0, 2\pi]$. Using the expressions (6.15), (6.16), and (6.17) transforms the functional optimization problem (6.6) into a

nonlinear programming problem in the variables μ_-, μ_+, and $V^{NM}(\Delta\varphi)$, given by

$$\begin{aligned} \min \quad & \mathcal{J}[\mu_-, \mu_+, V(\Delta\varphi)] = \tfrac{1}{4}(\mu_+^2 + \mu_-^2)V_0^{NM} - \tfrac{1}{2}\mu_+\mu_- V^{NM}(\Delta\varphi) \\ \text{s.t.} \quad & \Delta\omega_2 + \tfrac{1}{2}\mu_- V_0^{NM} - \tfrac{1}{2}\mu_+ V^{NM}(\Delta\varphi) \leq 0, \\ & -\Delta\omega_1 + \tfrac{1}{2}\mu_+ V_0^{NM} - \tfrac{1}{2}\mu_- V^{NM}(\Delta\varphi) \leq 0. \end{aligned} \tag{6.18}$$

We focus in Case II on optimal solutions to problem (6.18) for which both constraints are active. Indeed, when Case I is in effect, one of conditions (6.11) or (6.12) is satisfied, so that $\mu_+ = 0$ or $\mu_- = 0$, and problem (6.18) is reduced to problem (5.35) with $\lambda = \mu_-$ or $\lambda = -\mu_+$, respectively. Otherwise, both constraints in problem (6.18) are active, with multipliers given by

$$\begin{aligned} \mu_+ &= \frac{2(\Delta\omega_1 V_0^{NM} - \Delta\omega_2 V^{NM}(\Delta\varphi))}{(V_0^{NM} - V^{NM}(\Delta\varphi))(V_0^{NM} + V^{NM}(\Delta\varphi))}, \\ \mu_- &= \frac{2(\Delta\omega_1 V^{NM}(\Delta\varphi) - \Delta\omega_2 V_0^{NM})}{(V_0^{NM} - V^{NM}(\Delta\varphi))(V_0^{NM} + V^{NM}(\Delta\varphi))}. \end{aligned} \tag{6.19}$$

For these multipliers, the objective in problem (6.18) is reduced to function of $\beta = V^{NM}(\Delta\varphi)$ given by

$$\begin{aligned} \mathcal{J}[\beta] &= \frac{(\Delta\omega_1 V_0^{NM} - \Delta\omega_2\beta)^2 + (\Delta\omega_1\beta - \Delta\omega_2 V_0^{NM})^2}{(V_0^{NM} - \beta)^2(V_0^{NM} + \beta)^2} V_0^{NM} \\ &\quad - \frac{2(\Delta\omega_1 V_0^{NM} - \Delta\omega_2\beta)(\Delta\omega_1\beta - \Delta\omega_2 V_0^{NM})\beta}{(V_0^{NM} - \beta)^2(V_0^{NM} + \beta)^2}. \end{aligned} \tag{6.20}$$

Differentiating the cost (6.20) with respect to β results in

$$\frac{\mathrm{d}\mathcal{J}[\beta]}{\mathrm{d}\beta} = -2\frac{(V_0^{NM}\Delta\omega_1 - \beta\Delta\omega_2)(V_0^{NM}\Delta\omega_2 - \beta\Delta\omega_1)}{(V_0^{NM} - \beta)^2(V_0^{NM} + \beta)^2}. \tag{6.21}$$

Recall that because neither of the conditions (6.11) or (6.12) holds, then

$$V_0^{NM}\Delta\omega_1 - V_*^{NM}\Delta\omega_2 < 0 \qquad \text{and} \qquad V_0^{NM}\Delta\omega_2 - V_*^{NM}\Delta\omega_1 > 0. \tag{6.22}$$

We are restricted to $\beta = V^{NM}(\Delta\varphi) \in [V_*^{NM}, V_0^{NM}]$, so we write $V_*^{NM} - \beta = p(V_*^{NM} - V_0^{NM})$ for some $p \in [0, 1]$. In addition, the fact that $\omega_1 < \omega_2$ results in $\Delta\omega_1 - \Delta\omega_2 < 0$ and

$\Delta\omega_2 - \Delta\omega_1 > 0$. Therefore the quantities in the numerator of (6.21) satisfy

$$\begin{aligned} V_0^{NM}\Delta\omega_1 - \beta\Delta\omega_2 &= V_0^{NM}\Delta\omega_1 - V_*^{NM}\Delta\omega_2 + (V_*^{NM} - \beta)\Delta\omega_2 \\ &= V_0^{NM}\Delta\omega_1 - V_*^{NM}\Delta\omega_2 + p(V_*^{NM} - V_0^{NM})\Delta\omega_2 \\ &= p(\Delta\omega_1 - \Delta\omega_2)V_0^{NM} + (1-p)(V_0^{NM}\Delta\omega_1 - V_*^{NM}\Delta\omega_2) < 0, \end{aligned} \tag{6.23}$$

$$\begin{aligned} V_0^{NM}\Delta\omega_2 - \beta\Delta\omega_1 &= V_0^{NM}\Delta\omega_2 - V_*^{NM}\Delta\omega_1 + (V_*^{NM} - \beta)\Delta\omega_1 \\ &= V_0^{NM}\Delta\omega_2 - V_*^{NM}\Delta\omega_1 + p(V_*^{NM} - V_0^{NM})\Delta\omega_1 \\ &= p(\Delta\omega_2 - \Delta\omega_1)V_0^{NM} + (1-p)(V_0^{NM}\Delta\omega_2 - V_*^{NM}\Delta\omega_1) > 0. \end{aligned} \tag{6.24}$$

The relations (6.23) and (6.24) imply that (6.21) is positive for all values of $\beta = V^{NM}(\Delta\varphi) \in [V_*^{NM}, V_0^{NM}]$, so that the cost (6.20) increases when $V^{NM}(\Delta\varphi)$ does. Therefore the objective (6.20) is minimized when $V^{NM}(\Delta\varphi)$ is, which occurs when $V^{NM}(\Delta\varphi) = V_*^{NM}$. Therefore the problem (6.18) is solved when

$$\Delta\varphi = \varphi_*^{NM} = \underset{\varphi\in[0,2\pi]}{\operatorname{argmin}} V^{NM}(\varphi), \tag{6.25}$$

and the multipliers are as in (6.19). The locking range for this control is then exactly $R_\Omega^{NM}[v_e] = [\omega_1, \omega_2]$, which satisfies the entrainment constraints (6.5).

By combining the results in Sections 6.2.2 and 6.2.3 for Cases I and II we can completely characterize the minimum energy control that entrains the ensemble $\mathcal{F}$ in (6.4) to a target frequency Ω with subharmonic ratio N:M. This full solution is

$$v_e(\eta) = \begin{cases} -\dfrac{\Delta\omega_1}{V_0^{NM}} Y^{NM}(\eta, \varphi^+) & \text{if} \quad \Delta\omega_2 < \dfrac{\Delta\omega_1}{V_0^{NM}} V_*^{NM}, \\[2ex] \dfrac{(\Delta\omega_2 V_*^{NM} - \Delta\omega_1 V_0^{NM})}{(V_0^{NM} - V_*^{NM})(V_0^{NM} + V_*^{NM})} Y^{NM}(\eta, \varphi_*^{NM}) \\ \qquad + \dfrac{(\Delta\omega_1 V_*^{NM} - \Delta\omega_2 V_0^{NM})}{(V_0^{NM} - V_*^{NM})(V_0^{NM} + V_*^{NM})} Y^{NM}(\eta, 0) & \text{if} \quad \begin{cases} \Delta\omega_1 < \dfrac{\Delta\omega_2}{V_0^{NM}} V_*^{NM} \\ \text{and} \\ \Delta\omega_2 > \dfrac{\Delta\omega_1}{V_0^{NM}} V_*^{NM} \end{cases} \\[2ex] -\dfrac{\Delta\omega_2}{V_0^{NM}} Y^{NM}(\eta, \varphi^-) & \text{if} \quad \Delta\omega_1 > \dfrac{\Delta\omega_2}{V_0^{NM}} V_*^{NM}. \end{cases} \tag{6.26}$$

Finally, the energy of v_e, which is the minimum value of the objective (6.13), is

$$\left\langle v_e^2 \right\rangle = \begin{cases} \dfrac{(\Delta\omega_1)^2}{V_0^{NM}} & \text{if} \quad \Delta\omega_2 < \dfrac{\Delta\omega_1}{V_0^{NM}} V_*^{NM}, \\ \\ \dfrac{(\Delta\omega_1^2 + \Delta\omega_2^2)V_0^{NM} - 2\Delta\omega_1\Delta\omega_2 V_*^{NM}}{(V_0^{NM} - V_*^{NM})(V_0^{NM} + V_*^{NM})} & \text{if} \quad \begin{cases} \Delta\omega_1 < \dfrac{\Delta\omega_2}{V_0^{NM}} V_*^{NM} \\ \text{and} \\ \Delta\omega_2 > \dfrac{\Delta\omega_1}{V_0^{NM}} V_*^{NM} \end{cases} \\ \\ \dfrac{(\Delta\omega_2)^2}{V_0^{NM}} & \text{if} \quad \Delta\omega_1 > \dfrac{\Delta\omega_2}{V_0^{NM}} V_*^{NM}. \end{cases} \tag{6.27}$$

We have shown that the minimum energy periodic control $u(t) = v(\frac{N}{M}\Omega t)$ that achieves subharmonic entrainment of an ensemble of oscillators (6.4) to a target frequency Ω is an appropriately weighted sum of shifted functions Y^{NM}, as given in (5.25), where $\eta = \frac{N}{M}\Omega t = \Omega_f t$ is the forcing phase. When $N = M = 1$, these results reduce to the optimal solution for the harmonic (1:1) case [238]. Figure 6.5 shows the minimum energy subharmonic controls for ensembles of Hodgkin-Huxley neurons for $N, M = 1, \ldots, 5$ and several ranges of $[\omega_1, \omega_2]$. We have also presented generalized criteria for using the two derived classes of optimal controls, which can be applied to systems with Type I (strictly positive) and Type II PRCs, while the derivation in our previous work on 1:1 entrainment required $Q_* < 0$. It is important to note that using $\Omega = \frac{1}{2}(\omega_1 + \omega_2)$ allows the ensemble to be entrained with a minimum control energy, as in the case of $[\omega_1, \omega_2] = [0.95\omega, 1.05\omega]$. One can then consider a dual objective of maximizing the locking range of entrainment given a fixed power, as described in the following section.

6.3 Maximum locking range for subharmonic entrainment

In some applications, the frequency range $[\omega_1, \omega_2]$ of the oscillators in $\mathcal{F}$ in (6.4) is not known, or it is desirable to entrain the largest collection of oscillators with similar PRC but uncertain frequency. For such cases, we seek a control v that maximizes the locking range of entrainment $R_\Omega^{NM}[v]$ for a fixed control energy $\langle v^2 \rangle = P$. Because $R_\Omega^{NM}[v] = [\omega_-, \omega_+]$, we wish to maximize $\omega_+ - \omega_- = \Delta\omega_+ - \Delta\omega_- = \Lambda_v^{NM}(\varphi^+) - \Lambda_v^{NM}(\varphi^-)$, where the latter equality

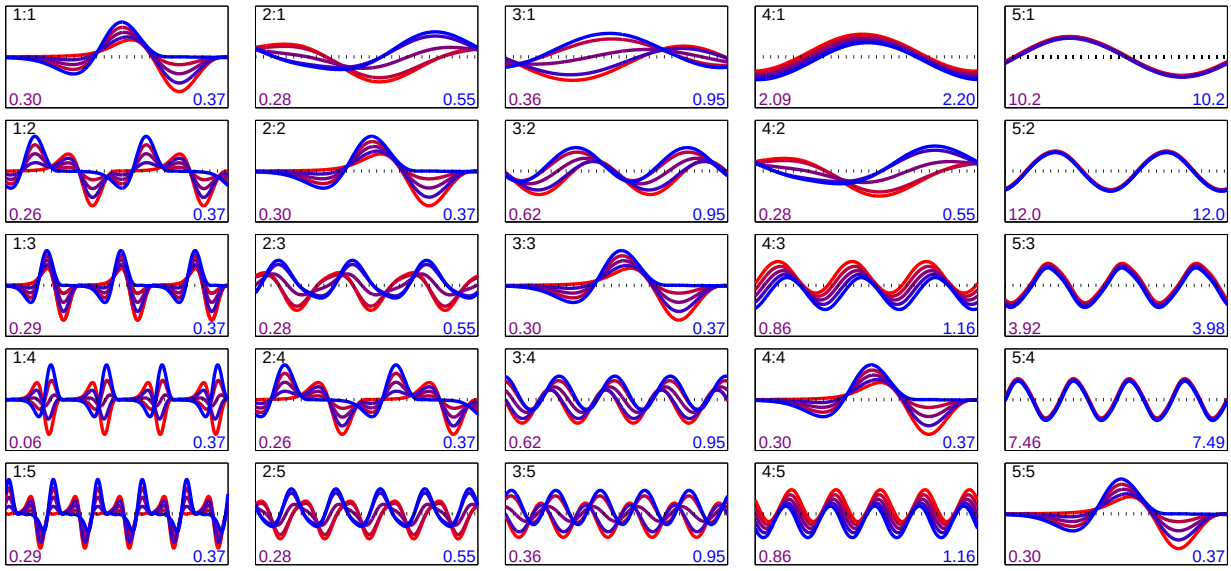

Figure 6.5: Minimum energy subharmonic entrainment controls for Hodgkin-Huxley neuron ensembles with frequency ranges $[0.925\omega, 1.025\omega]$, $[0.9375\omega, 1.0375\omega]$, $[0.95\omega, 1.05\omega]$, $[0.9625\omega, 1.0625\omega]$, and $[0.975\omega, 1.075\omega]$, colored in order from red to blue, and target frequency $\Omega = \omega$ equal to the nominal natural frequency in Appendix A.1. In each panel, the controls are rescaled so that the greatest energy waveform has unit energy, and the domain and range in each plot is $[0, 2\pi]$ and $[-3.7, 3.7]$, respectively. The entrainment ratio is indicated at the top, while the lowest energy (for v_r (purple)) and highest energy (for v_- (red) or v_+ (blue)) are shown at bottom left and right, respectively.

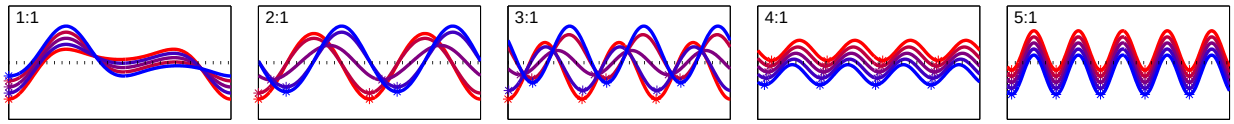

Figure 6.6: Interaction functions for the controls shown in Figure 6.5, where the domain and range in each plot is $[0, 2\pi]$ and $[-0.05, 0.05]$, respectively. The entrainment ratio is indicated, and the black line denotes the x-axis.

is due to the constraints 6.5. The resulting optimization problem can be formulated as

$$\max_{v \in \mathcal{P}} \quad \mathcal{J}[v] = \Lambda_v^{NM}(\varphi^+) - \Lambda_v^{NM}(\varphi^-) \tag{6.28}$$

$$\text{s.t.} \quad \langle v^2 \rangle = P. \tag{6.29}$$

By adjoining the constraint to (6.29) to the objective using a multiplier λ, we obtain a cost functional given by

$$\begin{aligned}\mathcal{J}[v] &= \Lambda_v^{NM}(\varphi^+) - \Lambda_v^{NM}(\varphi^-) - \lambda(\langle v^2\rangle - P)\\ &= \langle Y^{NM}(\eta,\varphi^+)v(\eta)\rangle - \langle Y^{NM}(\eta,\varphi^-)v(\eta)\rangle - \lambda(\langle v^2\rangle - P)\\ &= \frac{1}{2\pi}\int_0^{2\pi}\big(v(\eta)\big[Y^{NM}(\eta,\varphi^+) - Y^{NM}(\eta,\varphi^-) - \lambda v(\eta)\big] + \lambda P\big)\mathrm{d}\eta. \end{aligned} \tag{6.30}$$

Solving the Euler-Lagrange equation yields a candidate solution in the form

$$v_r(\eta) = \frac{1}{2\lambda}\big[Y^{NM}(\eta,\varphi^+) - Y^{NM}(\eta,\varphi^-)\big]. \tag{6.31}$$

By applying (5.28), the interaction function is shown to be

$$\Lambda_{v_r}^{NM}(\varphi) = \frac{1}{2\lambda}[V^{NM}(\varphi-\varphi^+) - V^{NM}(\varphi-\varphi^-)], \tag{6.32}$$

so the objective (6.28) is given by

$$\Lambda_{v_r}^{NM}(\varphi^+) - \Lambda_{v_r}^{NM}(\varphi^-) = \frac{1}{\lambda}[V^{NM}(0) - V^{NM}(\Delta\varphi)]. \tag{6.33}$$

It follows that to maximize the entrainment range, the phase $\Delta\varphi$ must minimize V^{NM} in order to maximize the span of the interval $R_\Omega^{NM}[v]$, hence $\Delta\varphi = \varphi_*^{NM}$ as in (6.25). In addition, substituting the candidate solution (6.31) into the constraint (6.29) yields

$$P = \langle v_r^2\rangle = \frac{1}{4\lambda^2}\big[2\langle Y^{NM}Y^{NM}\rangle - 2\langle Y^{NM}(\eta,\varphi^+)Y^{NM}(\eta,\varphi^-)\rangle\big] = \frac{1}{2\lambda^2}[V_0^{NM} - V_*^{NM}], \tag{6.34}$$

so that solving for the multiplier λ yields

$$\lambda = \frac{1}{\sqrt{2P}}\sqrt{V_0^{NM} - V_*^{NM}}. \tag{6.35}$$

Therefore the waveform of energy P with maximum locking range $R_\Omega^{NM}[v]$ for an ensemble of the form (6.4) is given by

$$v_r(\eta) = \frac{\sqrt{P}}{\sqrt{2(V_0^{NM} - V_*^{NM})}}[Y^{NM}(\eta,\varphi_*^{NM}) - Y^{NM}(\eta,0)]. \tag{6.36}$$

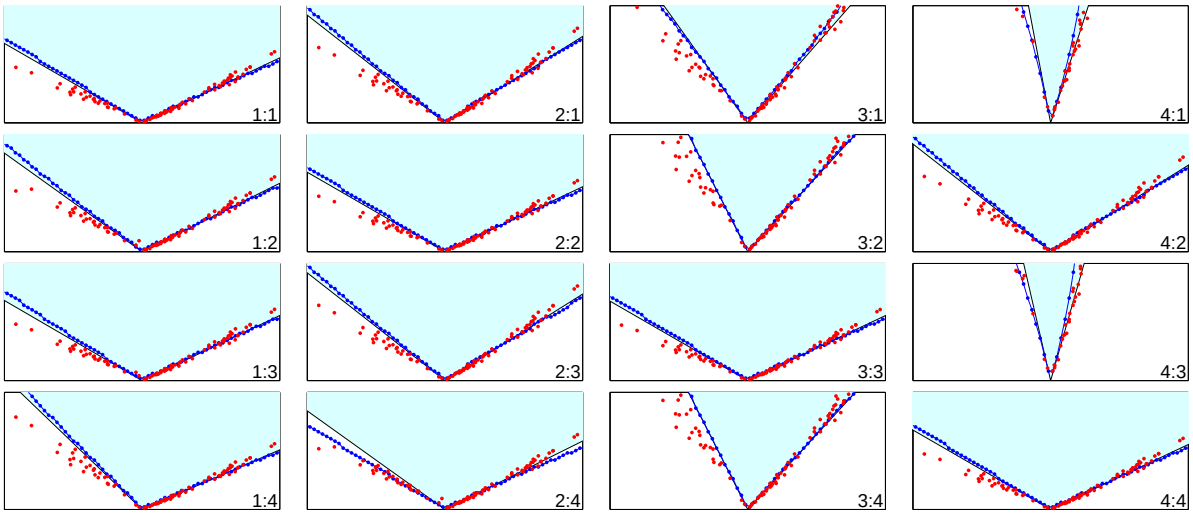

Figure 6.7: Arnold tongues for minimum-energy subharmonic entrainment ensemble controls v_e for Hodgkin-Huxley neurons, where the target frequency is $\Omega = 0.99\omega$. The domain in each panel is the forcing frequency Ω_f on the interval of 90% to 110% of $\frac{N}{M}\omega$ where ω is the natural frequency, and the range is $[0, .5]$. The entrainment ratio is indicated at the bottom right. The shaded region is the theoretical Arnold tongue as determined by (6.7). The computed boundaries of the Arnold tongues are shown in blue for entrainment of the phase model, and minimum entrainment energies for the state-space model with parameter values at the corner points of $\mathcal{D}$ are shown in red.

Note that although a phase ambiguity exists because we have solved for $\Delta\varphi$, but not for φ^+ and φ^-, the initial phase at which the control is applied is unimportant because entrainment is an asymptotic process. The waveform (6.36) is actually a special case of (6.27) when $\Omega = \frac{1}{2}(\omega_1 + \omega_2)$, and the extremal detunings $\Delta\omega_2 = -\Delta\omega_1$ are related to the control energy by $P = 2(\Delta\omega_2)^2/(V_0^{NM} - V_*^{NM})$. Such controls are shown in purple in Figure 6.5. We may deduce that the control (6.36) results in the greatest locking range for a fixed control energy, and can be applied at subharmonic forcing frequency $\Omega_f = \frac{N}{M}\frac{1}{2}(\omega_1 + \omega_2)$ to entrain the ensemble $\mathcal{F}$ with minimum control energy. These dual objectives are optimized by the same waveform, and this link clarifies the relationship between the interaction function and the maximal frequency locking range, which was first observed for harmonic entrainment [95, 236].

Examination of entrainment regions for the waveforms v_e in (6.26) that entrain ensembles of oscillators is complicated by the alternative notion of entraining an ensemble, as illustrated in Figure 6.4. Rather than varying the forcing frequency to compute Arnold tongue of a single oscillator with fixed natural frequency, this notion of an ensemble Arnold tongue requires the forcing frequency to remain fixed while the forcing energy required to entrain oscillators with varying natural frequency is determined. Recall that in Section 6.1 we considered a

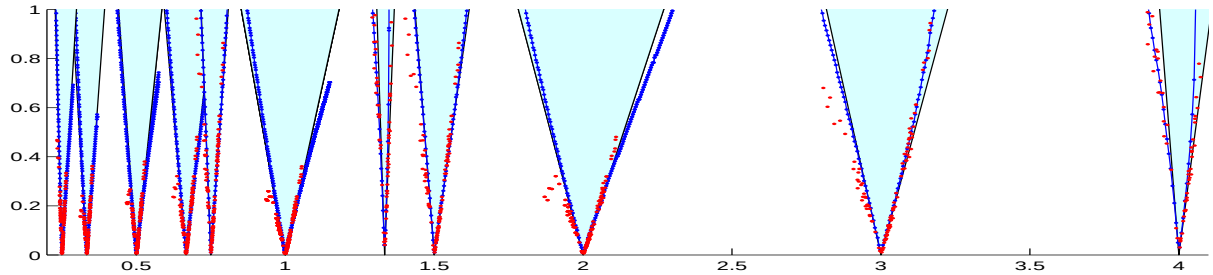

Figure 6.8: Arnold tongues for minimum energy subharmonic entrainment ensemble controls v_e for Hodgkin-Huxley neurons, where the target frequency is $\Omega = 0.99\omega$. All of the Arnold tongues in Figure 6.7 are shown together on one plot, where the domain is Ω_f/ω, i.e., the ratio between the forcing and natural frequencies.

collection of systems $\dot{x} = f(x, u, p)$ where $p \in \mathcal{D} \subset \mathbb{R}^d$ is a vector of constant parameters varying on a hypercube $\mathcal{D}$ containing a nominal parameter vector p^0. This collection was reduced to the ensemble $\mathcal{F}$ in (6.4). Thus the ensemble Arnold tongues for the phase-reduced ensemble can be computed by varying ω in $\mathcal{F}$ and computing the boundaries as described above. For the ensemble of state-space oscillators, we consider the parameter hypercube $\mathcal{D} := \prod_{i=1}^{7}[.98p_i^0, 1.02p_i^0]$, where $p^0 = (p_1^0, \ldots, p_7^0)$ represents the nominal set of parameters V_{Na}, V_K, V_L, $\overline{g}_{Na}$, $\overline{g}_K$, $\overline{g}_L$, and c of the Hodgkin-Huxley system. Each corner of $\mathcal{D}$ corresponds to a frequency of oscillation, for which we find the minimum power $P_{\tilde{v}}^{NM}(\omega)$ that results in entrainment. These points are plotted along with the shaded theoretical Arnold tongues in Figures 6.7 and 6.8, which arise from simulations in which the target frequency is set to 99% of the nominal frequency for the Hodgkin-Huxley system.

Figures 5.11 and 5.12 show close agreement between the phase-locking regions predicted from the theory and the computed boundaries when the forcing frequency Ω_f is within several percent of $\frac{N}{M}\omega$, and the first order approximation for the phase dynamics given by the model 4.2 is accurate. For larger frequency detuning, the nonlinear behavior of the oscillation is not captured by the phase model. Figures 6.7 and 6.8 show that the theoretical and computed ensemble Arnold tongues agree as well.

The above results on the entrainment of oscillator ensembles can be interpreted as a means of shaping the Arnold tongue characterizing the entrainment of an oscillatory ensemble. By adjusting the forcing waveform while keeping the forcing frequency Ω_f fixed, it is possible to significantly alter the frequency range (w_1, w_2) of the collection of oscillators $\mathcal{F}$ subjected to subharmonic phase-locking. The main focus here is on accomplishing such manipulation in an optimal manner. By using an input of appropriate frequency, entrainment of a given

ensemble $\mathcal{F}$ may be achieved using a biased sinusoid of the form $u(t) = b_0 + b_1 \sin(\Omega_f t)$ with appropriate constants b_0, b_1, and Ω_f. However, the derived waveforms accomplish this design goal using significantly less energy. Furthermore, the analysis of Arnold tongues for minimum-energy waveforms provides a framework for studying the possibilities and limitations of engineering entrainment of rhythmic systems on multiple time scales, for instance in an interacting network. Such analysis may also shed light on the evolved optimal periodic activity of complex multi-scale biological systems. For example, experimentally measured subharmonic entrainment regions were approximated by injecting single Aplysia motoneurons with sinusoidal inputs of varying frequency and amplitude [108], resulting in plots similar to Figures 6.7 and 6.8.

An indirect implication of the above results concerns the phase-locking properties of a collection of simultaneously entrained oscillators. Specifically, the interaction function between the PRC of one or more oscillators and the common control input can be used to determine, and moreover design, the relative phases of such a collection. So far, the focus here has been entirely on the frequency locking aspect of entrainment, and the fixed point of the average slow phase φ to which oscillators converge was not considered as long as the frequency control objective is satisfied. However, as one can see in Figure 5.1, the form of the interaction function determines the asymptotic phases of entrained oscillators, which is of particular interest when manipulating the synchronization of multiple rhythmic units. The techniques presented above are extended in the following section to engineer synchronization in collections of oscillators using weak forcing without feedback information, which is of compelling interest in electrochemistry [119], neuroscience [219], and circadian biology [81]. The impact may be greatest on the ability to manipulate collections of biological circadian and neural systems, for which the entrained phases may need to be designed in a nonuniform manner, by using common inputs.

6.4 Phase Assignment for Oscillator Ensembles

In this section, we describe an innovative perspective on modeling and control of complex and uncertain rhythmic dynamical systems in which a common input is applied to produce a dynamical pattern in a collection of oscillators without requiring a certain coupling structure. In addition, the oscillators involved may have arbitrary dynamics, as long as they exhibit

sufficient nonlinear relaxation for the control design to be realizable. Furthermore, knowledge of the initial state of the oscillators is not required, and control input designs are robust to uncertainty in the parameters of each oscillating system, as well as to disturbances, in a way that can be directly quantified. Finally, a desired synchronization structure can often be established and subsequently maintained for a collection of oscillators simply by applying the appropriate periodic waveform. Therefore, switching between synchronization patterns in a collection of oscillators can be as simple as switching between input waveforms.

Crucially, the fundamental results in Section 5.1 provide insight into the use of ergodic theory to engineer synchronization structures in real collections of rhythmic dynamical units. These techniques do not depend on the particular model or system involved, and can be applied to weakly nonlinear oscillators even when the system dynamics are uncertain or even unknown. The results in Chapter 5 and Sections 6.1 through 6.3 focus entirely on manipulating the frequency of one or more oscillating systems. They have been confirmed computationally [236, 238, 240] as described in detail in Chapter 5, as well as in practice [235] for the experimental electrochemical apparatus in Section 5.3, for which a representation of the form (4.2) can only be inferred experimentally. These results are subsequently extended to account for the phase structures that can result in periodically forced collections of heterogeneous oscillators, and are applied to produce control design techniques that are constructive, tractable, and verifiable in real laboratory dynamical systems.

The following section describes a method for establishing a desired phase relationship among a collection of non-interacting nonlinear dynamical oscillating systems that are mutually synchronized by an external forcing signal without the use of feedback information. In addition, it is of interest to derive conditions, based on the dynamics of the oscillators, on the ability to produce a desired pattern. As before, phase model reduction and an ergodic averaging approximation form the foundation for the technique.

6.4.1 Stability of Synchronization Structures in Oscillator Ensembles

The theory in Section 5.1 can be extended to understand the long-run behavior of a collection of P nonlinear oscillators with phase-reduced dynamics given by

$$\mathcal{F} = \{\dot{\psi}_i = \omega_i + Z(\psi_i)u,\ i = 1, \ldots, P\} \tag{6.37}$$

which all share an identical PRC. If an input of the form $u(t) = v(\Omega t)$, where v is 2π-periodic, entrains all of the oscillators in $\mathcal{F}$ to a frequency Ω, then the pattern that emerges in the asymptotic relative phase of the oscillators can be computed from the interaction function and the frequencies ω_i. Specifically, in the steady state the phase of each synchronized oscillator will evolve with a fixed relation ϕ_i^∞ to the forcing phase $\theta = \Omega t$, i.e., $\psi_i(t) = \Omega t + \phi_i^\infty$, or equivalently $\phi_i(t) = \phi_i^\infty$, where $\phi_i(t) = \psi_i(t) - \Omega t$. Such a configuration is shown in Figure 6.11(c). The synchronization dynamics that result from the entrainment of $\mathcal{F}$ can be understood by examining the interaction function between v and Z. By applying the averaging procedure in Section 5.1 to each system in $\mathcal{F}$, we obtain a collection of averaged dynamics of the form (5.5), which we denote $\langle\mathcal{F}\rangle$, and which is given by

$$\langle\mathcal{F}\rangle = \{\dot{\varphi}_i = \Delta\omega_i + \Lambda_v(\varphi_i),\ i = 1, \ldots, P\}. \tag{6.38}$$

Because we consider oscillators for which the limit cycles are strongly attractive, we may assume that $\lim_{t\to\infty} \varphi_i(t) = \lim_{t\to\infty} \phi_i(t) = \phi_i^\infty$ holds. When synchronization of the collection $\langle\mathcal{F}\rangle$ to the fixed points ϕ_i^∞ occurs, then $\dot{\varphi}_i = \Delta\omega_i + \Lambda_v(\varphi_i) = 0$, with

$$(i)\ \Lambda_v(\phi_i^\infty) = -\Delta\omega_i \quad \text{and} \quad (ii)\ \Lambda_v'(\phi_i^\infty) < 0, \quad i = 1, \ldots, P, \tag{6.39}$$

where condition (ii) guarantees that the dynamical configuration is attractive and stable. Conversely, it follows that if Λ_v satisfies (6.39), and the initial phases of the oscillators in $\mathcal{F}$ satisfy $\psi_i(0) = \phi_i^\infty$ for $i = 1, \ldots, P$, then the synchronization pattern will be maintained. The pattern is also established and maintained when the initial conditions are relaxed to $\psi_i(0) \in \mathcal{A}_i(\phi_i^\infty)$ for $i = 1, \ldots, P$, where $\mathcal{A}_i(\phi_i^\infty)$ is the set of initial phases for which the ith oscillator of $\langle\mathcal{F}\rangle$ is attracted to the asymptotic phase difference ϕ_i^∞. These regions are illustrated for an example interaction function in Figure 6.9. Note that for a given collection (6.38) of entrained oscillators the stable synchronization pattern may not be unique, but

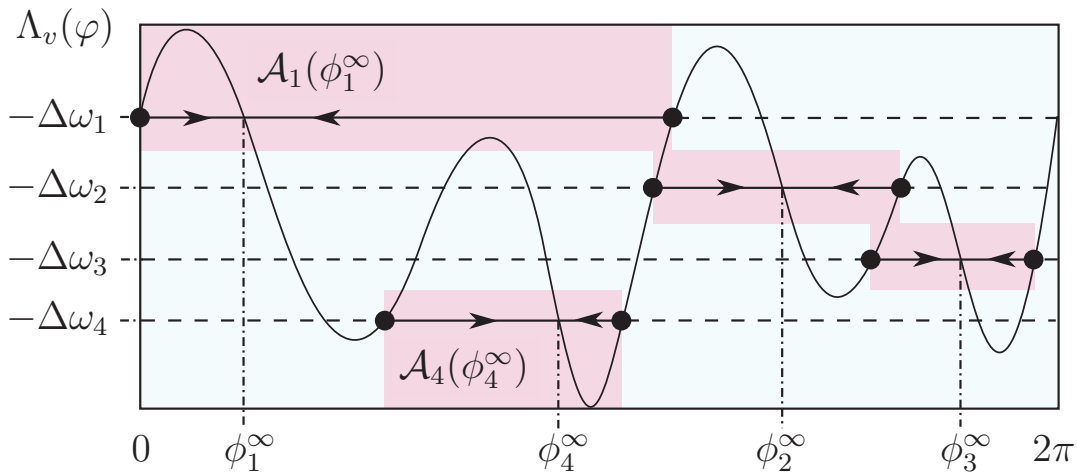

Figure 6.9: Illustration of an interaction function $\Lambda_v(\varphi)$ that satisfies the conditions (6.39). The desired synchronization pattern is established if $\psi_i(0)$ falls within the attractive set $\mathcal{A}_i(\phi_i^\infty)$ for all $i = 1, \ldots, N$, which is indicated by shading between dots, corresponding to the desired synchronization pattern.

rather depends on the initial conditions $\psi_i(0)$ of the collection (6.37). In the following section, we present a method for constructing an input v using the conditions (6.39) as design requirements in order to produce a desired synchronization structure.

6.4.2 Design of Phase Structures in Synchronized Oscillators

The analysis in Section 6.4.1 characterizes the synchronization pattern that arises when a collection of heterogenous oscillators with the same PRC and different natural frequencies are entrained by a periodic input signal. This suggests a method for creating an input signal v that maintains a desired pattern in the collection $\mathcal{F}$ by first designing the interaction function Λ_v to satisfy the conditions in (6.39), and then computing an input v that results in the designed Λ_v. In this way, a desired pattern with relative phase ϕ_i^∞ for the ith oscillator will persist if $\psi_i(0) \in \mathcal{A}_i(\phi_i^\infty)$ holds for $i = 1, \ldots, P$. Moreover, if v can also be chosen such that Λ_v satisfies $\mathcal{A}_i(\phi_i^\infty) = [0, \pi)$, then the pattern with relative phases ϕ_i^∞ will be established for any set of initial conditions $\psi_i(0)$, as illustrated in Figure 6.10. A technique for designing a control that satisfies these conditions is presented below. The approach involves approximate Fourier synthesis and inversion of the desired interaction function.

Because the PRC $Z(\theta)$, input waveform $v(\theta)$, and interaction function $\Lambda_v(\varphi)$ are all 2π-periodic, they are conveniently represented using Fourier series, and $\Lambda_v(\varphi)$ can readily be computed using (5.3), trigonometric identities, and the orthogonality of the Fourier basis, as

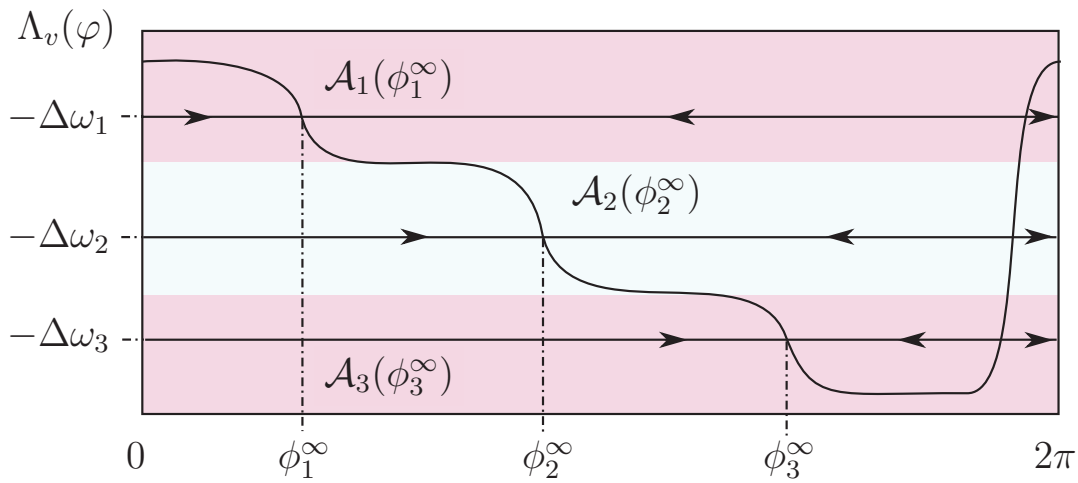

Figure 6.10: Illustration of a monotone step interaction function $\Lambda_v(\varphi)$ that satisfies the design requirements (6.39), and $\mathcal{A}_i(\phi_i^\infty) = [0, \pi)$ for $i = 1, \ldots, N$. The desired synchronization pattern is globally attractive, and is established for any initial conditions $\psi_i(0)$ for $i = 1, \ldots, N$.

described in Appendix B. The functions Z and v are represented in using truncated Fourier series expansions

$$Z(\theta) \approx Z^r(\theta) = \frac{a_0}{2} + \sum_{n=1}^{r} [a_n \cos(n\theta) + b_n \sin(n\theta)], \tag{6.40}$$

$$v(\theta) \approx v^r(\theta) = \frac{c_0}{2} + \sum_{n=1}^{r} [c_n \cos(n\theta) + d_n \sin(n\theta)], \tag{6.41}$$

where the appropriate order r is chosen based on $Z(\theta)$, as discussed below. Applying trigonometric angle sum identities and the orthogonality of the Fourier basis yields

$$\Lambda_v^r(\varphi) = \frac{f_0}{2} + \frac{1}{2}\sum_{n=1}^{r} f_n \cos(n\varphi) + \frac{1}{2}\sum_{n=1}^{r} g_n \sin(n\varphi), \tag{6.42}$$

where

$$f_0 = \frac{a_0 c_0}{4}, \quad f_n = a_n c_n + b_n d_n, \quad g_n = b_n c_n - a_n d_n. \tag{6.43}$$

Therefore given truncated Fourier expansions $\Lambda_v^r(\theta)$ and $Z^r(\theta)$, the Fourier coefficients of the corresponding truncated control waveform $v^r(\theta)$ are given by

$$c_0 = 4\frac{f_0}{a_0}, \quad c_n = 2\frac{f_n a_n + b_n g_n}{a_n^2 + b_n^2}, \quad d_n = 2\frac{f_n b_n - a_n g_n}{a_n^2 + b_n^2}. \tag{6.44}$$

It is thus crucial for the expansion order r to be appropriately chosen such that $a_n^2 + b_n^2 > \delta_Z$ for $r \leq n$, and any order n for which $a_n^2 + b_n^2 = 0$ occurs to be omitted from the approximation. This guarantees that numerical conditioning errors do not arise, and so that the designed $v^r(\theta)$ satisfies the weak forcing assumption. An appropriate value for the tolerance is $\delta_Z = \langle Z^2 \rangle \cdot 10^{-4}$. Hence given the input $u(t) = v^r(\Omega t)$, the asymptotic configuration of the entrained oscillators of (6.38) will approximately satisfy the conditions (6.39).

We call the entrainment input design described here the monotone step function method. Consider a phase assignment task for a collection $\mathcal{F}$ of P oscillators with the design requirements (6.39) with $\mathcal{A}_i(\phi_i^\infty) = [0, \pi)$ for $i = 1, \ldots, P$. A monotone step interaction function $\Lambda_v(\varphi)$ is constructed to correspond to the desired phase relationship, such as the one illustrated in Figure 6.10, as follows. The sum of scaled and shifted sigmoid functions, such as the error function or the inverse tangent function, can be used to synthesize such a $\Lambda_v(\varphi)$, which is then approximated using a truncated Fourier series expression $\Lambda_v^r(\varphi)$, as in Appendix (B.3). It follows that the corresponding control waveform $v^r(\theta)$ that results in the desired phase pattern can be synthesized using the Fourier coefficients (6.44). The input $v^r(\theta)$ functions as intended as long as the PRC exhibits sufficient higher order harmonics $\{a_0, a_n, b_n\}$ in order for the design (6.39) to be realizable using a waveform with truncated Fourier expansion of order r.

6.4.3 Phase Assignment Examples

In this section, several numerical simulations that verify the technique are presented, as well as a preliminary experimental study involving electrochemical oscillators. First, consider the Hodgkin-Huxley system with the nominal parameters given in Appendix A.1 and PRC shown in Figure 4.2(a), for which the tolerance of $\delta_Z = \langle Z^2 \rangle \cdot 10^{-4} = 7.401 \cdot 10^{-7}$ on the magnitude of included orders of the Fourier expansion results in a truncation at $r = 5$. The monotone step interaction function technique was applied for this system with $P = 3$, $r = 6$, $\{\phi_1^\infty, \phi_2^\infty, \phi_3^\infty\} = \{0, 2\pi/3, 4\pi/3\}$, and $\{\omega_1, \omega_2, \omega_3\} = \{.99\omega, \omega, 1.01\omega\}$ where ω is the natural frequency, with $\Lambda_v^r(\varphi)$ and $v^r(\theta)$ shown in Figures 6.11(a) and 6.11(b), respectively. The desired phase structure stabilizes after about 50 input cycles, as shown in Figure 6.11(a).

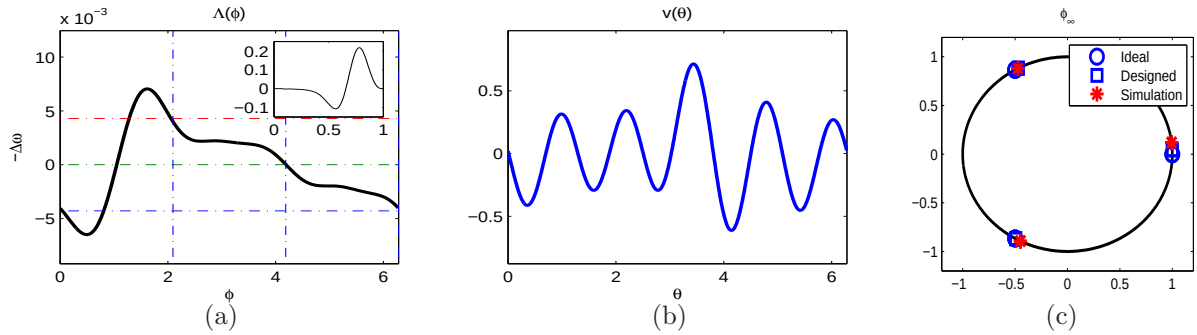

Figure 6.11: (a) Interaction function $\Lambda_v^r(\varphi)$ designed using a $r = 5$ order Fourier series fit to an ideal $\Lambda_v(\varphi)$ designed using the monotone step interaction function technique. Horizontal lines indicate values of $-\Delta\omega_i$, and vertical lines indicated values of ϕ_i^∞. Inset: PRC of Hodgkin-Huxley (HH) System. (b) Input waveform $v(\theta)$ resulting from Fourier inversion of $\Lambda_v^r(\varphi)$. (c) The ideal, designed and actual phase pattern resulting from applying $v(\theta)$ to HH phase models with frequencies at 1.01, 1, and .99 times the natural frequency ω.

An additional numerical experiment can be done to demonstrate that arbitrarily complex phase structures can indeed be created, and that the only limitation arises from the nonlinearity of the system PRC. That is, the number of oscillators whose fixed phase relationship can be exactly specified is limited by the number of significant modes in the Fourier expansion of the PRC, with energy greater than $\delta_Z = \langle Z^2 \rangle \cdot 10^{-4}$, as specified in Section 6.4.2. Consider a collection of theoretical example systems with sawtooth shaped PRCs and frequencies in the neighborhood of $\omega = 2\pi/T$ with $T = 25$. This PRC can be fairly accurately represented using a Fourier series of order 100, as shown in the inset panel in 6.12(a). The numerical simulation shown in Figure 6.12 involves 10 oscillators with a sawtooth PRC and with frequencies uniformly distributed on $[0.995\omega, 1.005\omega]$. By designing the appropriate waveform using the monotone step interaction function method described in Section 6.4.2, it is possible to achieve a splay state, such as in Figure 6.12(c), or an arbitrary phase structure, as shown in Figure 6.12(f). Because the attractive fixed phase of each oscillator in the collection is unique, the desired engineered phase structure arises from any vector of arbitrary initial conditions of the oscillators, and will be robust to disturbances, as well as slight variations in the frequency parameters.

In addition to the simulation in Figure 6.11, the above technique was used to create phase assigned synchronization in two heterogeneous electrochemical oscillators in the laboratory. The experimental setup in Figure 4.6(a) consists of two electrodes that behave as oscillators. Their relative remoteness results in a relatively small potential drop in the electrolyte, and consequently there is no measurable interaction between them [121]. Because of surface heterogeneities, the oscillators typically have about 10-20 mHz frequency difference [226].

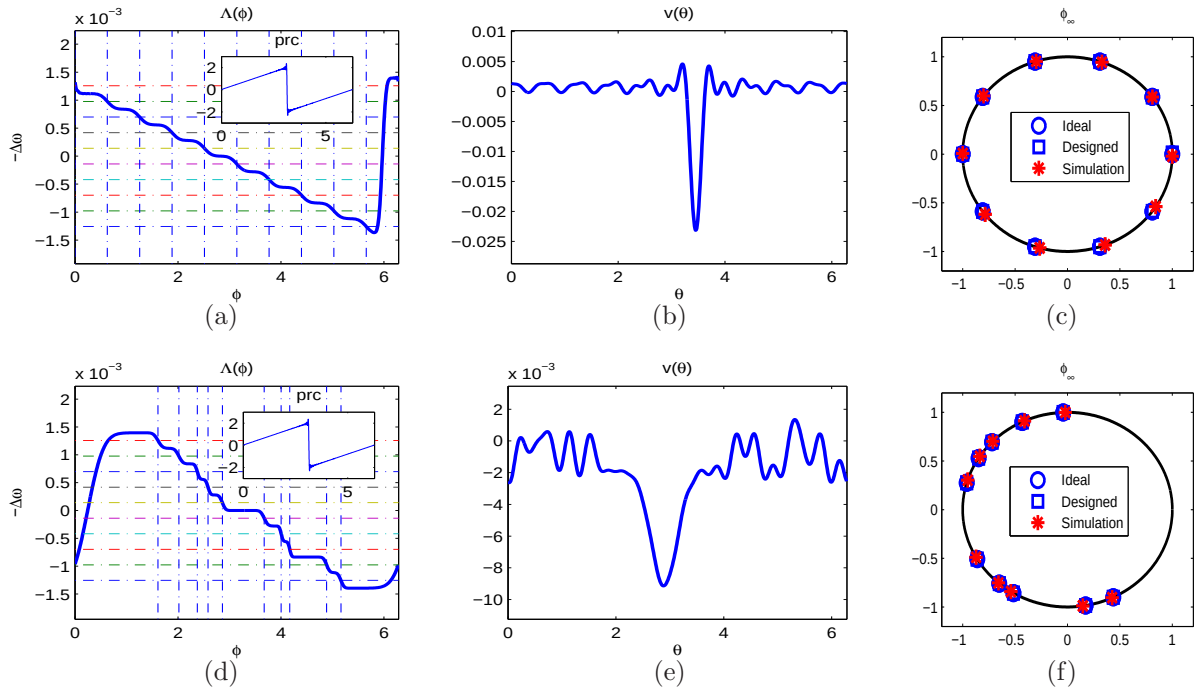

Figure 6.12: (a) Interaction function $\Lambda_v^r(\varphi)$ designed using a $r = 20$ order Fourier series fit to an ideal $\Lambda_v(\varphi)$ designed using the monotone step interaction function technique to correspond to a splay state. Horizontal lines indicate values of $-\Delta\omega_i$, and vertical lines indicated values of ϕ_i^∞. Inset: Sawtooth PRC. (b) Input waveform $v(\theta)$ resulting from Fourier inversion of $\Lambda_v^r(\varphi)$. (c) The ideal, designed and actual phase pattern resulting from applying $v(\theta)$ to sawtooth PRC phase models with frequencies uniformly distributed on $[0.995\omega, 1.005\omega]$, where $\omega = 2\pi/T$ is the natural frequency for a period of $T = 25$. (d) Interaction function designed to correspond to an arbitrarily chosen phase pattern. (e) Input waveform resulting in interaction function in (d). (f) Ideal, designed, and actual phase pattern resulting from application of the waveform (e) to the same collection as in (c).

Two relaxation oscillators with phase response characteristics as shown in Figure 4.6(b) but heterogeneous natural frequencies were entrained to the same frequency with a desired phase difference $\Delta\phi \in [0, 2\pi)$. The PRC and frequency of each was estimated using the method in Section 4.4, and the control was synthesized by using the average of the two PRCs using the monotone step function technique as illustrated in Figure 6.10. Two preliminary experiments shown in Figure 6.13 resulted in rapid entrainment of the oscillators to $\Delta\phi \approx 0$ (in-phase) and $\Delta\phi \approx \pi$ (anti-phase). The in-phase state is relatively easy to engineer, since both oscillators entrain to the input. However, Figure 6.13(a) demonstrates anti-phase synchronization, which confirms that the method above is promising for applications that require efficient phase difference control without the use of any state observations or feedback. The methodology is expected to supersede previous techniques that require real-time control and identical oscillators [190].

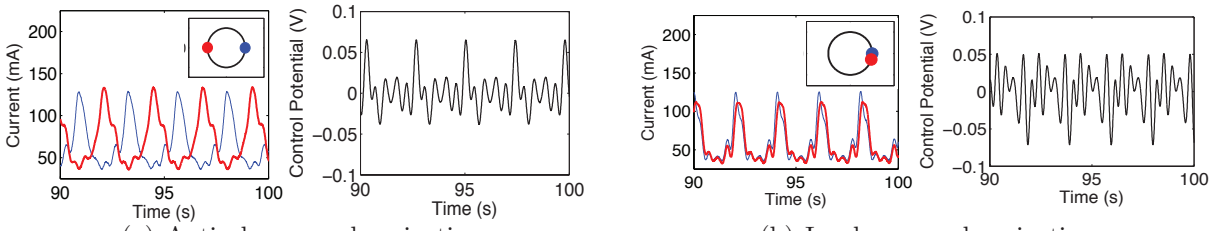

(a) Anti-phase synchronization (b) In-phase synchronization

Figure 6.13: Phase assignment of two electrochemical oscillators. Panel (a) shows anti-phase oscillations, and panel (b) shows phase assignment for in-phase oscillations. In each panel, a snapshot of the phase difference of the two oscillators is shown inset to a plot of current oscillations vs time at left. The applied control signal is shown to the right.

Observe that in the above experiments, the phase structures have all involved orderings of the oscillators with ascending natural frequencies ω_i corresponding to ascending asymptotic phases ϕ_i^∞, as shown in Figure 6.10. These cases satisfy $\mathcal{A}_i(\phi_i^\infty) = [0, \pi)$ for all $i = 1, \ldots, N$, hence only a single input waveform is required to produce the arrangement. However, a non-monotone pattern where phases ϕ_i^∞ are not necessarily ascending for ascending frequencies ω_i, such as that corresponding to the interaction function in Figure 6.9, is possible as well. In that case, a sequence of preliminary input waveforms can be applied to arrange increasing subsets of the oscillators until the desired phase structure is achieved, and then a single waveform suffices to maintain the configuration. Developing an automatic algorithm for generating such waveform sequences remains for future work.

Chapter 7

Conclusion

7.1 Computational Methods for Ensemble Control

In Chapter 2, an accurate, stable, and computationally efficient numerical method for synthesizing minimum norm ensemble controls for finite-dimensional time-varying linear systems is presented. Using the singular value decomposition (SVD) and appropriately conditioning the outcome guarantees accuracy and numerical stability of the method, and leverages the efficiency of widely-used numerical routines. Furthermore, because the SVD is a finite algorithm, the method does not require any additional optimization steps. Its effectiveness is demonstrated for designing controls for a variety of system ensembles and state transfers under various challenging conditions, including complicated state transfers and high-dimensional time-varying dynamics, as well as constraints on the control amplitude.

Chapter 3 extends the results of Chapter 2 to produce a computationally efficient iterative fixed-point method for synthesizing ensemble controls for bilinear systems. Employing successive linear time-varying approximations of the bilinear system dynamics, and the resulting control iterates synthesized using the SVD-based method, yields a consistent, optimization-free algorithm. We have demonstrated its effectiveness for designing controls that accomplish state transfers for bilinear ensemble systems, in particular the Bloch system, and have conducted multiple simulations to illustrate the sensitivity of the method with respect to the chosen discretization parameters and time horizon. This work provides a novel numerical method for designing excitations for the manipulation of quantum spin systems. Further development of this technique will accelerate the quickly broadening scope of ensemble control theory by contributing powerful new tools for solving forefront problems in numerous

fields from neuroscience to quantum computing. Extension of our approach to a universal algorithm for ensemble control of general nonlinear systems, as well as systems involving constraints or stochastic components, can contribute to applications in fields including chemistry, robotics, and medicine.

7.2 Novel Paradigms for Synchronization Engineering

The Chapters 4 through 6 investigate approaches to designing optimal periodic inputs for synchronization of nonlinear oscillators, culminating in a novel technique for locally structuring interactions between the phase dynamics of collections of highly nonlinear oscillators and the input. The key concept is the construction of globally attracting, spatially organized stationary patterns in such oscillator ensembles. Phase model reduction and the ergodic averaging approximation facilitate the use of the calculus of variations to derive optimal entrainment waveforms, and to design synchronizing inputs that establish a desired phase relationship among a collection of nonlinear dynamical oscillating systems without the use of feedback information.

Chapter 5 describes methods for deriving minimum-energy inputs for entrainment of arbitrary oscillators to a desired frequency using weak periodic forcing. We also derive an approximation of the locking region in energy-frequency space for a periodically forced oscillator, called an Arnold tongue. The entrainment of phase-reduced Hodgkin-Huxley neurons is considered as an example problem, and Arnold tongues are computed to evaluate the effectiveness of the derived inputs. The results closely match the theoretical bounds when the weak forcing requirement is fulfilled. The optimal waveforms produce a similar result when applied to the original model, which suggests that optimal entrainment controls derived using a phase model are optimal for the original system, provided the oscillator remains within a neighborhood of its limit cycle. In addition, for many biological and engineered systems, a central function or design goal is to abbreviate the time required to synchronize a rhythmic process to an external forcing signal. This has inspired our theory for deriving the input that effectively minimizes the average transient time required to entrain a phase model, which enables a practical technique for constructing fast entrainment waveforms for general nonlinear oscillators. This result is verified in numerical simulations using the Hodgkin-Huxley neuron model, and in experiments on an oscillatory electrochemical system. The technique

can be applied to any nonlinear oscillator, and requires no knowledge about its initial state. Entrainment is achieved over the minimum number of cycles possible for a given control energy such that phase model approximation and averaging remain valid. In contrast to previous studies on the control of oscillators using phase models, the derivative of the PRC plays an important role in addition to the PRC itself. The methodology is promising for fast re-establishment of entrainment in oscillators that intermittently break phase locking due to environmental or internal effects, such as biological systems with fluctuations in chemical reaction rates due to the small number of molecules in a cell. This methodology is suitable for weak phase resetting, while strong resetting requires control approaches that do not depend on averaging but involve substantial changes to the state of the oscillator.

In addition, a methodology for designing optimal waveforms for subharmonic entrainment, or N:M, entrainment is developed, where M cycles of the oscillator occur for every N control input cycles. Diverse objectives such as minimizing input energy, maximizing the rate of entrainment, and designing the entrainment frequency and control power are considered. In order to characterize the phenomenon of subharmonic entrainment, we also derive an approximation of the Arnold tongues. The entrainment of phase-reduced Hodgkin-Huxley neurons is considered as an example problem, and boundaries of Arnold tongues are computed for various subharmonic entrainment ratios and controls to compare to the theoretical regions. Detailed descriptions and illustrations are provided to connect the behavior of entrained systems to the corresponding Arnold tongues and interaction functions. Simulations to compute actual Arnold tongues are described and carried out for minimum energy subharmonic entrainment controls for single oscillators, and the measurement of entrainment rates of simulations is described and carried out to examine the performance of fast entrainment waveforms. In all cases, the computational results closely correspond to what is predicted by the derived theory. This work provides a comprehensive study of subharmonic entrainment of weakly forced nonlinear oscillators, as well as a practical technique for control synthesis.

In Chapter 6, the approach of considering an ensemble with common phase response curve and varying frequency is justified by a sensitivity analysis of the phase response curve and optimal waveform to variation in model parameters. The results of our simulations suggest that stimuli based on inherent dynamical properties of neural oscillators can result in significant improvement in energy efficiency and performance over traditional pulses both in theory and in practical neural engineering applications. This work provides a basis for evaluating the effectiveness of phase reduction techniques for the control of oscillating systems

with parameter uncertainty. The theory of optimal entrainment of oscillator ensembles is also extended to the case of subharmonic, or N:M entrainment, and the minimum-energy entrainment of large ensembles of oscillators with uncertain parameters is explored. The asymptotic behavior of the ensemble is studied by examining an ensemble Arnold tongue, which characterizes the synchronization properties of oscillator ensembles.

A result of particular note is the ability to design a common periodic input that produces a desired fixed phase relationship in a collection of entrained oscillators. The key feature of this technique is to take advantage of the nonlinearity of the oscillator dynamics, which may be arbitrary as long as they exhibit sufficient nonlinear relaxation for the control design to be realizable. Furthermore, knowledge of the initial state of the oscillators is not required, and control input designs are robust to uncertainty in the parameters of each oscillating system, as well as to disturbances, in a way that can be directly quantified. Most interestingly for applications, switching between synchronization patterns in a collection of oscillators can be as simple as switching between input waveforms that establish and maintain the desired configuration.

7.3 Future Work

The work in Chapters 2 and 2 forms the basis for a new set of numerical methods for quantum control by providing an approach to designing excitations for guidance of quantum spin systems. Future work in this direction will involve investigation of the contractive properties of the relevant integral operator equations to derive theorems characterizing the convergence properties of these algorithms. Another direction is the extension of computational methods for ensemble control to nonlinear systems. Many open questions remain regarding the control of dynamic equations of bilinear form, which govern many widely studied quantum dynamical phenomena. A computationally efficient numerical scheme to synthesize controls for this type of problem will facilitate the improvement of pulse design for NMR, and would be of immediate use to experimentalists.

The optimal synchronization methodology developed in Chapters 4 through 6 bypasses the limitations of present synchronization engineering techniques, such as the requirements of real-time feedback, knowledge of exact initial conditions and a comprehensive model, and

lack of paradigms for constructing multi-scale patterns. The exploration of stable and robust phase structures that can be achieved by external forcing without feedback, and that are robust for each oscillator within an ensemble is compelling, because many of the motivating applications for research into the dynamics of rhythmic systems, including circadian pacemakers and particularly neuronal dynamics, exhibit disturbances, variations, and incomplete models of dynamics, and provide limited state information. An important extension of this work is to generalize synchronization engineering techniques to coevolutionary networks [86], with topologies that adapt in response to the dynamics of interacting network units, by designing adaptive strategies to manipulate fully or partially observable networks given complete or limited feedback. These methods can also be extended to analyze and optimize synchronization in interacting rhythmic systems across different time-scales.

The analytical tools and practical system identification and control methodology developed in this project will be of particular value for neural engineering. For example, the techniques of Chapters 4 through 6 can be used to design stimulus patterns for optimally treating the effects of Parkinson's disease. Parkinson's disease (PD) is a major neurological disorder in terms of prevalence and morbidity. In the U.S. there are 500,000 people with PD, and the socioeconomic burden of PD is set to rise as the elderly population increases. DBS neurostimulation of the is a powerful yet costly treatment that effectively alleviates the burden of advanced PD symptoms, but can induce unwanted effects on working memory and other cognitive functions. Despite the benefits of DBS and its implantation in over 75,000 patients, the optimization of the stimulation waveform to maximize therapeutic effect while minimizing total energy delivery in vivo has not been attempted. Such an advance will prolong the battery life of the implant while reducing unwanted stimulator-induced cognitive deficits. More generally, altering neuronal spiking activity using external stimuli is a subject of active research with the intent of developing therapeutic stimulation procedures for treating neurological conditions such as essential tremor, dystonia, and psychiatric disorders.

Appendix A

Complex Oscillator Models

A.1 Hodgkin-Huxley Neuron Model

The Hodgkin-Huxley model describes the propagation of action potentials in neurons, specifically the squid giant axon, and is used as a canonical example of neural oscillator dynamics [99]. The equations are

$$
\begin{aligned}
c\dot{V} &= I_b + I(t) - \overline{g}_{Na} h (V - V_{Na}) m^3 - \overline{g}_K (V - V_k) n^4 - \overline{g}_L (V - V_L) \\
\dot{m} &= a_m(V)(1-m) - b_m(V) m, \\
\dot{h} &= a_h(V)(1-h) - b_h(V) h, \\
\dot{n} &= a_n(V)(1-n) - b_n(V) n, \\
a_m(V) &= 0.1(V+40)/(1-\exp(-(V+40)/10)), \\
b_m(V) &= 4\exp(-(V+65)/18), \\
a_h(V) &= 0.07\exp(-(V+65)/20), \\
b_h(V) &= 1/(1+\exp(-(V+35)/10)), \\
a_n(V) &= 0.01(V+55)/(1-\exp(-(V+55)/10)), \\
b_n(V) &= 0.125\exp(-(V+65)/80).
\end{aligned}
$$

The variable V is the voltage across the axon membrane, m, h, and n are the ion gating variables, I_b is a baseline current that induces the oscillation, and $I(t)$ is the control input. The units of V and time are millivolts and milliseconds, respectively. Nominal parameters are $V_{Na} = 50$ mV, $V_K = -77$ mV, $V_L = -54.4$ mV, $\overline{g}_{Na} = 120$ mS/cm^2, $\overline{g}_K = 36$ mS/cm^2, $\overline{g}_L = 0.3$ mS/cm^2, $I_b = 10$ μA/cm^2, and $c = 1$ μF/cm^2, for which the period of oscillation is $T = 14.63842 \pm 10^{-5}$ ms, corresponding to frequency $\omega \approx 0.4292$ rad/ms.

A.2 Morris-Lecar Neuron Model

The Morris-Lecar model describes the voltage oscillations in the barnacle giant muscle fiber [159]. The dynamics are given by

$$\begin{aligned} C\dot{V} &= I_b + I(t) + g_{Ca} m_\infty h(V_{Ca} - V) + g_K w(V_k - V) - g_L(V_L - V) \\ \dot{w} &= \phi(w_\infty - w)/\tau_w(V), \end{aligned}$$

$$\begin{aligned} m_\infty(V) &= 0.5(1 + \tanh((V - V_1)/V_2)), \\ w_\infty(V) &= 0.5(1 + \tanh((V - V_3)/V_4)), \\ \tau_\infty(V) = &= 1/\cosh((V - V_3)/(2V_4)). \end{aligned}$$

The variable V is the membrane potential, w is a so-called recovery variable corresponding to the potassium ion conductance, I_b is a baseline current that induces the oscillation, and $I(t)$ is the control input. The units of V are millivolts and the units of time are milliseconds. The nominal parameters are given by $\phi = 0.5$, $I_b = 0.09\mu\text{A/cm}^2$, $V_1 = -0.01\text{mV}$, $V_2 = 0.15\text{mV}$, $V_3 = 0.1\text{mV}$, $V_4 = 0.145\text{mV}$, $g_{Ca} = 1\text{mS/cm}^2$, $V_K = -0.7\text{mV}$, $V_L = -0.5\text{mV}$, $g_K = 2\text{mS/cm}^2$, $g_L = 0.5\text{mS/cm}^2$, $C = 1\mu\text{F/cm}^2$, $V_{Ca} = 1\text{mV}$.

A.3 Hindmarsh-Rose Bursting Neuron Model

The Hindmarsh-Rose model is a generic model of bursting neuron dynamics that is widely used in neuroscience [98]. A slow variable is augmented to the Fitzhugh-Nagumo planar model, which is a reduction of the Hodgkin-Huxley model [67]. The equations are

$$\begin{aligned} \dot{V} &= I_b + I(t) + n - aV^3 + bV^2 - h \\ \dot{n} &= c - dV^2 - n \\ \dot{h} &= r(\sigma(V - V_0) - h) \end{aligned}$$

The non-dimensional variable V is the voltage across the axon membrane, while n and h are fast and slow ion gating variables, respectively, I_b is a baseline current that induces the oscillation, and $I(t)$ is the control input. The units of V are millivolts and the units of time are milliseconds. Nominal dimensionless parameters are $a = 1$, $b = 3$, $c = 1$, $d = 5$,

$r = 0.001$, $\sigma = 4$, $V_0 = -1.6$, and $I_b = 2$, for which a full period of oscillation is $T = 430.7757$, corresponding to angular frequency $\omega \approx 0.0145857$.

A.4 Anodic Dissolution of Nickel in Sulfuric Acid

Complex oscillatory behavior has been shown to arise in an electrochemical apparatus consisting of a collection of nickel electrodes immersed in sulfuric acid [90]. When constant circuit potential $V(t) = V_0$ is applied through a potentiostat, the 1 mm diameter metal wires undergo a dissolution process with variation in the rate, which induces oscillations in the measured currents $i(t)$ of the electrodes [136, 120]. A control signal $\delta V(t)$ can be superimposed onto the potentiostat, so that the circuit potential $V(t) = V_0 + \delta V(t)$ affects the reaction rate of the electrode as a perturbation [95, 119]. The dynamics of potentiostatic nickel dissolution in sulfuric acid can be modeled using a system of differential equations that describe the dynamics of non-dimensionalized potential and chemical concentration variables. It is important to note that although the model does not completely represent the detailed chemistry underlying the oscillatory behavior, it does capture the underlying dynamical behavior [120]. The system equations are given by

$$\begin{aligned}
\dot{E} &= \frac{V - E}{R} - (1-\theta)\left[\frac{C_h e^{E/2}}{1 + C_h e^E} + a e^E\right], \\
\Gamma\dot{\theta} &= (1-\theta)\frac{e^E/2}{1 + C_h e^E} - \theta\frac{b C_h e^2 E}{c C_h + e^E}.
\end{aligned}$$

The variable E is the dimensionless electrode potential, and θ is a dimensionless chemical concentration variable. The circuit potential V and cell resistance R can be adjusted in the experimental apparatus. In synchronization studies, R is fixed while the circuit potential $V(t) = V_0 + \delta V(t)$ is engineered so that V_0 induces an oscillation and $\delta V(t)$ is treated as a control input. The parameter set $\Gamma = 0.01$, $C_h = 1600$, $a = 0.3$, $b = 6 \times 10^{-5}4$, $V_0 = 15$, $R = 20$, and $c = 1 \times 10^{-3}$ results in relaxation oscillations with a period of 13.85.

Appendix B

Interaction functions for subharmonic entrainment

Because the PRC $Z(\theta)$, input waveform $v(\theta)$, and interaction function

$$\Lambda_v^{NM}(\phi) \triangleq \langle Z(M\theta+\phi)v(N\theta)\rangle = \frac{1}{2\pi}\int_0^{2\pi} Z(M\theta+\phi)v(N\theta)\mathrm{d}\theta$$

are all 2π-periodic, they are most conveniently represented using Fourier series, and interaction functions can easily be computed by inspecting the equation 5.3. Let us denote the Fourier series for Z and v by

$$Z(\theta) = \frac{1}{2}a_0 + \sum_{n=1}^{\infty} a_n \cos(n\theta) + \sum_{n=1}^{\infty} b_n \sin(n\theta), \tag{B.1}$$

$$v(\theta) = \frac{1}{2}c_0 + \sum_{n=1}^{\infty} c_n \cos(n\theta) + \sum_{n=1}^{\infty} d_n \sin(n\theta). \tag{B.2}$$

By applying trigonometric angle sum identities and the orthogonality of the Fourier basis, we can obtain $\Lambda_v^{NM}(\varphi)$ by first computing

$$\begin{aligned}\Lambda_v^{NM}(M\varphi) = \frac{a_0c_0}{4} &+ \frac{1}{2}\sum_{j=1}^{\infty}[a_{Mj}\,c_{Nj} + b_{Mj}\,d_{Nj}]\cos(j\varphi)\\ &+ \frac{1}{2}\sum_{j=1}^{\infty}[b_{Mj}\,c_{Nj} - a_{Mj}\,d_{Nj}]\sin(j\varphi),\end{aligned} \tag{B.3}$$

then making the appropriate re-scaling. It is assumed that the integers N and M are coprime. The equation (B.3) leads to the following lemmas:

Lemma 1: Condition for existence of subharmonic entrainment. Given a phase model (4.2) and an input waveform $v(\theta)$, subharmonic (N:M) entrainment to a target frequency $\Omega \neq \omega$ using a forcing frequency $\Omega_f = \frac{N}{M}\Omega$ is possible if and only if $a_{Mj}\, c_{Nj} + b_{Mj}\, d_{Nj} \neq 0$ or $b_{Mj}\, c_{Nj} - a_{Mj}\, d_{Nj} \neq 0$ for at least one $j \in \mathbb{N}$ in (B.3).

Proof: If $a_{Mj}\, c_{Nj} + b_{Mj}\, d_{Nj} = 0$ and $b_{Mj}\, c_{Nj} - a_{Mj}\, d_{Nj} = 0$ for all $j \in \mathbb{N}$, then $\Lambda_v^{NM}(\varphi) \equiv 0$ by (B.3). Therefore if $\Delta\omega = \omega - \Omega \neq 0$, then $\Lambda_v^{NM}(\varphi) + \Delta\omega = 0$ has no solution and (5.5) has no fixed point. Therefore entrainment cannot occur.

Conversely, suppose that N:M entrainment is possible for $\Delta\omega \neq 0$. It follows that $\Lambda_v^{NM}(\varphi) + \Delta\omega = 0$ must have a solution, hence $\Lambda_v^{NM}(\varphi)$ is not identically zero, and therefore $a_{Mj}\, c_{Nj} + b_{Mj}\, d_{Nj} \neq 0$ or $b_{Mj}\, c_{Nj} - a_{Mj}\, d_{Nj} \neq 0$ for at least one $j \in \mathbb{N}$. □

Lemma 2: Continuity of interaction function. Interaction function Λ_v^{NM} is continuous when v is bounded.

Proof: Suppose v is bounded but Λ_v^{NM} in (5.3) is discontinuous at $\phi \in [0, 2\pi)$. Then $\exists\, M > 0$ such that $|v(\theta)| < M \;\; \forall\, \theta \in [0, 2\pi)$, and $\exists\, \sigma > 0$ such that $|\Lambda_v^{NM}(\phi + \frac{\delta}{2}) - \Lambda_v^{NM}(\phi - \frac{\delta}{2})| > \sigma$ $\forall\, \delta \in (0, d)$ for some $d > 0$. Because Z is continuous, it follows that $\forall\, \epsilon > 0$, $\exists\, \delta > 0$ such that $|Z(\theta + \delta) - Z(\theta)| < \epsilon$. Then for arbitrary fixed $\varepsilon > 0$,

$$
\begin{aligned}
0 < \sigma &< |\Lambda_v^{NM}(\phi + \tfrac{\delta}{2}) - \Lambda_v^{NM}(\phi - \tfrac{\delta}{2})| \\
&= \left| \frac{1}{2\pi} \int_0^{2\pi} [Z(M\theta + \phi + \tfrac{\delta}{2}) - Z(M\theta + \phi - \tfrac{\delta}{2})] v(N\theta) \mathrm{d}\theta \right| \\
&\leq \frac{1}{2\pi} \int_0^{2\pi} |Z(M\theta + \phi + \tfrac{\delta}{2}) - Z(M\theta + \phi - \tfrac{\delta}{2})| \cdot |v(N\theta)| \mathrm{d}\theta \\
&\leq \frac{1}{2\pi} \int_0^{2\pi} \varepsilon M \mathrm{d}\theta = \varepsilon M.
\end{aligned}
$$

Therefore $\varepsilon M > \sigma$, and choosing $\varepsilon = \sigma/(2M)$ yields a contradiction. □

References

[1] J. A. Acebron, L. L. Bonilla, C. J. P. Vicente, F. Ritort, and R. Spigler. The Kuramoto model: A simple paradigm for synchronization phenomena. *Reviews Of Modern Physics*, 77(1):137–185, 2005.

[2] Z. Aganovic and Z. Gajic. The successive approximation procedure for finite-time optimal control of bilinear systems. *IEEE Trans. on Automatic Control*, 39(9):1932–1935, 1994.

[3] D. Aharonov, W. van Dam, J. Kempe, Z. Landau, S. Lloyd, and O. Regev. Adiabatic quantum computation is equivalent to standard quantum computation. *SIAM J. on Computing*, 37:166–194, 2007.

[4] R. Albert and A. L. Barabasi. Statistical mechanics of complex networks. *Reviews Of Modern Physics*, 74(1):47–97, 2002.

[5] D. Andrieux and P. Gaspard. Fluctuation theorem and mesoscopic chemical clocks. *J. Chem. Phys.*, 128:154506, 2008.

[6] T. Aprille and T. Trick. A computer algorithm to determine the steady-state response of nonlinear oscillators. *IEEE Transactions on Circuit Theory*, 19(4):354–360, 1972.

[7] V. I. Arnol'd. Small denominators. i. mapping the circle onto itself. *Izvestiya Rossiiskoi Akademii Nauk. Seriya Matematicheskaya*, 25(1):21–86, 1961.

[8] D. Aronson, R. McGehee, I. Kevrekidis, and R. Aris. Entrainment regions for periodically forced oscillators. *Physical Review A*, 33(3):2190–2192, 1986.

[9] P. Ashwin and J. Swift. The dynamics of N weakly coupled identical oscillators. *Journal of Nonlinear Science*, 2(6):69–108, 1992.

[10] N. Bagheri, J. Stelling, and F. J. Doyle. Circadian phase resetting via single and multiple control targets. *PLoS computational biology*, 4(7):e1000104, 2008.

[11] C. Baker, L. Fox, D. Mayers, and K. Wright. Numerical solution of fredholm integral equations of first kind. *The Computer Journal*, 7(2):141–148, 1964.

[12] C. T. H. Baker. *The numerical treatment of integral equations*, volume 13. Clarendon press Oxford, 1977.

[13] A. C. Barnes, R. C. Roberts, N. C. Tien, C. A. Zorman, and P. X. L. Feng. Silicon carbide (sic) membrane nanomechanical resonators with multiple vibrational modes. In *Solid-State Sensors, Actuators and Microsystems Conference (TRANSDUCERS), 2011 16th International*, pages 2614–2617. IEEE, 2011.

[14] S. D. Bartlett, H. de Guise, and B. C. Sanders. Quantum encodings in spin systems and harmonic oscillators. *Phys. Rev. A*, 65(5):052316, 2002.

[15] R. Beals. *Analysis: an introduction*. Cambridge University Press, 2004.

[16] K. Beauchard, J.-M. Coron, and P. Rouchon. Controllability issues for continuous-spectrum systems and ensemble controllability of bloch equations. *Commun. Math. Phys.*, 296:525–557, 2010.

[17] A. Becker and T. Bretl. Optimal motion planning for robust sensorless part orientation. In *2011 International Conference on Intelligent Robots and Systems*, San Francisco, September 2011.

[18] A. Becker and T. Bretl. Approximate steering of a unicycle under bounded model perturbation using ensemble control. *IEEE Trans. on Robotics*, 28(3):580–591, 2012.

[19] A. L. Benabid and P. Pollak. Long-term suppression of tremor by chronic stimulation of the ventral intermediate thalamic nucleus. *Lancet*, 337:403–406, 1991.

[20] J. D. Berke, M. Okatan, J. Skurski, and H. B. Eichenbaum. Oscillatory Entrainment of Striatal Neurons in Freely Moving Rats. *Neuron*, 43:883–896, 2004.

[21] R. E. Best. *Phase-Locaked Loops: Design, Simulation, and Applications*. McGraw-Hill, New York, 1997.

[22] I. Blekhman. *Synchronization in science and technology*. ASME Press translations, New York, 1988.

[23] S. Boccaletti, V. Latora, Y. Moreno, M. Chavez, and D. Hwang. Complex networks: Structure and dynamics. *Physics Reports*, 424(4-5):175–308, 2006.

[24] F. Bolaños. Measurement and analysis of subharmonics and other distortions in compression drivers. volume 1, 2005.

[25] R. W. Brockett. *Finite Dimensional Linear Systems*. John Wiley & Sons, Inc., 1970.

[26] E. Brown, J. Moehlis, and P. Holmes. On the Phase Reduction and Response Dynamics of Neural Oscillator Populations. *Neural Computation*, 16(4):673–715, 2004.

[27] P. Brumer and M. Shapiro. Laser control of molecular processes. *Annu. Rev. Phys. Chem.*, 43:257–282, 1992.

[28] J. Buck. Studies on the firefly. I. The effects of light and other agents on flashing in Photinus pyralis, with special reference to periodicity and diurnal rhythm. *Physiological zoology*, 10(1):45–58, 1937.

[29] C. Cajochen, S. Altanay-Ekici, M. Münch, S. Frey, V. Knoblauch, and A. Wirz-Justice. Evidence that the lunar cycle influences human sleep. *Current Biology*, 2013.

[30] J. Cavanagh, W. J. Fairbrother, A. G. Palmer, and N. J. Skelton. *Protein NMR Spectroscopy*. Academic Press, San Diego, CA, 1996.

[31] M. Chavez, C. Adam, V. Navarro, S. Boccaletti, and J. Martinerie. On the intrinsic time scales involved in synchronization: a data-driven approach. *Chaos: An Interdisciplinary Journal of Nonlinear Science*, 15(2):023904–023904, 2005.

[32] L. Chen, C. Qiu, and HB Huang. Synchronization with on-off coupling: Role of time scales in network dynamics. *Physical Review E*, 79(4):045101, 2009.

[33] X. Chen, A. Ruschhaupt, S. Schmidt, A. del Campo, D. Guéry-Odelin, and J. G. Muga. Fast optimal frictionless atom cooling in harmonic traps: Shortcut to adiabaticity. *Phys. Rev. Lett.*, 104:063002, 2010.

[34] S. Ching, E. N. Brown, and M. A. Kramer. Distributed control in a mean-field cortical network model: implications for seizure suppression. *Phys Rev E Stat Nonlin Soft Matter Phys*, 86(2 Pt 1):021920, 2012.

[35] S. Ching and J. T. Ritt. Control strategies for underactuated neural ensembles driven by optogenetic stimulation. *Front Neural Circuits*, 7:54, 2013.

[36] M. Clayton, R. Sager, and U. Will. In time with the music: The concept of entrainment and its significance for ethnomusicology. In *European meetings in ethnomusicology*, volume 11, pages 3–142, 2005.

[37] J.-M. Coron. *Control and Nonlinearity*. AMS, 1991.

[38] D. Cory, A. Fahmy, and T. Havel. Ensemble quantum computing by nmr spectroscopy. *PNAS*, 94:1634–1639, 1997.

[39] M. D. Crisp. Adiabatic following approximation. *Physical Review A*, 8(4):2128–2135, 1973.

[40] W. J. Cunningham. The growth of subharmonic oscillations. *The Journal of the Acoustical Society of America*, 23:418, 1951.

[41] R. F. Curtain and H. Zwart. *An Introduction to Infinite-Dimensional Linear Systems Theory*. Springer Verlag, 1991.

[42] P. Danzl, A. Nabi, and J. Moehlis. Charge-balanced spike timing control for phase models of spiking neurons. *Discrete and Continuous Dynamical Systems*, 28(4):1413–1435, 2010.

[43] A. S. Daryoush, T. Berceli, R. Saedi, P. R. Herczfeld, and A. Rosen. Theory of subharmonic synchronization of nonlinear oscillators. In *Microwave Symposium Digest, 1989., IEEE MTT-S International*, pages 735–738. IEEE, 1989.

[44] I. Dasanayake and Li J.-S. Charge-balanced minimum-power controls for spiking neuron oscillators. *arXiv:1109.3798*, 2011.

[45] I. Dasanayake and J.-S. Li. Constrained minimum-power control of spiking neuron oscillators. In *IEEE CDC*, pages 3694–3699. IEEE, 2011.

[46] I. Dasanayake and J.-S. Li. Optimal design of minimum-power stimuli for phase models of neuron oscillators. *Phys. Rev. E*, 83:061916, 2011.

[47] I. Dasanayake and J.-S. Li. Charge-balanced time-optimal control for spiking neuron oscillators. In *51st IEEE Conference on Decision and Control*, Maui, Hawaii, December 2012.

[48] A. Demir and J. Roychowdhury. A reliable and efficient procedure for oscillator ppv computation, with phase noise macromodeling applications. *Computer-Aided Design of Integrated Circuits and Systems, IEEE Transactions on*, 22(2):188–197, 2003.

[49] S. Demir, R. Butera, A. DeFranceschi, J. Clark, and J. Byrne. Phase Sensitivity and Entrainment in a Modeled Bursting Neuron. *Biophysical Journal*, 72:579–594, 1997.

[50] J. W. Demmel. *Applied Numerical Linear Algebra*. SIAM, 1997.

[51] A. Destexhe, D. Contreras, T. J. Sejnowski, and M. Steriade. A model of spindle rhythmicity in the isolated thalamic reticular nucleus. *J Neurophysiol*, 72(2):803–18, 1994.

[52] F. Dörfler and F. Bullo. Exploring synchronization in complex oscillator networks. In *IEEE Conference on Decision and Control*, Maui, HI, USA, December 2012.

[53] F. Dörfler and F. Bullo. Synchronization and transient stability in power networks and non-uniform Kuramoto oscillators. 50(3):1616–1642, 2012.

[54] F. Dörfler, M. Chertkov, and F. Bullo. Synchronization in complex oscillator networks and smart grids. *Proceedings of the National Academy of Sciences*, 110(6):2005–2010, 2013.

[55] D. Efimov. Phase resetting control based on direct phase response curve. *Journal of mathematical biology*, 63(5):855–879, 2011.

[56] D. Efimov and T. Raissi. Phase resetting control based on direct phase response curve. In *Preprints of the 8th IFAC Symposium on Nonlinear Control Systems*, pages 332–337, Bologna, September 2010.

[57] D. Efimov, P. Sacré, and R. Sepulchre. Controlling the Phase of an Oscillator: A Phase Response Curve Approach. In *Joint 48th Conference on Decision and Control*, pages 7692–7697, December 2009.

[58] B. Ermentrout. Type I Membranes, Phase Resetting Curves, and Synchrony. *Neural Computation*, 8(5):979–1001, 1996.

[59] B. Ermentrout. *Simulating, Analyzing, and Animating Dynamical Systems: A Guide to XPPAUT for Researchers and Students*. SIAM, 2002.

[60] G. Ermentrout and J. Rinzel. Beyond a pacemaker's entrainment limit: phase walk-through. *American Journal of Physiology - Regulatory, Integrative and Comparative Physiology*, 246(1), 1984.

[61] G. B. Ermentrout. n:m phase-locking of weakly coupled oscillators. *Journal of Mathematical Biology*, 12:327–342, 1981.

[62] R. Brette et. al. Simulation of networks of spiking neurons: A review of tools and strategies. *Journal of Computational Neuroscience*, 23(3):349–398, 2007.

[63] S. Bize et. al. Cold atom clocks and applications. *Journal of Physics B: Atomic, Molecular and Optical Physics*, 38(9):S449, 2005.

[64] X. L. Feng, C. J. White, A. Hajimiri, and M. L. Roukes. A self-sustaining ultrahigh-frequency nanoelectromechanical oscillator. *Nature Nanotechnology*, 3(6):342–346, 2008.

[65] G. Filatrella. Analysis of a power grid using a kuramoto-like model. *Eur. Phys. J. B*, 61:485–491, 2008.

[66] I. Fischer, Y. Liu, and P. Davis. Synchronization of chaotic semiconductor laser dynamics on subnanosecond time scales and its potential for chaos communication. *Physical Review A*, 62, 2000.

[67] R. Fitzhugh. Impulses and physiological states in theoretical models of nerve membrane. *Biophysical Journal*, 1(6):445–466, 1961.

[68] D. B. Forger and D. Paydarfar. Starting, stopping, and resetting biological oscillators: in search of optimum perturbations. *Journal of Theoretical Biology*, 230(4):521–532, 2004.

[69] R. G. Foster and T. Roenneberg. Human responses to the geophysical daily, annual and lunar cycles. *Current Biology*, 18(17):R784–R794, 2008.

[70] H. Fukuda, H. Murase, and I. T. Tokuda. Controlling Circadian Rhythms by Dark-Pulse Perturbations in Arabidopsis thaliana. *Scientific Reports*, 3:1533, 2013.

[71] R. F. Galán, G. B. Ermentrout, and N. N. Urban. Efficient estimation of phase-resetting curves in real neurons and its significance for neural-network modeling. *Physical Review Letters*, 94(15):158101, 2005.

[72] D. H. Gay and W. H. Ray. Identification and control of distributed parameter systems by means of the singular value decomposition. *Chemical Engineering Science*, 50(10):1519–1539, 1995.

[73] F. Geier, S. Becker-Weimann, A. Kramer, and H. Herzel. Entrainment in a model of the mammalian circadian oscillator. *Journal of Biological Rhythms*, 20(1):83–93, 2005.

[74] I. Gelfand and S. Fomin. *Calculus of Variations*. Dover, 2000.

[75] N. A. Gershenfeld and I. L. Chuang. Bulk spin-resonance quantum computation. *Science*, 275:350–356, 1997.

[76] V. Gintautas and A. W. Hübler. Resonant forcing of nonlinear systems of differential equations. *Chaos: An Interdisciplinary Journal of Nonlinear Science*, 18(3):033118, 2008.

[77] L. Glass and M. C. Mackey. *From clocks to chaos: The rhythms of life*. Princeton University Press, 1988.

[78] B. J. Gluckman, H. Nguyen, S. L. Weinstein, and S. J. Schiff. Adaptive electric field control of epileptic seizures. *Journal of Neuroscience*, 21(2):590–600, 2001.

[79] I. Gohberg, S. Goldberg, and M. A. Kaashoek. *Basic Classes of Linear Operators*. Birkhäuser Verlag, Boston, MA, 2003.

[80] L. Good. Control of synchronization of brain dynamics leads to control of epileptic seizures in rodents. *International Journal of Neural Systems*, 19(3):173–196, 2009.

[81] J. J. Gooley, S. M. Rajaratnam, G. C. Brainard, R. E. Kronauer, C. A. Czeisler, and S. W. Lockley. Spectral responses of the human circadian system depend on the irradiance and duration of exposure to light. *Science Translational Medicine*, 2(31):31–33, 2010.

[82] W. Govaerts and B. Sautois. Computation of the Phase Response Curve: A Direct Numerical Approach. *Neural Computation*, 18(4):817–847, 2006.

[83] A. Granada, R. M. Hennig, B. Ronacher, A. Kramer, and H. Herzel. Phase response curves: elucidating the dynamics of coupled oscillators. *Methods in Enzymology*, 454:1–27, 2009.

[84] A. E. Granada and H. Herzel. How to achieve fast entrainment? the timescale to synchronization. *PLoS One*, 4(9):e7057, 2009.

[85] R. A. Gray. Termination of spiral wave breakup in a fitzhugh-nagumo model via short and long duration stimuli. *Chaos*, 12(3):941–951, 2002.

[86] T. Gross and B. Blasius. Adaptive coevolutionary networks: a review. *J. R. Soc. Interface*, 5:259, 2008.

[87] M. Guevara and L. Glass. Phase Locking, Period Doubling Bifurcations and Chaos in a Mathematical Model of a Periodically Driven Oscillator. *Journal of Mathematical Biology*, 14:1–23, 1982.

[88] R. Gutiérrez, A. Amann, S. Assenza, J. Gómez-Gardenes, V. Latora, and S. Boccaletti. Emerging meso-and macroscales from synchronization of adaptive networks. *Physical Review Letters*, 107(23):234103, 2011.

[89] W. Hackbusch. *Integral equations: theory and numerical treatment*, volume 120. Springer, 1995.

[90] D. Haim, O. Lev, L. M. Pismen, and M. Sheintuch. Modeling periodic and chaotic dynamics in anodic nickel dissolution. *The Journal of Physical Chemistry*, 96(6):2676–2681, 1992.

[91] P. Hansen. Computation of the singular value expansion. *Computing*, 40(3):185–199, 1988.

[92] P. C. Hansen. Numerical tools for analysis and solution of fredholm integral equations of the first kind. *Inverse Problems*, 8(6):849–872, 1992.

[93] F. Hanson. Comparative studies of firefly pacemakers. *Federation Proceedings*, 38(8):2158–2164, 1978.

[94] R. J. Hanson. Numerical method for solving fredholm integral equations of the first kind using singular values. *SIAM J. Numerical Analysis*, 8(3):616–622, 1971.

[95] T. Harada, H. Tanaka, M. Hankins, and I. Kiss. Optimal waveform for the entrainment of a weakly forced oscillator. *Physical Review Letters*, 105(8), 2010.

[96] S. Hata, K. Arai, R. F. Galán, and H. Nakao. Optimal phase response curves for stochastic synchronization of limit-cycle oscillators by common poisson noise. *Physical Review E*, 84(1):016229, 2011.

[97] E. D. Herzog. Neurons and networks in daily rhythms. *Nat. Rev. Neurosci.*, 8(10):790–802, 2007.

[98] J. L. Hindmarsh and R. M. Rose. A model of neuronal bursting using three coupled first order differential equations. *Proceedings of the Royal society of London. Series B. Biological sciences*, 221(1222):87–102, 1984.

[99] A. Hodgkin and A. Huxley. A quantitative description of membrane current and its application to conduction and excitation in nerve. *The Journal of Physiology*, 117(4), 1952.

[100] E. P. Hofer and B. Tibken. An iterative method for the finite-time bilinear-quadratic control problem. *J. Optimization Theory and Applications*, 57(3):411–427, 1988.

[101] L. Hofmann, M. Ebert, P. A. Tass, and C. Hauptmann. Modified pulse shapes for effective neural stimulation. *Frontiers in Neuroengineering*, 4, 2011.

[102] C. J. Honey, R. Kötter, M. Breakspear, and O. Sporns. Network structure of cerebral cortex shapes functional connectivity on multiple time scales. *Proceedings of the National Academy of Sciences*, 104(24):10240–10245, 2007.

[103] H. Hong and M. Y. Choi. Synchronization on small-world networks. *Physical Review E*, 65:026139(5), 2002.

[104] F. Hoppensteadt and E. Izhikevich. *Weakly connected neural networks*. Springer-Verlag, New Jersey, 1997.

[105] F. Hoppensteadt and E. Izhikevich. Oscillatory Neurocomputers with Dynamic Connectivity. *Physical Review Letters*, 82(14), 1999.

[106] F. C. Hoppensteadt and E. M. Izhikevich. Pattern recognition via synchronization in phase-locked loop neural networks. *IEEE Transactions On Neural Networks*, 11(3):734–738, 2000.

[107] F. C. Hoppensteadt and E. M. Izhikevich. Synchronization of laser oscillators, associative memory, and optical neurocomputing. *Physical Review E*, 62(3):4010–4013, 2000.

[108] J. Hunter and J. Milton. Amplitude and Frequency Dependence of Spike Timing: Implications for Dynamic Regulation. *Journal of Neurophysiology*, 90:387–394, 2003.

[109] E. Izhikevich. *Dynamical systems in neuroscience*. Neuroscience. MIT press, 2007.

[110] E. Izhikevich and Y. Kuramoto. Weakly Coupled Oscillators. In *Encyclopedia of mathematical physics*. Elsevier, 2006.

[111] E. M. Izhikevich. Neural excitability, spiking and bursting. *Int. J. Bifurcat. Chaos.*, 10(6):1171–1266, 2000.

[112] E. M. Izhikevich. Which model to use for cortical spiking neurons? *IEEE Transactions On Neural Networks*, 15:1063–1070, 2004.

[113] W. Kelley and A. Peterson. *The Theory of Differential Equations, Classical and Qualitative*. Pearson, 2004.

[114] H. Khalil. *Nonlinear Systems*. Prentice Hall, 3 edition, 2002.

[115] N. Khaneja, C. Kehlet, S. J. Glaser, and N. Nielsen. Composite dipolar recoupling: Anisotropy compensated coherence transfer in solid-state nuclear magnetic resonance. *Journal of Chemical Physics*, 124:114503, 2006.

[116] I. Z. Kiss and J. L. Hudson. Phase synchronization and suppression of chaos through intermittency in forcing of an electrochemical oscillator. *Physical Review E*, 64(4):046215, 2001.

[117] I. Z. Kiss, M. Quigg, S.-H. C. Chun, H. Kori, and J. L. Hudson. Characterization of synchronization in interacting groups of oscillators: Application to seizures. *Biophys. J.*, 94(3):1121–1130, 2008.

[118] I. Z. Kiss, M. Quigg, S. H. C. Chun, H. Kori, and J. L. Hudson. Characterization of synchronization in interacting groups of oscillators: application to seizures. *Biophysical Journal*, 94(3):1121–1130, 2008.

[119] I. Z. Kiss, C. G. Rusin, H. Kori, and J. L. Hudson. Engineering complex dynamical structures: sequential patterns and desynchronization. *Science*, 316(5833):1886–1889, 2007.

[120] I. Z. Kiss, W. Wang, and J. L. Hudson. Experiments on arrays of globally coupled periodic electrochemical oscillators. *J. Phys. Chem. B*, 103:11433–11444, 1999.

[121] I. Z. Kiss, Y. Zhai, and J. Hudson. Emerging coherence in a population of chemical oscillators. *Science*, 296:1676–1678, 2002.

[122] I. Z. Kiss, Y. M. Zhai, and J. L. Hudson. Predicting mutual entrainment of oscillators with experiment-based phase models. *Phys. Rev. Lett.*, 94(24):248301, 2005.

[123] H. W. Knobloch, A. Isidori, and D. Flockerzi. *Topics in control theory*. Birkh auser-Verlag, 1993.

[124] K. Kobzar, B. Luy, N. Khaneja, and S. J. Glaser. Pattern pulses: design of arbitary excitation profiles as a function of pulse amplitude and offset. *J. Magn. Reson.*, 173:229–235, 2005.

[125] K. Kobzar, T. E. Skinner, N. Khaneja, S. J. Glaser, and B. Luy. Exploring the limits of broadband excitation and inversion pulses. *J. Magnetic Resonance*, 170(2):236–243, 2004.

[126] H. Kori, C. G. Rusin, I. Z. Kiss, and J. L. Hudson. Synchronization engineering: Theoretical framework and application to dynamical clustering. *Chaos*, 18(2):026111, 2008.

[127] I. Kornfeld, S. Fomin, and Y. Sinai. *Ergodic theory: Differentiable Dynamical Systems*, volume 245 of *Grund. Math. Wissens.* Springer-Verlag, 1982.

[128] B. Kralemann, L. Cimponeriu, M. Rosenblum, A. Pikovsky, and R. Mrowka. Phase dynamics of coupled oscillators reconstructed from data. *Physical Review E*, 77(6):066205, 2008.

[129] D. J. Kriellaars, R. M. Brownstone, B. R. Noga, and L. M. Jordan. Mechanical entrainment of fictive locomotion in the decerebrate cat. *Journal of neurophysiology*, 71(6):2074–2086, 1994.

[130] A. M. Kuncel and W. M. Grill. Selection of stimulus parameters for deep brain stimulation. *Clinical Neurophysiology*, 115:2431–2441, 2004.

[131] Y. Kuramoto. *Chemical Oscillations, Waves, and Turbulence*. Springer, New York, 1984.

[132] H. Kwakernaak. Robust control and h_∞-optimization. *Automatica*, 29(2):255–273, 1993.

[133] G. Lajoie and E. Shea-Brown. Shared inputs, entrainment, and desynchrony in elliptic bursters: from slow passage to discontinuous circle maps. *SIAM Journal on Applied Dynamical Systems*, 10(4):1232–1271, 2011.

[134] E. W. Large. Modeling beat perception with a nonlinear oscillator. In *Proceedings of the 18th Annual Conference of the Cognitive Science Society*, page 420, 1996.

[135] A. E. Leanhardt, T. A. Pasquini, M. Saba, A. Schirotzek, Y. Shin, D. Kielpinski, D. E. Pritchard, and W. Ketterle. Cooling Bose-Einstein condensates below 500 Picokelvin. *Science*, 301(5639):1513–1515, 2003.

[136] O. Lev, A. Wolfberg, L. M. Pismen, and M. Sheintuch. The structure of complex behavior in anodic nickel dissolution. *Journal of Phys. Chem.*, 93:1661–1666, 1989.

[137] J.-S. Li. *Control of Inhomogeneous Ensembles*. PhD thesis, Harvard University, Cambridge, MA, 2006.

[138] J.-S. Li. A new perspective on control of uncertain complex systems. In *Joint 48th IEEE Conference on Decision and Control*, Shanghai, China, Dec. 2009.

[139] J.-S. Li. Ensemble control of finite-dimensional time-varying linear systems. *IEEE Trans. Autom. Control*, 56:345–357, 2011.

[140] J.-S. Li and N. Khaneja. Control of inhomogeneous quantum ensembles. *Phys. Rev. A*, 73:030302, 2006.

[141] J.-S. Li and N. Khaneja. Ensemble control of linear systems. In *46th IEEE Conference on Decision and Control*, pages 3768–3773. IEEE, 2007.

[142] J.-S. Li and N. Khaneja. Ensemble control of bloch equations. *IEEE Trans. Autom. Control*, 54:528–536, 2009.

[143] J.-S. Li, J. Ruths, and D. Stefanatos. A pseudospectral method for optimal control of open quantum systems. *J. Chem. Phys.*, 131:164110, 2009.

[144] J.-S. Li, J. Ruths, T.-Y. Yu, H. Arthanari, and G. Wagner. Optimal pulse design in quantum control: A unified computational method. *Proc. Nat. Acad. Sci.*, 108(5):1879–1884, 2011.

[145] A. M. Lozano and H. Eltahawy. How does dbs work? *Suppl. Clin. Neurophysiol.*, 57:733–736, 2004.

[146] D. Luenberger. *Optimization by Vector Space Methods.* John Wiley & Sons, Inc., 1969.

[147] H. Mabuchi and N. Khaneja. Principles and applications of control in quantum systems. *International Journal of Robust and Nonlinear Control*, 15:184505, 2008.

[148] P. Maffezzoni, D. D'Amore, S. Daneshgar, and MP Kennedy. Estimating the locking range of analog dividers through a phase-domain macromodel. In *Circuits and Systems (ISCAS), Proceedings of 2010 IEEE International Symposium on*, pages 1535–1538. IEEE, 2010.

[149] I. Malkin. *Methods of Poincare and Liapunov in the theory of nonlinear oscillations.* Gostexizdat, Moscow, 1949.

[150] W. R. Mann. Mean value methods in iteration. *Proceedings of the American Mathematical Society*, 4(3):506–510, 1953.

[151] S. C. Manrubia, A. S. Mikhailov, and D. H. Zanette. *Emergence of Dynamical Order: Synchronization Phenomena in Complex Systems.* World Scientific, Singapore, 2004.

[152] W. J. Marks. Deep brain stimulation for dystonia. *Curr. Treat. Options Neurol.*, pages 237–243, 2005.

[153] M. M. McCarthy, C. Moore-Kochlacs, X. Gu, E. S. Boyden, X. Han, and N. Kopell. Striatal origin of the pathologic beta oscillations in parkinson's disease. *Proc Natl Acad Sci U S A*, 108(28):11620–11625, 2011.

[154] J. Meijer, C. Colwell, J. Rohling, T. Houben, and S. Michel. Dynamic neuronal network organization of the circadian clock and possible deterioration in disease. *Progress in Brain Research*, 199:143–162, 2012.

[155] D. R. Merril, M. Bikson, and J. G. R. Jefferys. Electrical stimulation of excitable tissue: Design of efficacious and safe protocols. *Journal of Neuroscience Methods*, 141:717–198, 2005.

[156] M. Mirrahimi. Controllability of quantum harmonic oscillators. *IEEE Trans. Automatic Control*, 49(5):745–747, 2004.

[157] H. Moehlis, E. Brown, and H. Rabitz. Optimal inputs for phase models of spiking neurons. *Journal of Computational and Nonlinear Dynamics*, 1:358–367, 2006.

[158] R. R. Mohler. *Bilinear control processes: with applications to engineering, ecology, and medicine*. Academic Press, 1973.

[159] C. Morris and H. Lecar. Voltage oscillations in the barnacle giant muscle fiber. *Biophysical Journal*, 35(1), 1981.

[160] A. Nabi and J. Moehlis. Charge-balanced optimal inputs for phase models of spiking neurons. In *2009 ASME Dynamic Systems and Control Conference*, Hollywood, CA, October 2009.

[161] A. Nabi and J. Moehlis. Single input optimal control for globally coupled neuron networks. *J. Neural Eng.*, 8:065008, 2011.

[162] M. T. Nair. *Functional analysis: A first course*. Prentice Hall of India, 2002.

[163] S. Nakata, K. Miyazaki, S. Izuhara, H. Yamaoka, and D. Tanaka. Arnold Tongue of Electrochemical Nonlinear Oscillators. *Journal of Physical Chemistry A*, 113:6876–6879, 2009.

[164] T. Z. Naqvi and D. C. Winter. Optimization of pacemaker settings, February 2012. US Patent 8,112,150.

[165] T. I. Netoff, C. D. Acker, J. C. Bettencourt, and J. A. White. Beyond two-cell networks: experimental measurement of neuronal responses to multiple synaptic inputs. *Journal Of Computational Neuroscience*, 18(3):287–295, 2005.

[166] T. Nishikawa, N. Gulbahce, and A. E. Motter. Spontaneous Reaction Silencing in Metabolic Optimization. *PLoS Computational Biology*, 4(12):e1000236, 2008.

[167] J. W. Noris. Nonlinear dynamical behavior of a moving voice coil. In *105th AES Convention, San Francisco*, volume 1, 1988.

[168] S. Nozaradan, I. Peretz, M. Missal, and A. Mouraux. Tagging the neuronal entrainment to beat and meter. *The Journal of Neuroscience*, 31(28):10234–10240, 2011.

[169] E. J. Nyström. Über die praktische auflösung von integralgleichungen mit anwendungen auf randwertaufgaben. *Acta Mathematica*, 54(1):185–204, 1930.

[170] S. Ohtahara and Y. Yamatogi. Epileptic encephalopathies in early infancy with suppression-burst. *J Clin Neurophysiol*, 20(6):398–407, 2003.

[171] L. Organ, I. Z. Kiss, and J. L. Hudson. Bursting oscillations during metal electrodissolution: Experiments and model. *J Phys Chem B*, 107:6648–6659, 2003.

[172] H. Osinga and J. Moehlis. Continuation-based computation of global isochrons. *SIAM Journal on Applied Dynamical Systems*, 9(4):1201–1228, 2010.

[173] J. Pauly, P. Le Roux, D. Nishimura, and A. Macovski. Parameter relations for the shinnar-le roux selective excitation pulse design algorithm. *IEEE Trans. Medical Imaging*, 10:53–65, 1991.

[174] D. B. Percival. *Spectral analysis for physical applications*. Cambridge University Press, 1993.

[175] A. Peressini, F. Sullivan, and J. Uhl. *Mathematics of Nonlinear Programming*. Springer, 2000.

[176] L. Perko. *Differential equations and dynamical systems*. Texts in applied mathematics. Springer, 2 edition, 1990.

[177] J. S. Perlmutter and J. W. Wink. Deep Brain Stimulation. *Annu. Rev. Neurosci.*, 29:229–257, 2006.

[178] A. Pikovsky, M. Rosenblum, and J. Kurths. *Synchronization: A Universal Concept in Nonlinear Science*. Cambridge University Press, 2001.

[179] H. M. Pinsker. Aplysia Bursting Neurons as Endogenous Oscillators. I. Phase-Response Curves for Pulsed Inhibitory Synaptic Input. *J. Neurophysiology*, 40(3):065008, 2011.

[180] A. J. Preyer and R. J. Butera. Neuronal Oscillators in Aplysia californica that Demonstrate Weak Coupling In Vitro. *Physical Review Letters*, 95:138103, 2005.

[181] S. Prössdorf and B. Silbermann. Numerical analysis for integral and related operator equations. *Operator theory*, 52:5–534, 1991.

[182] B. Pryor. Fourier decompositions and pulse sequence design algorithms for nuclear magnetic resonance in inhomogeneous fields. *Journal of Chemical Physics*, 125:194111, 2006.

[183] B. Pryor and N. Khaneja. Fourier methods for control of inhomogeneous quantum systems. In *46th IEEE Conference on Decision and Control*, pages 6340–6345, New Orleans, 2007.

[184] J. Qi and J.-S. Li. Ensemble controllability of time-invariant linear systems. In *52nd IEEE Conference on Decision and Control*, Florence, Italy, December 2013.

[185] J. Qi, A. Zlotnik, and J.-S. Li. Optimal ensemble control of stochastic time-varying linear systems. *Systems & Control Letters*, 62(11):1057–1064, 2013.

[186] M. G. Rosenblum, A. S. Pikovsky, and J. Kurths. Phase synchronization of chaotic oscillators. *Physical Review Letters*, 76(11):1804–1807, 1996.

[187] D. Rosenfeld and Y. Zur. Design of adiabatic selective pulses using optimal control theory. *Magn. Reson. Mde.*, 36:401–409, 1996.

[188] J. E. Rubin and D. Terman. High frequency stimulation of the subthalamic nucleus eliminates pathological thalamic rhythmicity in a computational model. *J Comput Neurosci*, 16(3):211–235, 2004.

[189] C. G. Rusin, I. Z. Kiss, H. Kori, and J. L. Hudson. Framework for engineering the collective behavior of complex rhythmic systems. *Industrial & Engineering Chemistry Research*, 48(21):9416–9422, 2009.

[190] C. G. Rusin, H. Kori, I. Z. Kiss, and J. L. Hudson. Synchronization engineering: tuning the phase relationship between dissimilar oscillators using nonlinear feedback. *Philosophical Transactions of the Royal Society A-Mathematical Physical And Engineering Sciences*, 368(1918):2189–2204, 2010.

[191] J. Ruths and J.-S. Li. Optimal ensemble control of open quantum systems with a pseudospectral method. In *49th IEEE Conference on Decision and Control*, pages 3008–3013, Atlanta, 2011.

[192] J. Ruths, A. Zlotnik, and J.-S. Li. Convergence of a pseudospectral method for optimal control of complex dynamical systems. In *50th IEEE Conference on Decision and Control*, page 1039, Orlando, 2011.

[193] P. Salamon, K. H. Hoffmann, Y. Rezek, and R. Kosloff. Maximum work in minimum time from a conservative quantum system. *Phys. Chem. Chem. Phys.*, 11:1027–1032, 2009.

[194] C. Schäfer, M.G. Rosenblum, J. Kurths, and H.H. Abel. Heartbeat synchronized with ventilation. *Nature*, 392:239–240, 1998.

[195] M. J. Schaus and J. Moehlis. On the response of neurons to sinusoidal current stimuli: Phase response curves and phase-locking. In *Proceedings of the 45th IEEE Conference on Decision & Control*, pages 2376–2381, San Diego, CA, December 2006.

[196] S. Schiff. Controlling chaos in the brain. *Nature*, 370:615–620, 1994.

[197] A. Schweiger. *Modern Pulsed and Continuous Wave Electron Spin Resonance*. Wiley, London, 1990.

[198] K. Serkh and D. B. Forger. Optimal schedules of light exposure for rapidly correcting circadian misalignment. *PLoS Comput. Biol.*, 10(4):e1003523, 2014.

[199] W. E. Sherwood and J. Guckenheimer. Dissecting the phase response of a model bursting neuron. *SIAM Journal on Applied Dynamical Systems*, 9(3):659–703, 2010.

[200] Q. Shi and E. Geva. Stimulated raman adiabatic passage in the presence of dephasing. *Journal of Chemical Physics*, 119(22):11773–11787, 2003.

[201] A. Sirota, S. Montgomery, S. Fujisawa, Y. Isomura, M. Zugaro, and G. Buzsáki. Entrainment of neocortical neurons and gamma oscillations by the hippocampal theta rhythm. *Neuron*, 60:683–697, 2008.

[202] M. A. St. Hilaire, J. J. Gooley, S. B. S. Khalsa, R. E. Kronauer, C. A. Czeisler, and S. W. Lockley. Human phase response curve to a 1 h pulse of bright white light. *The Journal of Physiology*, 2012.

[203] P. B. Stark and R. L. Parker. Bounded-variable least-squares: an algorithm and applications. *Computational Statistics*, 10:129–129, 1995.

[204] D. Stefanatos and J.-S. Li. Frictionless atom cooling in harmonic traps: A time-optimal approach. *Physical Review A*, 82:063422, 2010.

[205] D. Stefanatos and J.-S. Li. Minimum-time frictionless atom cooling in harmonic traps. *SIAM Journal on Control and Optimization*, 49:2440–2462, 2011.

[206] D. Stefanatos and J.-S. Li. Minimum-time quantum transport with bounded trap velocity. arXiv:1107.1691v1, July 2011.

[207] M. L. Steyn-Ross, D. A. Steyn-Ross, and J. W. Sleigh. Modelling general anaesthesia as a first-order phase transition in the cortex. *Prog Biophys Mol Biol*, 85(2-3):369–85, 2004.

[208] D. Storti and R.H. Rand. Subharmonic entrainment of a forced relaxation oscillator. *International journal of non-linear mechanics*, 23(3):231–239, 1988.

[209] D. J. Strauss, W. Delb, R. D'Amelio, and P. Falkai. Neural synchronization stability in the tinnitus decompensation. In *Neural Engineering, 2005. Conference Proceedings. 2nd International IEEE EMBS Conference on*, pages 186–189. IEEE, 2005.

[210] S. H. Strogatz. From Kuramoto to Crawford: exploring the onset of synchronization in populations of coupled oscillators. *Physica D*, 143(1-4):1–20, 2000.

[211] K. Takano, M. Motoyoshi, and M. Fujishima. 4.8 ghz cmos frequency multiplier with subharmonic pulse-injection locking. In *Solid-State Circuits Conference, 2007. ASSCC'07. IEEE Asian*, pages 336–339. IEEE, 2007.

[212] P. Tass, M. G. Rosenblum, J. Weule, J. Kurths, A. Pikovsky, J. Volkmann, A. Schnitzler, and H. J. Freund. Detection of n:m phase locking from noisy data: application to magnetoencephalography. *Physical Review Letters*, 81(15):3291–3294, 1998.

[213] P. A. Tass. *Phase Resetting in Medicine and Biology. Stochastic Modeling and Data Analysis*. Springer, Berlin, 1999.

[214] P. A. Tass. A model of desynchronizing deep brain stimulation with a demand-controlled coordinated reset of neural subpopulations. *Biol. Cybern*, 89:81–88, 2003.

[215] P. A. Tass, I. Adamchic, H. J. Freund, T. von Stackelberg, and C. Hauptmann. Counteracting tinnitus by acoustic coordinated reset neuromodulation. *Restorative neurology and neuroscience*, 30(2):137–159, 2012.

[216] D. Terman, J. E. Rubin, A. C. Yew, and C. J. Wilson. Activity patterns in a model for the subthalamopallidal network of the basal ganglia. *J Neurosci*, 22(7):2963–2976, 2002.

[217] I. T. Tokuda, S. Jain, I. Z. Kiss, and J. L. Hudson. Inferring phase equations from multivariate time series. *Physical Review Letters*, 99(6):64101, 2007.

[218] K. Turitsyn, P. Sulc, S. Backhaus, and M. Chertkov. Options for control of reactive power by distributed photovoltaic generators. *Proceedings of the IEEE*, 99(6):1063–1073, 2011.

[219] P. J. Uhlhaas and W. Singer. Neural synchrony in brain disorders: relevance for cognitive dysfunctions and pathophysiology. *Neuron*, 52(1):155–168, 2006.

[220] H. Ukai, T. J. Kobayashi, M. Nagano, K.-H. Masumoto, M. Sujino, T. Kondo, K. Yagita, Y. Shigeyoshi, and H. R. Ueda. Melanopsin-dependent photo-perturbation reveals desynchronization underlying the singularity of mammalian circadian clocks. *Nature Cell Biology*, 9(11):1327–1334, 2007.

[221] G. Ullah. Tracking and control of neuronal Hodgkin-Huxley dynamics. *Physical Review E*, 79:040901(R), 2009.

[222] B. van Keulen. *H_∞-Control for Distributed Parameter Systems: A State-Space Approach*. Birkh auser Boston, 1993.

[223] C. Vogel. Optimal choice of a truncation level for the truncated svd solution of linear first kind integral equations when data are noisy. *SIAM journal on numerical analysis*, 23(1):109–117, 1986.

[224] A. M. Vosko, C. S. Colwell, and A. Y. Avidan. Jet lag syndrome: circadian organization, pathophysiology, and management strategies. *Nature*, 2:187–198, 2010.

[225] M. Wacker and H. Witte. On the stability of the n: m phase synchronization index. *Biomedical Engineering, IEEE Transactions on*, 58(2):332–338, 2011.

[226] M. Wickramasinghe, E. M. Mrugacz, and I. Z. Kiss. Dynamics of electrochemical oscillators with electrode size disparity: asymmetrical coupling and anomalous phase synchronization. *Phys. Chem. Chem. Phys.*, 13:15483, 2011.

[227] A. T. Winfree. Biological rhythms and the behavior of populations of coupled oscillators. *Journal of Theoretical Biology*, 16(1):15–42, 1967.

[228] A. T. Winfree. *The Geometry of Biological Time*. Springer-Verlag, New York, 1980.

[229] Y. Yao, V. Colao, G. Marino, and H.-K. Xu. Implicit and explicit algorithms for minimum-norm fixed points of pseudocontractions in hilbert spaces. *Taiwanese Journal of Mathematics*, 16(4):1489–1506, 2012.

[230] M. Zalalutdinov, K. Aubin, A. Zehnder, R. Hand, H. Craighead, J. Parpia, and B. Houston. Frequency entrainment for micromechanical oscillator. *Applied Physics Letters*, 83(16):3281–3283, 2003.

[231] A. Zarroug, P. S. Hall, and M. Cryan. Active antenna phase control using subharmonic locking. *Electronics Letters*, 31(11):842–843, 1995.

[232] Y. Zhai, I. Z. Kiss, H. Kori, and J. L. Hudson. Desynchronization and clustering with pulse stimulations of coupled electrochemical relaxation oscillators. *Physica D*, 239(11):848–856, 2010.

[233] Y. Zhai, I. Z. Kiss, P. A. Tass, and J. L. Hudson. Desynchronization of coupled electrochemical oscillators with pulse stimulations. *Physical Review E*, 71:065202, 2005.

[234] A. Zlotnik. http://appliedmath.engineering.wustl.edu/research/ensemble-control/.

[235] A. Zlotnik, Y. Chen, I. Z. Kiss, H.-A. Tanaka, and J.-S. Li. Optimal waveform for fast entrainment of weakly forced nonlinear oscillators. *Phys. Rev. Lett.*, 111:024102, Jul 2013.

[236] A. Zlotnik and J. Li. Optimal asymptotic entrainment of phase-reduced oscillators. In *2011 ASME Dynamic Systems and Control Conference*, volume 1, pages 479–484, Arlington, VA, October 2011.

[237] A. Zlotnik and J.-S. Li. Iterative Ensemble Control Synthesis for Bilinear Systems. In *51st IEEE Conference on Decision and Control*, pages 3484–3489, Maui, Hawaii, December 2012.

[238] A. Zlotnik and J.-S. Li. Optimal entrainment of neural oscillator ensembles. *J. Neural Eng.*, 9(4):046015, 2012.

[239] A. Zlotnik and J.-S. Li. Synthesis of Optimal Ensemble Controls for Linear Systems using the Singular Value Decomposition. In *2012 American Control conference*, pages 5849–5854, Montreal, June 2012.

[240] A. Zlotnik and J.-S. Li. Optimal subharmonic entrainment. *arXiv:1401.1863*, 2014.

Vita

Anatoly Zlotnik

Degrees

Ph.D. Systems Science & Mathematics, August 2014
M.S. Applied Mathematics, August 2009
M.S. Systems & Control Engineering, August 2006
B.S. Magna Cum Laude, Systems & Control Engineering, May 2006

Publications

A. Zlotnik, Y. Chen, I.Z. Kiss, H.-A. Tanaka, J.-S. Li. (2013). Optimal waveform for fast entrainment of weakly forced nonlinear oscillators, *Physical Review Letters* **111**(2): 024102.

J. Qi, A. Zlotnik, J.-S. Li. (2013). Optimal ensemble control of stochastic time-varying linear systems, *Systems & Control Letters*, **62**(11): 1057-1064.

A. Zlotnik, J.-S. Li. (2012). Optimal entrainment of neural oscillator ensembles, *Journal of Neural Engineering*, **9**(4): 046015.

A. Piryatinska, G. Terdik, W. Woyczynski, K. Loparo, M. Scher, A. Zlotnik. (2009). Automated detection of neonate EEG sleep stages, *Computer Methods and Programs in Biomedicine*, **95**(1): 31–46.

August 2014